Order Number 9304720

Computer modeling of blood flow through the heart during the complete cardiac cycle

Printz, Beth Feller, Ph.D.

City University of New York, 1992

U·M·I
300 N. Zeeb Rd.
Ann Arbor, MI 48106

Computer Modeling of Blood Flow through the Heart

During the Complete Cardiac Cycle

by

Beth Feller Printz

A dissertation submitted to the Graduate Faculty in Biomedical Sciences in partial fulfillment of the requirements for the degree of Doctor of Philosophy, The City University of New York.

1992

This manuscript has been read and accepted for the Graduate Faculty in Biomedical Sciences in satisfaction of the dissertation requirement for the degree of Doctor of Philosophy.

Sept. 29, 1992
Date

Harel Weinstein, Sc.D.
Chair of Examining Committee

Sept 30, 1992
Date

Terry A. Krulwich, Ph.D.
Executive Officer

Louis Evan Teichholz, M.D.

Charles S. Peskin, Ph.D.

Edward L. Yellin, Ph.D.

H. Michael Lacker, M.D., Ph.D.

(Supervisory Committee)

THE CITY UNIVERSITY OF NEW YORK

Abstract

Computer Modeling of Blood Flow through the Heart

During the Complete Cardiac Cycle

by

Beth Feller Printz

Advisors: Louis Evan Teichholz, M.D. and Charles S. Peskin, Ph.D.

In this dissertation, a computer model of the left heart originally developed by Peskin and McQueen has been expanded in order to study blood flow through the heart during the complete cardiac cycle.

The original Peskin and McQueen computer model included the left atrium and ventricle separated by a mitral valve, but had no aortic valve. As such, only diastole and early systole could be studied. An ejecting aortic valve has been added to enable modeling of systolic and diastolic function; the model now is also capable of continuously simulating the beating heart. The shape of the heart has been changed to more closely reflect human cardiac geometry by using published data obtained from 2-D echocardiographic studies of the human heart.

The model has also been improved in a number of technical areas. The timestep has been refined to improve temporal resolution. One new display modality has been added: a simulation of color Doppler ultrasound. Volume conservation has been corrected through the introduction of a new formula for the divergence based on an interpolation scheme instead of a simple centered difference.

This expanded computational model of the left heart has been employed to explore a number of different aspects of cardiac physiology and pathophysiology. The effects of mitral apparatus geometry on mitral flow and leaflet motion have been investigated by varying the computational parameters that determine the initial size of the mitral leaflets, chordae tendineae and papillary muscle. This study provides mechanistic explanations for certain clinical observations, including the occurrence of early systolic mitral "regurgitation", the dissociation between mitral valve prolapse, redundant mitral leaflets, and true systolic back-flow, and changes in diastolic filling due to non-atrial causes. Aortic valve physiology also has been studied by changing the parameters that define the model natural aortic valve.

These applications illustrate just a few of the possible uses of this improved two dimensional cardiac model. Many additional clinical situations can be simulated by varying one or more of the model's parameters. Although limitations still remain, this model, which is capable of simulating one or more complete cardiac cycles, can be an important tool for understanding cardiac physiology and pathophysiolgy.

Format of Dissertation

This thesis is prepared according to the new guidelines of the City University of New York which permits the direct incorporation of research articles as chapters. The thesis has a general introduction, several papers as chapters, and a general discussion. Each chapter contains specific introductions, methods, discussions and references. The references for the introduction and discussion follow the discussion.

Acknowledgments and Dedication

There are many people to be thanked for enabling me to complete this project which has spanned four very different departments at three separate institutions.

First, I want to express by gratitude to my co-advisors, Dr. Louis Teichholz and Dr. Charlie Peskin, who in their own very different (and complementary) styles define the word mentor. To Dr. Teichholz - thanks for showing me that it is possible to be an outstanding scientist, teacher, clinician, and magician. To Dr. Peskin - thanks for your unfailing wisdom, warmth and patience, and for helping me feel at home at Courant. It is my hope that I will be half the role model for my students that both of you have been for me. I also want to thank Dr. Ed Yellin for making every trip up to the Bronx an educationally rewarding experience, and Dave McQueen for always knowing exactly where to look for a particular experiment done many years ago and for your immense help whenever computational problems arose.

Next, I want to thank Dr. Terry Krulwich and the Mount Sinai Medical Scientist Training Program for having the courage to let me work out this inter-disciplinary, and inter-institutional, project.

Finally, this thesis is dedicated to my husband David and my parents, without whose love and support I never would have reached this milestone.

TABLE OF CONTENTS

LIST OF TABLES

LIST OF FIGURES

Chapter 1. Introduction

Chapter 2. Aortic Valve Addition

Chapter 1. Introduction

1.1 Background Literature

> [The] effect of this revolution of blood [in the aortic sinuses] is to shut again the open valve of the heart making by its primary reflected motion a perfect closure.
>
> *Leonardo DaVinci, 1513* [1]

Since the time of DaVinci and the Renaissance, the motion of blood through the heart and of the heart valves has been examined and re-examined. Much has been learned about the mechanisms of valve motion and blood flow, but many questions still remain unanswered. Even questions to which we thought we had answers must now be re-examined in light of information ascertained from recently-developed cardiovascular diagnostic procedures. One way to re-analyze the mechanism of valve motion and blood flow is to use a different approach: computer modeling. By using computer models, parameters can be varied independently in a way not possible in human or even animal studies and cause versus effect can be more readily differentiated.

The original computational model developed by Peskin [3] was a two-dimensional model of the left side of the heart. It included a mitral valve but no aortic valve or aorta. One could use this model to study mitral valve motion and intracardiac blood flow during diastole and early systole, up until the time of aortic valve opening. This was adequate for the study of physiological and some pathological mitral valve function as well as for the design of prosthetic mitral valves. Indeed, the basic two-dimensional diastolic model has already offered predictions concerning basic physiological questions which have been validated experimentally [4,5,6].

A complete left heart model can go further in helping one to understand normal physio-

logical as well as pathological function of the heart and valves. The existence of regurgitation through the "normal" mitral valve [7,8], the occurrence of mitral valve prolapse with and without systolic mitral regurgitation [9,10,11], and the controversy surrounding the mechanism of the Austin-Flint murmur of aortic insufficiency [12,13,14] are all areas where a model capable of simulating aortic valve function and the entire heart beat may aid in the understanding of cardiac pathophysiology.

The aim of this project was therefore to develop a cardiac model that includes both diastole and systole, and to use this model to study patterns of blood flow in the heart during the complete cardiac cycle.

1.1.1 General heart and valve function

"The chief function of the heart is the transmission and pumping of blood," stated William Harvey in the beginning of the 17th century [15]. Pumps are devices that impart energy to fluids by accelerating flow. They change the direction and timing of flow using valves and chambers. If pumping is the principal function of the heart and its valves, it seems natural to try to understand this function by developing a model that emphasizes mechanical aspects. In order to develop such a model, however, one must first understand the anatomy and physiology of the heart and its valves. The heart valves are emphasized here, for they are important determinants of the patterns of cardiac blood flow.

The general anatomical features of the cardiovascular system were described as early as the Renaissance by DaVinci (1513) and Vesalius (1543). DaVinci not only described the anatomy of the aortic valve, but also gave one of the earliest descriptions of the mechanism by which the heart valves close (see the beginning quote.) His drawings show vortices in the aortic sinuses aiding in valve closure; he even outlined a method of injecting dye into a glass

model of an aorta to study blood flow (1). However, the idea that blood circulates through the body instead of being continuously absorbed and regenerated was only conceived in 1628 by William Harvey. This began the "modern era of cardiovascular physiology" [16]. The existence of vortices will be discussed in detail, as they are still important in many theories of valve function and cardiac blood flow.

In 1912, Henderson and Johnson constructed a model of heart valves and described two possible methods by which the heart valves could close [17]. The first method is analogous to a door closing during a windstorm: the valve leaflets begin to swing shut as a pressure difference is applied across them. This mode of closure will produce backflow across the closing valve. The second method they termed the "breaking jet" theory. All of a sudden, a fluid jet is stopped: the part of the column of fluid behind the valve stops, while that in front continues moving. This creates a negative pressure region ("like the wake of a ship") which draws fluid in from the sides. The fluid moving in from the sides serves to move the valve leaflets toward closure without significant regurgitation. Henderson and Johnson continue by stating that the semilunar (e.g. aortic) valves always close by this breaking jet mechanism, whereas A-V (e.g. mitral) valve closure may use either mechanism depending on physiological conditions (for example, when atrial/ventricular coordination is absent, no breaking jet appears and regurgitation will occur). The question of whether a normal valve closes with or without regurgitation (i.e. to what extent each of the above two mechanisms contributes to normal valve closure) is still being debated today.

Since Henderson and Johnson's study, most other investigators have concentrated on either the mechanism of mitral valve motion and diastolic blood flow, or that of aortic valve motion and systolic blood flow. This research has included physical in-vitro models of artificial heart chambers with either excised or artificial valves, and invasive animal studies.

Recently, non-invasive human studies and computer modeling work have augmented these types of experiments.

In order to understand any of the experiments concerning blood flow through the heart, one must first understand the different ways by which fluid flow can be examined. There are methods that use injected particles or dye and different types of cameras to "see" the actual flow patterns; Although visualization of these patterns is technically quite difficult, electromagnetic flowmeters [20,21] and hot-film or thin-film anemometers have enabled flow quantification. Various Doppler techniques, included continuous-wave, pulsed-Doppler [22,23,24] and color Doppler [25] ultrasound, together with laser Doppler anemometry [26,27] allow one to study blood velocity; flow quantification by Doppler is as yet only qualitative, however [28,29]. Two-dimensional echocardiography makes visualization of cardiac structures possible [30] Finally, mathematical formulas, such as the Gorlin equation (relating pressure drop across a valve to the area of that valve) [31] or the mitral pressure half time [32], use data from these techniques in order to interpolate other hemodynamic quantities.

1.1.2 Mitral valve function

The motion of the mitral valve and diastolic blood flow in the heart have been reviewed previously by physiologists, engineers and clinicians and only will be summarized here. Indeed, there has been much recent discussion about the importance of diastolic function in determining systolic function. For more detailed explanations, one can consult Little [18], Bellhouse [33], Peskin [19], Schnittger et.al. [34], and Yellin [35].

Theoretical and physical mitral valve models were important antecedents of Peskin's computer model. In 1972, Bellhouse proposed a vortex theory of mitral valve closure and constructed an elastic transparent ventricle in which a model mitral valve was placed [36,37].

Lee and Talbot [38] used a rigid, hinged mitral valve model; they too saw vortices aiding in mitral valve closure. The mitral valve closure theory supported by these models is considered "atriogenic", as ventricular action does not directly lead to valve closure. These models were not truly physiologically accurate, but rather provided qualitative mechanistic explanations of mitral valve function.

Invasive animal research has substantiated many of these theoretical explanations of mitral valve motion. Brockman studied mitral valve motion in dogs, and concluded that mitral valve closure was atriogenic [39]. Taylor and Wade injected radio-opaque dye and fluid bubbles to follow the flow patterns of blood around the mitral valve; they too found stable vortices within the left ventricle and no evidence of regurgitation upon mitral valve closure [40]. Laniado et.al. [41,42] and Tsakiris et.al. [43] used radio-opaque markers to visualize the mitral leaflets of dogs. Vortices aiding in valve closure were again seen, although valve motion could have been impaired by the markers. Other invasive dog studies have augmented the vortex closure idea by concluding that the atrio-ventricular pressure difference closes the mitral valve [44], perhaps with help from the papillary muscles [45,46], mitral annular contraction [47,48] or even leaflet contraction [49,50]. Influences of the atrium and of blood flow itself typically were not considered to be significant. However, these ventriculogenic conclusions were often based on the false assumption that mitral valve closure coincides with the moment of left atrial/left ventricular pressure crossover. Another problem is that dog hearts are not identical to human hearts; thus one cannot extrapolate directly from these studies to determine human mitral valve mechanics.

Peskin's Computer Model

The computational model developed by Peskin, based on many of the above mitral valve studies, has helped to clarify the issue of valve motion. His original model of flow patterns around the mitral valve was introduced in 1972 [2,51]. In this model, a numerical method is used to solve the Navier-Stokes equations describing incompressible fluid flow in order to study the interaction of valve motion and blood flow. Details of this method will be described below. Mathematical models developed by Bellhouse and Bellhouse [36,37] and others usually assume a particular geometry for their flow patterns in order to look at valve motion. In contrast, Peskin's method begins with only the physical characteristics of the fluid, valves and heart wall, then computes what these flow patterns should look like [19]. The original model included only a left atrium (larger than normal, as if all of the pulmonary venous return had already entered the atrium before diastole began) emptying into a ventricle (without any outflow tract or aorta) through a symmetric bi-leaflet mitral valve. Chordae tendineae and papillary muscles were also present, since they are believed to influence the motion of the mitral valve.

Even with such simplifications, useful conclusions could be reached about mitral valve function. Vortices were seen behind a normal valve, in agreement with Bellhouse's model results [37], and an explanation of how these vortices could close the valve without regurgitation (similar to Henderson and Johnson's "breaking jet" theory) was offered. It also was shown that slack chordae led to excessively opened leaflets, no vortices, and poor valve closure. This was contrary to Bellhouse's results, but in agreement with work done by Rushmer [52]. Finally, regurgitation at the level of the mitral ring and not at the cusp margins was noted and explained as being due to the moving leaflets displacing fluid that is "caught" inside the leaflets back towards the left atrium while valve closure occurred. Thus,

experimental measurement of flow at the mitral ring in dogs does not necessarily mean that there is actual backflow of fluid escaping from the ventricle between the cusp margins.

Peskin, together with McQueen [3,5], extended this model to include a more accurate atrium, pulmonary inflow, ventricle, and outflow tract, thus simulating a cross-section of the left heart minus the aortic valve. Geometric parameters were based on data derived from invasive dog studies [4,5].

Output from this extended model, including velocity, atrial and ventricular pressures, mitral diameter and even simulated echocardiograms and phonocardiograms were then compared with experimental data; good agreement was obtained [5]. An exception was that the atrio-ventricular pressure difference in early diastole was lower in the model than in the dog. This could be a problem inherent in the model itself, or due to the experimental flow probe producing an effective stenosis that would raise this pressure difference [21,53]. Recent studies have shown that, indeed, the A-V pressure difference is much smaller than the original experimental studies indicated [54,35]. This model also has allowed one to look at the actual flow patterns versus time, a difficult observation to make experimentally.

The above Peskin–McQueen model was used to study a few pathological condition of the mitral valve. Mitral valve prolapse (MVP) was simulated by making the papillary muscle less stiff. This led to prolapse of the posterior mitral valve leaflet (as in real life), regurgitation in eary systole, and even a "sound" resembling the mid-systolic click of mitral valve prolapse. Clinically, papillary muscle rupture is one mechanism of mitral valve prolapse. Mitral valve prolapse also commonly occurs when mitral valve leaflets and/or chordae tendineae are too large [55], or in the condition known as ischemic mitral insufficiency.

More computational experiments on the diastolic role of the chordae were performed; the results again agreed with experimental dog data [4]. This study refined conclusions

drawn in earlier computational experiments with slack chordae. The diastolic function of chordal tension no longer seemed to be valve closure (as Rushmer stated, [52]), but rather restraint of valve opening, as supported by anatomical data from McAlpine [56], Marzilli et.al. [46] and Yellin et.al. [4]. It also had been noted that excess tension on the leaflets prohibits the valve from closing properly during late diastole and systole [57].

A variety of prosthetic mitral valves have been modeled [19,58]. Fluid flow patterns that were generated enable one to examine how specific changes in the shape of a prosthetic valve could change the valve's performance. For example, since blood stasis is known to lead to thrombus formation, one could look at flow patterns from differently shaped valves to see which would produce the least stasis. Yoganathan et. al. [61,62] used laser Doppler anemometry to aid in the design of a tilting- disc prosthetic valve that would lead to less stasis of blood within the heart. McQueen and Peskin [59] evaluated a model of this type of valve using their computer test chamber: their results agreed with the experimental observation that less stasis could be expected with this valve design. They go on to explain how such studies can be used as a starting point for improved valve design. Once optimal computed prosthetic valve parameters have been determined, the valve can be built and clinically tested. This type of computer method was used by McQueen and Peskin in a design study of curved butterfly bileaflet mitral prostheses [60].

Further improvements have been made to this model. The duration of atrial systole was shortened to be more physiological, and the pulmonary venous return parameters were changed to agree with the experimental data of Rajagopalan et.al. [63,64,65]. Meisner et.al. used this improved Peskin - McQueen model together with invasive dog experiments to study how the timing of atrial systole influences mitral valve closure and flow patterns [6]. The existence of an optimal delay between atrial and ventricular contraction (seen both

in the computer-generated and dog data) was proposed, and an explaination offered; the existence of an optimal PR interval is consistent with Doppler ultrasound results of Halperin et. al. [66]. Meisner et. al. also mention that there was "no significant retrograde flow at any point in diastole for any AV delay", again raising the question of whether "backflow" experimentally measured at the mitral ring is real or just a consequence of fluid being displaced toward the atrium as the valve closes [6].

Alternative Computer Models

A number of different computer models of the mitral valve and ventricle have been described by other investigators. Beyar and Sideman [67] developed a systolic model of left ventricular contraction based on sarcomere physiology. They included sequential activation of the different heart layers (endocardium to epicardium) by representing the ventricle as nested spheroidal shells of muscle fibers. Using this model, they could "measure" pressure-volume data and determine cardiac output (based on volumetric changes). Beyar and Sideman extended their model to include diastole [68], leading to their claim of having developed the "first model to describe complete left ventricular contraction and relaxation." However, their model could only be used to study overall cardiac function, without any information about flow patterns or the mechanics of various sections of the heart.

Meisner [6,69] introduced a lumped parameter analog computer model of the heart to continue his study of the effects of atrial changes on ventricular filling, citing the difficulty of separating out and simultaneously measuring all pertinent hemodynamic variables. He has used this model to explore the atrial contribution to ventricular filling under a number of different conditions, including the presence of mitral stenosis and increased left ventricular compliance [70,35,53], finding good correlation with experimentally-determined data.

However, as he states, this type of model cannot be used to study flow streamlines, regional wall motion or valve movement.

A lumped-parameter model similar to Meisner's has been developed by Thomas and Weyman [71,72,73], which they have used to study the dependence of flow and pressure on chamber compliance and mitral valve morphology. This model uses as input atrial and ventricular pressure at time zero together with chamber compliances and mitral impedence. A system of coupled non-linear ordinary differential equations are solved (using a fourth-order Runge-Kutta technique) in order to calculate transmitral flow, velocity, and pressure versus time. Different mitral valve characteristics are included by varying the mitral impedence parameter, although (as they note) there is no a priori association of this parameter with specific clinical measurements. They too have found good correlation between data generated by their model and both in-vitro simulations and clinical studies. Again, this model cannot be used to study regional wall motion or flow patterns within the heart.

Computer simulations of the mitral valve were developed by Hunter [74], and Miller and Marcotte [75]. Their methods use transvalvular pressure and simple three-dimensional stress/strain considerations to look at leaflet position during systole. Changes in coaptation length and leaflet movement in the atrial direction can be studied (though there is no atrium per se in the model); atrial, pulmonary or fluid influences cannot. Obviously, this also prohibits examination of the flow patterns or ventricular motion itself.

Bryhn and Garding also devised a basic model of mitral valve motion [76]. This model again uses simple geometric force considerations to look at coaptation of normal and enlarged mitral leaflets, specifically with respect to mitral valve prolapse. As before, flow patterns and heart motion cannot be studied.

Kovacs et. al. have introduced a computer cardiac model based on the heart functioning

as a damped simple harmonic oscillator in order to look at the mechanism of diastolic mitral flow [77]. They disregard underdamped conditions based on the velocity profile found clinically by Taylor [78]. Although mitral flow can be studied by this technique, no spatial information concerning the flow is available.

Arts and Reneman have also developed a computer heart model in which the ventricle is modeled as a thick-walled cylinder, the mitral valve simulated by a diode in series with a resistance and inertance, and aortic outflow included as a series of differential flow equations based on pressure, volume, aortic compliance and impedence, and peripheral resistance [79]. They have used this model to look at the mechanical loading of the left ventricle as a function of time. An extra equation is actually added to further damp the mitral flow trace to "agree" with clinical data (although the velocity profile they too used as a standard was also obtained using an implanted flow probe). One observation they made was the occurrence of mitral backflow associated with the movement of the closed mitral valve toward the left atrium during isovolumetric contraction, as has also been noted by Peskin [2] and Meisner [6]. Again, it is not possible with this model to generate actual blood flow patterns inside the heart.

Mechanism of mitral valve closure: Conclusion

Based on all these studies, as well as on non-invasive work using M-mode and Doppler ultrasound visualization of the mitral valve [35,80,81,53], a common view today is that both atriogenic and ventriculogenic mechanisms are important for effective mitral valve closure. Early diastolic filling increases with the presence of a positive atrial - ventricular pressure gradient (the "E wave" on Doppler echocardiograms). A decreasing pressure gradient, together with the chordae and papillary muscle, seem to restrain the mitral valve from

opening excessively. As the atrial - ventricular pressure gradient decreases further (and even reverses) and vortices are formed during mid-diastole, the mitral leaflets move toward closure with a decrease in transmitral flow (the Doppler "E deceleration"). At times, this decrease in mitral flow is followed by an extra mid-diastolic mitral flow peak temporally related to reacceleration of mitral flow following the restoration of a positive transmitral pressure gradient when pulmonary inflow refills the atrium (the "L-wave") [53] Transmitral flow again returns toward zero, only to be increased with atrial contraction (the Doppler "A-wave"). With atrial contraction and further vortex formation behind the mitral leaflets, the valve is positioned toward closure. Ventricular contraction (possibly with help from annular and leaflet contraction) then completely closes the valve with minimal, if any, regurgitation. The chordae/papillary muscles complex decreases the atrial-ward motion of the closed mitral valve throughout systole. An echocardiographic study by Smalcelj [82] seems to contradict the atrial contribution to mitral valve closure, but this difference may be due to the lack of a consistent M-mode echocardiographic definition of when the mitral valve is closed [83,34].

1.1.3 Modeling the Aortic Valve and Aorta

The research outlined above shows how a combination of experimental plus computational methods can aid in the understanding of valve function in particular, and heart function in general. Before incorporating an aortic valve and aorta into the Peskins – McQueen heart model, it was necessary to understand what is already known about the function of the aortic valve and flow patterns in the aorta.

Flow patterns in the aorta are intimately related to the motion of the aortic valve, as can be seen in daVinci's illustration (Fig. 1.2). Many studies have been performed to

determine this relationship. Again, due to the complex mechanical nature of this problem, these studies often utilized physical models of the heart and aorta.

In the mid-18th century, about a hundred years after Harvey's work, Stephen Hales described how the pulsatile arterial flow could be "smoothed" to generate steady venous flow because of the elastic properties of the large arteries; this is the classical Windkessel theory of fluid mechanics that has been used to describe the function of the aorta [84]. Many physical models of the aorta since the time of Hales have focused on this windkessel idea (for example, Beyar and Sideman's model [68]).

Bellhouse and Bellhouse, along with Reid and Talbot [85,86,87,88] developed a physical model of the aortic valve with thin rubber sheets for cusps glued inside a rigid perspex or silicone rubber aortic root that included detachable perspex aortic sinuses. Using dye injection and high speed photography (50 frames/second) to measure velocity, they were able to study the actual flow patterns set up by the aortic valve [88]. Both steady and pulsatile flow were studied. "The essential feature of aortic valve function is the formation and maintenance of trapped vortices", they concluded [88]. The vortices formed in the aortic sinuses early in systole help to fully open the cusps in mid-systole, and then together with the axial pressure gradient, properly close the valve in late systole with only 2% backflow (versus 25% backflow and uneven closing observed without the sinuses present). They also concluded that the velocity profile just above the aortic valve was flat at all phases of the cardiac cycle [88], thus no turbulent jet was present. A theoretical model of aortic valve closure was developed to explain these observations, based on allowing only one degree of freedom in the valve structure (as Peskin [19] explains). As pointed out by vanSteenhoven, however, this model would necessitate excessively large pressure differences across very thin aortic leaflets [89].

Despite the simplifications inherent in their physical and theoretical models, Bellhouse et. al. could even explain the occurrence of angina in patients with aortic stenosis who did not have concurrent coronary artery disease: aortic stenosis (modeled as cusps glued together) produced a turbulent jet and decreased pressure at the coronary ostia located inside the aortic sinus, thereby decreasing systolic coronary flow [85].

Subsequent studies have refined these qualitative ideas. Swanson and Clark [90] calculated the motion of the aortic valve leaflets by mathematically assuming the shape of the velocity profile and then looking at the fluid streamlines across the leaflets. Gillani and Swanson [91] mathematically modeled the aorta as an axisymmetric duct, then used the Navier-Stokes equations to look at the sinus vortices. However, as vanSteenhoven points out [89] they ignored the effects of leaflet impedence on aortic flow.

Hung and Schuessler [92] used Bellhouse and Talbot's data on orifice area and flow rate [88] to develop an axially-symmetric computational model of aortic valve motion. By varying flow rates and cusp speeds, they were able to show that the leaflet's shape and speed could change the orifice area, contrary to assumptions used in the Gorlin equation that orifice area is independent of leaflet shape and speed. The early systolic formation of vortices behind the cusps is in agreement with Bellhouse and Talbot's data, as is the idea that stenosis decreases blood flow in the sinuses.

Peskin and Wolfe [93] developed an alternate mathematical vortex theory to explain how this "trapped vortex" leads to proper valve closure and the upstream (i.e. into the aorta) movement of the vortices observed by Bellhouse and Talbot. Finally, vanSteenhoven and vanDongen [89] developed a two-dimensional mathematical model of the aortic valve. This model also gave good agreement with previous models: a flat velocity profile and a sinus vortex were apparent. They were able to conclude that the valve closes as the cusps move

slowly into the aorta by rotating around their attachment point without changing shape. This study also shows that it is possible to study three-dimensional fluid characteristics using two-dimensional modeling (as noted by Peskin, [19]). But this model ignores viscosity and the effects of pressure on valve geometry. It is also valid only for the flow deceleration phase of valve closure (see vanSteenhoven, [104]).

Various in vitro flow model also have been used to study aortic valve pathology and prosthetic valve design, especially how such pathology affects the accuracy of certain Doppler-derived measurements. Aortic insufficiency has been studied by Taylor et. al., who placed rigid acrylic templates of regurgitant tricuspid, biscuspid, degenerative, and rheumatic aortic valves in a flow chamber and allowed fluid to discharge across these valves [95,96]. They analyzed the regurgitant flow using Doppler color flow mapping and found that aortic valve morphology influences the regurgitant volume measured by Doppler ultrasound (especially for the bicuspid aortic valve). Unfortunately, these studies are limited by the rigid nature of the valve models and the use of steady (not pulsatile) flow. Reimold et. al. developed a method for estimating the effective aortic regurgitant orifice area based on conservation of mass (the continuity equation) using Doppler- derived data, then tested this method using an in vitro aortic model [97]. Another in vitro model used to study aortic insufficiency was developed by Baumgartner et. al., who employed a pulsatile flow model to determine that proximal jet width and area are good parameters for evaluating an aortic regurgitant jet, but that the value of using the jet width is limited by its assumption of a circular defect shape [98].

There have been many recent studies employing in vitro models to study prosthetic aortic valve design, function, and their impact on Doppler measurements. For example, Yoganathan et. al. used an in vitro pulsatile flow model and laser Doppler anemometry

to investigate the influence of valve type on flow, pressure gradient, valvular regurgitation, and fluid stasis [99]. An estimation of turbulent shear stresses downstream of artificial aortic valves was developed by Nygaard et. al., also using a pulsatile model [100]. Finally, Baumgartner et. al. showed how aortic valve design could influence the correlation between Doppler- and invasive catheter-determined pressure gradients by studying the normal aortic valve and a variety of different aortic valves placed in a pulsatile flow model [101].

All of the above physical and computational models make certain assumptions: the fluid used was not blood, effects of viscosity were often neglected, mechanical properties of the aorta were not duplicated and some do not discuss how pulsatile flow would change the results, as Segadal and Matre note [102]. Even with these assumptions good qualitative descriptions were possible, and many of these observations have since been described in invasive dog studies. This includes work by Laniado [41], Thrubriker [103], vanSteenhoven [89,104], Lucas [105] and vanRenterghen [106]. As mentioned briefly regarding the mitral valve, these invasive dog studies share certain problems. Many used positive-pressure ventilation which may change valve motion and cardiac performance [102]. All assume that the presence of flow probes and catheters does not change the velocity profile or valve movement; this assumption probably is not realistic [53]. Also, the delay between various electronic measurement components makes any "simultaneous" measurements questionable (see, for example, vanSteenhoven [94] or Lucas [105]). Finally, aortic geometry in dogs is not identical to aortic geometry in humans. Since geometric considerations are important in determining flow patterns and valve motion one only can use these studies as qualitative explanations of aortic mechanics. These factors illustrate the desirability and usefulness of a complete computational heart model, with an aorta included, in helping to clarify existing questions about cardiac mechanics.

1.2 Mathematical Formulation

The mathematical formulation of this method has been described as it was developed [3,5,2,19,51,58] and only will be summarized here[1]. The immersed boundary technique, as this method is now termed, has been modified to study other fluid dynamics problems such as aquatic animal locomotion [107,108], platelet aggregation [109], fluid flow in the inner ear [110], particle sedimentation [111], and three-dimensional blood flow in the heart [112,113].

In the two-dimensional Peskin - McQueen cardiac model, the heart is treated as if it were immersed in a large, periodic fluid-filled box. All parts of the heart (valves, muscle, chordae, etc.) as well as the blood and external fluid are assumed to have a constant density. This formulation makes it possible to use the Navier-Stokes equations for incompressible flow,

$$\rho(\frac{\delta \mathbf{u}}{\delta t} + (\mathbf{u} \bullet \nabla)\mathbf{u}) = -\nabla p + \mu \nabla^2 \mathbf{u} + \mathbf{F} \tag{1.1}$$

$$\nabla \bullet \mathbf{u} = 0 \tag{1.2}$$

to study the interaction of heart wall and valve motion with fluid flow. Basically, Equation 1.1 is analogous to Newton's force = mass x acceleration, and Equation 1.2 just states that flow is incompressible. The left side of Equation 1.1 is the mass (actually, mass/volume, or density) times fluid acceleration (u=fluid velocity). The right side is the sum of three force densities acting on the fluid: the pressure gradient $-\nabla p$, the diffusion of momentum due to viscosity ($\nabla^2 \mathbf{u}$),and the external forces acting on the fluid, F. The cardiac tissue (including muscle and valves) generates this force F which influences fluid flow through its inherent

[1]This description pertains to the Peskin - McQueen heart model *before* the implementation of the improvements that are the subject of this dissertation. Changes to the formulation described here will be discussed in subsequent chapters.

elastic and muscular properties as well as its motion.

These equations of motion are solved using a finite-difference algorithm developed by Alexander Chorin [114,115,116]. Chorin's method is based on a "projection technique", where the unknown vector **u** is computed by projection of a vector onto two orthogonal vector field spaces: one field which is divergence-free, and the second field where the divergence is non-zero. Mathematically, this can be represented as:

$$\rho\frac{\mathbf{u}-\mathbf{w}}{\Delta t}+\mathbf{D}p = 0 \tag{1.3}$$

$$\mathbf{D}\cdot\mathbf{u} = 0 \tag{1.4}$$

Given a vector **w**, the system of equations above can be solved for the unknowns $(\mathbf{u},p)$ through the following steps. First, evaluate

$$\mathbf{q} = -\frac{\rho}{\Delta t}\mathbf{D}\cdot\mathbf{w} \tag{1.5}$$

Next, solve a discrete Poisson equation for p:

$$-\mathbf{D}\cdot\mathbf{D}p = q \tag{1.6}$$

This Poisson equation is solved using discrete Fourier transform (computationally, using an FFT subroutine).

Finally, evaluate **u**:

$$\mathbf{u} = \mathbf{w} - \frac{\Delta t}{\rho}\mathbf{D}p \tag{1.7}$$

The actual discrete steps used in Chorin's projection method to solve successively for $\mathbf{u}^{n+1,0}$, $\mathbf{u}^{n+1,1}$, $\mathbf{u}^{n+1,2}$ (the intermediate velocities), and $(\mathbf{u}^{n+1},p^{n+1})$ (the new velocity and pressure), are as follows:

$$\rho\frac{\mathbf{u}^{n+1,0}-\mathbf{u}^{n}}{\Delta t} = \mathbf{F}^{n} \tag{1.8}$$

$$\rho\left(\frac{\mathbf{u}^{n+1,1}-\mathbf{u}^{n+1,0}}{\Delta t}+u_x^n D_x^0 \mathbf{u}^{n+1,1}\right) = \mu D_x^+ D_x^- \mathbf{u}^{n+1,1} \quad (1.9)$$

$$\rho\left(\frac{\mathbf{u}^{n+1,2}-\mathbf{u}^{n+1,1}}{\Delta t}+u_y^n D_y^0 \mathbf{u}^{n+1,2}\right) = \mu D_y^+ D_y^- \mathbf{u}^{n+1,2} \quad (1.10)$$

$$\rho\left(\frac{\mathbf{u}^{n+1}-\mathbf{u}^{n+1,2}}{\Delta t}\right)+\mathbf{D}p^{n+1}=0 \quad (1.11)$$

$$\mathbf{D}\cdot\mathbf{u}^{n+1}=0 \quad (1.12)$$

Model Geometry

The model heart is actually a two-dimensional cross-section bisecting the anterior and posterior leaflets of the mitral valve and intersecting the apex, left ventricular outflow tract, and aortic location. This geometry is seen in Figure 1.1A–C; such a representation is similar to the echocardiographic long axis view of the heart. The initial configuration (time=0) corresponds to the onset of diastole: the atrium is relaxed, the ventricle has maximally contracted, and the mitral valve is about to open as atrial pressure just reached ventricular pressure. This heart/valve outline is stored as approximately 300 points in cartesian coordinate form. These points are superimposed on a 64 X 64 fluid mesh, though boundary points do not have to (nor will they typically) correspond to particular mesh points. As the computation proceeds with time, these boundary points move with the fluid, and apply forces (F above) to the fluid. These forces depend on the heart configuration at that particular computational instant.

The geometry of the heart and valves was chosen to correspond to data from invasive dog experiments. Straight lines and circular arcs connect the boundary points. The walls have no thickness so larger strains are necessary to produces a given volume change, as Hunter and Baan explain [117]. All geometric parameters can be varied to model different initial heart or valve configurations, either to agree with experimental data or to test how a single parameter can influence flow patterns and heart performance.

Heart muscle is represented by links that connect the 300 plus boundary points. These links are analogous to springs in that the forces they generate at their endpoints depend on their length. Longitudinal stress of heart fibers can be represented directly as short links connecting adjacent points along the boundary. In the real heart, forces also are generated perpendicular to the model heart's cross section. These cannot be modeled directly in two dimensions, as would be possible in a three-dimensional heart model. Instead, non-physiological cross links are needed to simulate the circumferential stress generated by these perpendicular forces (note Laplace's law, $P \propto T/R$). These cross links are also needed to maintain the correct ventricular shape [5]. Since the cross links are merely artificial devices that generate force only at their endpoints, they do not interfere with the blood flow patterns. Figure 1.1C illustrates some representative cross links.

Hill's three-component model of heart muscle, as described by Braunwald et.al. [118] and shown in Fig. 1.1D, is incorporated into these links. His model includes a series elastic, parallel elastic and contractile element as the components of each muscle fiber. The elastic element is modeled as a linear spring for simplicity, although this could be changed to give increased stiffness when fiber length (here, link length) increases, as noted by Parmley et.al. [119]. The active tension actually is a function of a non-linear series elastic length:

$$Tp = \begin{cases} (L - Lpe) * Spe & \text{if } L > Lpe \\ 0 & \text{otherwise} \end{cases} \tag{1.13}$$

$$Ta = \begin{cases} (L - Lce) * Sse & \text{if } L > Lce \\ 0 & \text{otherwise} \end{cases} \tag{1.14}$$

$$\frac{-dLce}{dt} = \frac{(Vmax/\alpha) * (\alpha * So * L - Ta)}{(So * L + Ta)} \tag{1.15}$$

where:

Ta = active tension

Tp = passive tension

L = instantaneous length

Lpe = initial length of parallel elastic element

Lce = instantaneous length of contractile element

Sse = stiffness constant of series elastic element

Spe = stiffness constants of parallel elastic element

and where Equation 1.15 is equivalent to a family of force-velocity curves with:

Vmax = maximum velocity of contraction

So = slope of the length-tension curve

α = muscle activation as a function of time [5].

Each muscle segment is therefore represented as a pair of links acting in parallel: one generating active tension, the other passive tension. The model muscle does obey Starling's law that as muscle fiber length (here, link length) increases, the force generated also increases (Equations 1.13 and 1.14). However, the restriction $L > Lpe$ or $L > Lce$ for non-zero tension means that a chain of links cannot resist compression and will go slack if the chain becomes shorter than its initial length. A valve that resists compression can be modeled by connecting the links in certain stable configurations, then dropping the restriction that $L > Lce$ (and $L > Lpe$); a chain comprised of equilateral triangles of links (i.e. trusses, like are used to build bridges) is such a stable configuration. Compression-resisting links that

are not restricted to this type of stable configuration can also be constructed by using a more complex form for the forces, as explained by Peskin [19].

Initial tensions are computed based on the common atrial/ventricular pressure at time=0 (the onset of diastole) together with the heart's geometry (using Laplace's law), Equations 1.3 and 1.4 above and experimental data. These are set as described in McQueen et.al. [5].

The mitral valve is composed of two circular arcs tangent to each other at their free margins, pointing toward the apex. The anterior leaflet is larger, as in mammalian hearts, and is connected to the left ventricular outflow tract. The smaller posterior leaflet is connected to the posterior ventricular wall. These leaflets are elastic and flexible, without contractile characteristics. Papillary muscle and chordae, all of which lie outside the plane of the model, are represented as Y-shaped force-generating links connecting the free margins of the mitral valve with the apex, as shown in Figure 1.5 and Figure 1.6. In a three-dimensional heart, chordae and papillary muscles actually would change the flow patterns: fluid would move around these structures. However, blood does not have any room to get around them in a two-dimensional heart. By modeling the chordae and papillary muscle as force-generating links that do not interfere with flow, blood is not obstructed while the proper restraining forces can be represented.

In the present Peskin – McQueen diastolic heart model, papillary muscle activation occurs simultaneously with ventricular muscle activation. However, the magnitude of diastolic papillary muscle activation is set lower than ventricular muscle activation to get good agreement between model and experimental results. The mitral annulus has properties of both atrial and ventricular muscle (again, represented by cross-links); as such, it is consistent with experimental results of Tsakiris et.al. [43,120].

Modeling of pulmonary venous return (Qvr) is based on the simplification that flow

equals the pressure gradient times the resistance:

$$Qvr = (P_{pa} - P_{la}) * R_{pulm} \tag{1.16}$$

where P_{pa} is the mean pulmonary artery pressure, P_{la} is the left atrial pressure and R_{pulm} is the resistance of the lung bed. Other forms for pulmonary venous return such as described by Keren et. al. [53] and Alexander [121], may agree more closely to experimental data but have not yet been included in this computational model.

Once the initial conditions have been set as described, the computational heart beat begins. At first the fluid velocity equals zero. The boundary force density is computed from this starting configuration using a modified Newton's method that is based on reformulating the force as a derivative of an energy function. The force density is spread to the nearby fluid mesh points using a discrete approximation to the two-dimensional delta function. This force field is used in Chorin's method to solve the Navier-Stokes Equations, obtaining new fluid velocity and pressure on the computational grid. Each boundary point is then moved at the new fluid velocity by interpolating the fluid velocity from the grid back onto the boundary points (again using the discrete delta function). This completes one time step; the computation continues with the determination of the new force density at the next time step. A single computer cycle covering diastole through early systole (until the time the aortic valve should open) was comprised of 640 time steps of 0.7 msec duration in diastole and 0.35 msec duration in systole. The time-step refinement is necessary to ensure numerical stability.

A number of additional limitations should also be mentioned here. Due to the model's two-dimensional nature, volumes cannot be calculated directly. Whenever volumes are needed (for instance, in measuring flow or ventricular filling), appropriate areas are multiplied by a reference "thickness", chosen to be equal to one quarter the length of the com-

putational domain (or approximately the diameter of the mitral valve). This factor leads to good agreement between model and experimental volume-dependent results. Since they do not depend on volume, velocity and pressure measurements are free from this problem.

When the model is initially constructed, lengths and times are all divided by a factor of 25 because of computational limitations. Density and viscosity are not affected, but the Reynold's number is also reduced by this factor. This can change the flow patterns by making viscous forces proportionately greater than inertial forces. However, inertial forces still dominate, as McQueen et.al. explain [5].

Results of the computational heart beat have been displayed in a number of ways. There are plots of flow, velocity, atrial and ventricular pressure versus time, simulated M-mode echocardiograms and simulated phonocardiograms. Flow patterns can be displayed as streamlines and pressure contours at each time step, or as a video of computational fluid markers moving with the blood inside the heart. This last method is similar to the clinically-used bubble-injection technique of flow visualization, and similar to contrast angiography.

1.3 Overview of Dissertation

The goal of this project has been to model blood flow through the heart during the complete cardiac cycle. Many modifications have been made to the origin Peskin – McQueen model described above in order to accomplish this goal. Other improvements to the model have also been made during this process. Each chapter in this dissertation is a self-contained presentation of a particular change or series of changes made to the original model. Those changes concerned with adding an ejecting aorta will be presented first in Chapter 2, as this was the project's main focus. Subsequent chapters, therefore, may describe changes that actually were made prior to those described in Chapter 2.

The addition of an ejecting aorta has been accomplished by first changing the geometry of the simulated heart. An aortic valve, together with aortic sinuses and a complete aortic structure, has been modeled. The geometry of the atrium and ventricle also has been changed to more closely simulate human cardiac geometry by using published data obtained from 2-D echocardiographic studies of the human heart to determine the parameters used for the initial heart construction. A generalized form for the sources and sinks used to model pulmonary venous return into the left atrium and ejection into the descending aorta has been developed; this generalization makes it possible to include any number of sources and sinks in the future. The aorta has been tethered in place through the use of links between the aortic boundary points and fixed points in space. This tethering models the physical attachment of the aorta to various connective tissue and vascular structures; it also prevents the heart from rotating and translating as it had done previously. Other technical changes were made in order to include these modifications, including a decrease in the size of the computational timestep, an increase in the size of the computational domain, and an increase in the grid resolution. The simulation also can now be continued over more than

one cardiac cycle. All of these modifications are described in Chapter 2, along with results of two computational heartbeats.

One necessary modification of the original Peskin – McQueen method was to correct the observed volume loss: when ventricular pressure increased, the old method produced a numerical 'leak' where fluid would appear to leave the heart at a rate proportional to the pressure across the walls. Up to one third of the ventricular volume was lost through this numerical leak during systole. Chapter 3 discusses the correction of this volume error through the incorporation of a new form for the divergence used in the last steps of Chorin's method (Equations 1.11 and 1.12 above) in place of a simple centered-difference divergence formula.

Some of the advantages of this computer model can be seen in Chapter 4 and Chapter 5. In Chapter 4, a preliminary form of an ejecting heart model has been used to explore the effects of changing the geometry of the mitral leaflets, chordae tendineae, and papillary muscle on mitral flow and leaflet motion. This study illustrates the ease with which one particular parameter can be varied systematically without changing other parameters, thereby making it more straightforward to differentiate cause versus effect. Finally, Chapter 5 describes the development of a color Doppler ultrasound tool to enable results generated using this model to be displayed in a manner that is familiar to clinicians. This color Doppler tool may also provide mechanistic explanations for certain clinical Doppler observations.

The dissertation concludes with a discussion of where the model stands at present, together with additional planned modifications to even further improve this computational model of blood flow through the heart during the complete cardiac cycle; this discussion can be found in Chapter 6.

Figure 1.1 The Peskin-McQueen Computer Heart Model

(A). View of the base of the heart, comprised of the valve rings, with a line drawn to indicate the two-dimensional cross section that is represented in the model. This plane bisects the anterior leaflet (**AL**) and posterior leaflet (**PL**) of the mitral valve, together with the aortic root, left atrium, and left ventricle.

(B). An illustration of the computational plane as indicated in **(A)**, showing the portions of the atrium, ventricle, and aortic root represented in the model.

(C). The initial configuration of the computational heart model, superimposed on the 64 X 64 computational grid. The initial heart geometry is constructed by the parameters R_{LV}, the left ventricular radium; ZV, the length of the straight segment of the ventricle; ZA, the left of the ventricular outflow tract; ZE, the length of the straight segment of the atrium (which functions to increase the size of the atrium); R_{LA}, the radius of the left atrium; and PHM, the angle of the mitral valve ring with respect to the horizontal axis. The lines across the ventricle represent cross links used simulate the forces generated in the plane perpendicular to the model plane. These links generate force at their end points only, and do not interfere with the flow inside the heart. There is also a source in the middle of the left ventricle which models pulmonary venous return to the heart, a sink equipped with a mathematical pop-off valve which models aortic outflow, and a source/sink around the edges of the domain to accomodate instantaneous changes in volume.

(D). Representation of Hill's three component muscle model, which is incorporated into the links between boundary points used to represent the cardiac muscular characteristics. Each link is comprised of a parallel elastic element (**PE**), a series elastic element (**SE**) and a contractile element (**CE**). The elastic elements are linear springs,

while the contractile element generates force dependent on its velocity of shortening; see [McQueen 82] for details.

(Figure from [McQueen 82], reprinted with permission of author and publisher).

Figure 1.1 The Peskin–McQueen Computer Heart Model

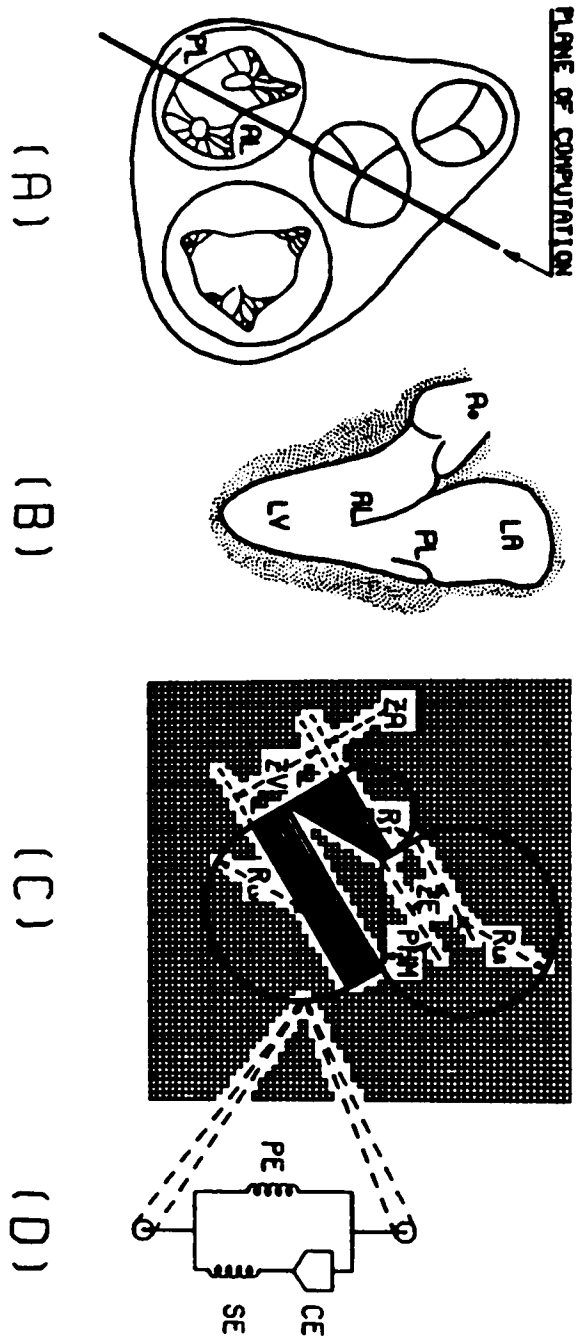

Chapter 2.

Addition of an Aortic Valve to a Two-Dimensional Model of Blood Flow Through the Heart

Beth Feller Printz[1], Louis Evan Teichholz, M.D.[2] and Charles S. Peskin, Ph.D.[3]

[1]Department of Physiology, Mount Sinai School of Medicine

[2]Division of Cardiology, Department of Medicine, Mount Sinai Medical Center

[3]Department of Mathematics, Courant Institute of Mathematical Sciences, New York University

Abstract

The two-dimensional computer heart model pioneered by Peskin and McQueen has been expanded in order to enable the modeling of blood flow through the heart during the complete cardiac cycle. Changes that have been made include the addition of aortic valve leaflets and aorta, modification of the overall heart geometry to better approximate a human heart, addition of an aortic sink located in the descending aorta, tethering of the aorta to fixed points in space, enlargement of the computational grid, and refinement of the timestep. As a result of the addition of an aortic valve, the simulation can now be continued over more than one heart beat.

The expanded computational model has been used to simulate the normal beating heart. Results of these simulations are presented as streamline and fluid marker plots, and graphs of pressure, flow and chamber volume versus time. These results are qualitatively quite similar to those obtained in clinical studies.

This two-dimensional model of the left heart now can be used to study an almost limitless number of physiological and pathological conditions concerning heart valve and chamber function.

Introduction

Peskin pioneered the use of the immersed boundary technique in the development of a two-dimensional computer model of blood flow through the heart [1,2]. He and McQueen have expanded this model during the past twenty years in order to study a number of different aspects of cardiac physiology and pathophysiology, including the function of the normal mitral valve, the influence of the chordae tendineae and papillary muscle in mitral valve motion [2,3], the effect of changing the P-R interval separating atrial from ventricular contraction [4], and the influences of various mitral prosthetic valve design parameters on fluid flow characteristics [3,5,6,7]. The advantage of this model over other cardiac models that have been introduced is its ability not only to generate different flow parameters versus time (such as transmitral flow, pressure, or chamber volumes), but also to provide the actual blood flow patterns *inside* the heart. Indeed, the Peskin – McQueen model has already offered predictions about basic physiological questions that have since been experimentally validated.

Despite its usefulness, the Peskin – McQueen model included only a mitral valve and as such could not be used to study cardiac function after the aortic valve would have opened. This was adequate for the study of physiological and many aspects of pathological mitral valve function, which were their areas of interest. In contrast, a complete left heart model would allow the study of ventricular systole, together with the influence of one upon the other by allowing the computation to continue over more than one heart beat. Such a model would also make it possible to study aortic valve physiology, pathophysiology, and prosthetic aortic valve function. The effects of one valve upon the other could also be examined, for instance looking at the mechanism behind the Austin-Flint murmur of aortic insufficiency [8,9].

This paper describes the steps that have gone into adding an aortic valve to the initial Peskin – McQueen model, along with other changes that have been made to improve that model. A computer simulation of two complete heart beats is presented, together with a discussion of further planned modifications. This expanded model now can be used to study an almost endless number of problems regarding mitral and aortic function, and the influence of atrial and ventricular parameters on blood flow patterns throughout the left heart during the complete cardiac cycle.

Methods

The mathematical formulation of this computational model has been described previously (See [1,2,3,4,5] and Chapter 1.2, *Mathematical Formulation*). Only those portions of the method that have been modified are described here.

Many changes have been made in the process of adding an ejecting aorta to the initial Peskin – McQueen two-dimensional heart model. These changes have included:

1. The structural addition of aortic valve leaflets, two aortic sinuses, an ascending aorta and an aortic arch.

2. Modification of the atrial and ventricular geometry to better approximate the human heart, and the change of certain parameters that influence cardiac function.

3. The addition of an aortic sink in the aortic arch to allow for ejection of blood from the heart.

4. Tethering the aorta to fixed points in space in order to retain the correct shape of the complete aortic structure, as well as to prevent the heart from translating through the periodic computational domain.

5. Enlargement of the computational grid and refinement of the timestep to allow for the above modifications.

Changes in Atrial and Ventricular Dimensions

In addition to incorporating an aorta into this method, geometry of the atrium and ventricle were altered to better simulate human heart dimensions. Chamber dimensions in the original model were chosen arbitrarily to obtain a fairly realistic shape, with the stipulation that the diameter of the mitral ring was accurate (see [3] for further details). The introduction of two-dimensional echocardiography has made measurement of heart chamber dimensions a standard component of clinical cardiac ultrasound evaluations. Triulzi et. al. published a paper in which they listed many of normal cardiac dimensions at end systole (where the computation begins) and end diastole; these measurements were obtained via two-dimensional echocardiography [10]. The end-systolic measurements from this study have been used to redesign the anatomy of the heart represented in the computer model. The chambers still are comprised of straight segments and arc lengths, but now there are additional parameters that can be varied to study different cardiac dimensions. The configuration of the new heart is shown in Figure 2.1; the dimensions initially assigned to the parameters are listed in Table 2.1. Note that the axes of Figure 2.1 are in centimeters, making it possible to read off the dimensions used for any portion of the heart wall. The computational domain is a box 14.7 cm square (versus 7.35 cm previously), with its lower left corner corresponding to the point (0,0) on Figure 2.1. The area of the computational domain has therefore been increased by a factor of four. With this change, the computational grid has been expanded from 64 X 64 to 128 X 128.

This new computational heart is divided into about 750 boundary points (compared to a total of 300 used in the old model), of which 300 make up the aortic structure. These boundary points are still equally spaced an average of one half meshwidths apart from each other.

A few differences between the new cardiac geometry and that of the original Peskin - McQueen model should be emphasized. The left ventricle is more elongated than was modeled previously, and the overall ventricular size greater. It also has a more conical shape, with the ventricle narrowing at the apex. The ventricular inflow and outflow tracts can now be asymmetric, as occurs clinically.

Table 2.2 lists the comparisons between various initial measurements using this new configuration and the clinically-derived measurements from Triulzi et. al. [10] Although the model's parameters are fairly realistic, they are obviously not exact: the model ventricle is slightly wider and shorter than the clinical data suggest, the end-systolic areas slightly less, and the aortic ring and sinus diameters are smaller.

Structural Addition of the Aortic Valve and Aorta

Construction of the aortic valve and aorta also was accomplished using clinically-derived parameters in order to best model the human heart. As this computer method is only two-dimensional, an obvious question is how to model the three aortic leaflets and sinuses. It was decided to use two- dimensional cross-sectional measurements as a first approximation. The aortic leaflets and sinuses modeled here are symmetric, although the method is constructed in such a way that asymmetric geometry can be included. The two cusps included represent both coronary cusps, as these are the two cusps visualized in the echocardiographic apical four-chamber plane that is most similar to the cross-sectional plane of the heart modeled here (with only the left two chambers and aorta included).

Parameters chosen for the construction of the aortic valve and aorta were obtained from a published report by Swanson and Clark [11], who made rubber molds of human aortic valves under different pressures and then calculated dimensionless measurements of the aortic valve and sinus components relative to the aortic inlet diameter. It is these dimensionless numbers that have been used to model the aortic leaflets and sinuses, as listed in Table 2.3. The diameter of the aorta is not an independent parameter in this model, but rather is determined by the construction of the ventricle and outflow tract. These parameters all can be varied to simulate different aortic valve characteristics.

The length of the ascending aorta (3.3 cm) was assigned to achieve a realistic shape within the confines of the computational domain. This is longer than the echocardiographically derived length of 2.4 cm given by Triulzi et. al. [10], but shorter than the echocardiographic measurement of 5 cm given by Friedewald [12]. The radius of the aorta is constant throughout the ascending aorta. The curvature of the aortic arch was arbitrarily assigned, since in reality this is a function of three, not two, dimensions.

The initial configuration of the aortic structure can be seen in Figure 2.2; the parameters corresponding to this figure are listed in Table 2.3. The length of the aortic leaflets is determined by **COAPT** and **PAL** along with angle **PHAS**, the tilt of the center of the valve with respect to the valve ring (used to locate the center of curvature for the aortic leaflet arc). Here, **PHAS** is set to zero and is therefore not shown in Figure 2.2.

One should also note that there have been "aortic chordae" incorporated into this model in order to help keep the aortic leaflets from prolapsing into the left ventricle, and to help keep the aortic valve closed when the aortic pressure is greater than ventricular pressure. These two chordae (one attached to the tip of each aortic leaflet) are modeled in the same manner as the mitral chordae and papillary muscle: they are links that connect the leaflets with a point in the center of the top of the ascending aorta, as shown by the point labeled **PACH** in Figure 2.1. These links do not obstruct the flow, but merely provide forces at their endpoints. There is no physiological equivalent to these structures, which are needed because of the two-dimensional nature of this model. In the real aortic leaflet, force is transmitted to the wall of the aorta by collagen fibers which are perpendicular to the plane of the present two-dimensional model.

Aortic Sink Addition

The initial Peskin - McQueen computer heart model contains a flow source for blood entering the left atrium to simulate pulmonary venous return. The form for this source is given by the equation:

$$Q_s = \frac{(\bar{P}_{pa} - P_{la})}{R_p} \tag{1}$$

where Q_s is the source flow, P_{la} the instantaneous left atrial pressure (computed at each time step), $\bar{P}_{pa}$ corresponds to what would be the mean pulmonary artery pressure, and R_p the pulmonary resistance. This formula, together with a value of 9.33 mm Hg for $\bar{P}_{pa}$, were taken from Rajagopalan et. al. [13,14,15]. R_p was calculated such that the mean cardiac output is 29.6 ml per second [3], with the value for mean left atrial pressure assumed to be 6.6 mm Hg. This formula can be considered a linear resistance model for atrial inflow.

Because the total volume of the computational domain has to remain constant due to the fluid's incompressibility, the increase in heart volume with pulmonary inflow has to be balanced at each time step by an equal volume leaving the computational domain. This has been accomplished by placing a sink at the edge of the domain, and then using the average pressure at this sink as a reference pressure. In fact, the computed pressure outside the heart shows little spatial variation, as would be desired if the fluid outside the heart has little effect on the heart itself (a premise of this form of the immersed boundary technique).

The mathematical formulation of the general Navier Stokes equations included in Chapter 1.3 (Equations 1.1 and 1.2) has been altered to take this source and sink into account, as discussed by Peskin [2]. Instead of using $\nabla \bullet \mathbf{u} = 0$ (Equation 1.2), the equation

$$\nabla \bullet \mathbf{u} = Q(t)\psi_0(\mathbf{x}) \tag{2}$$

is used, where $Q(t)$ is the volume flow rate versus time, and $\psi_0(\mathbf{x})$ corresponds to a weight

function that specifies the spatial distribution of the source and sink:

$$\psi_0(\mathbf{x}) = w_a(\mathbf{x} - \mathbf{X}) - w_e \tag{3}$$

where w_a is a weight function for the atrial source located at $\mathbf{X}$, w_e is a weight function for the external sink around the edge of the domain, and

$$\int w_i(\mathbf{x})d\mathbf{x} = 1. \tag{4}$$

Because the domain is periodic,

$$\int \nabla \bullet \mathbf{u}d\mathbf{x} = 0 \tag{5}$$

and the total flow into the heart over the entire computational domain has to be balanced by the flow out of the domain. This is the mathematical reason why a sink is needed with a source.

The addition of a source and sink modifies the last two steps of Chorin's projection method used to solve the Navier Stokes equations (see Chapter 1.2). Instead of

$$\rho\frac{\mathbf{u}^{n+1} - \mathbf{u}^{***}}{\Delta t} + \mathbf{G}P^{n+1} = 0 \tag{6}$$

$$D\mathbf{u}^{n+1} = 0 \tag{7}$$

(where $\mathbf{u}^{***}$ is the intermediate velocity found through the earlier fractional steps of Chorin's method), Equations (6) and (7) take the form

$$\rho\frac{\mathbf{u}^{n+1} - \mathbf{u}^{***}}{\Delta t} + \mathbf{G}P^{n+1} = 0 \tag{8}$$

$$D\mathbf{u}^{n+1} = Q(t)\psi_0(\mathbf{x}) \tag{9}$$

From these two equations, one can derive the Poisson equation:

$$kDGP^{n+1} = D\mathbf{u}^{***} - Q(t)\psi_0(\mathbf{x}) \tag{10}$$

These equations are solved as described by Peskin in [2] to find the pressure field, and then the fluid velocity, at the new timestep (P^{n+1} and $\mathbf{u}^{n+1}$, respectively).

In order to model aortic outflow, the above source/sink procedure has been generalized in such a way that number of sources and sinks now can be included. The terms 'source' and 'sink' actually are interchangeable, as the direction of flow (into or out of the heart) becomes determined by the direction of the pressure difference; here the term 'source' will be used to refer to both. What follows are the changes that have been made to the mathematical procedure as described by Peskin [2] to include more than one source.

The goal is as follows. Given P_i^s (the average pressure at source i, like $\bar{P}_{pa}$ in equation 1 above), R_i (the resistance of the *ith* source, like R_{pa}), and N (the number of total sources, *excluding* the external reference source, here labeled $i = 0$) we wish to find Q_i, the flow through source i, (equivalent to Qs in equation 1), and $P_i' = P_i - P_0$, the instantaneous pressure at the *ith* source location relative to the reference pressure P_0 (like P_{la}).

A formula equivalent to Equation 1 therefore can be written:

$$Q_i = \frac{P_i^s - P_i'}{R_i} \tag{11}$$

or by rearranging terms,

$$P_i' = P_i^s - Q_i R_i \tag{12}$$

and Equation 2 above now becomes

$$\nabla \bullet \mathbf{u} = \sum_{i=0}^{N} Q_i w_i(\mathbf{x}) \tag{13}$$

Next, define the pressure at source i, P_i, and the pressure at the reference source P_0 (the reference pressure):

$$P_i = \int w_i(\mathbf{x}) P(\mathbf{x}) dx \tag{14}$$

$$P_0 = \int w_0(\mathbf{x})P(\mathbf{x})dx \tag{15}$$

Equation (5) above states that the total flow from all sources into the heart has to equal the flow from the reference source out, or

$$Q_0 = -\sum_{i=1}^{N} Q_i \tag{16}$$

and therefore, in place of Equation 2 (and Equation 13), we can now write

$$\nabla \bullet \mathbf{u} = \sum_{i=1}^{N} Q_i(w_i(\mathbf{x}) - w_0(\mathbf{x})). \tag{17}$$

If we now define

$$w_i' = w_i(\mathbf{x}) - w_0(\mathbf{x}) \tag{18}$$

then the instantaneous pressure at the *ith* source relative to the reference pressure, P_i', can be defined as

$$P_i' \equiv P_i - P_0 = \int_0^1 P(\mathbf{x})w_i'(\mathbf{x})d\mathbf{x} \tag{19}$$

and the latest form for Equation 2 can be expressed as

$$\nabla \bullet \mathbf{u} = \sum_{i=1}^{N} Q_i w_i'(\mathbf{x}) \tag{20}$$

It is at this point that the last two steps of Chorin's method, Equations 6 and 7 above, are used. The first two steps are to solve for P_i^*, the pressure at source i when all sources and sinks are off:

$$k\mathbf{D}\mathbf{G}P^* = D\mathbf{u}^{***} \tag{21}$$

then, find P_i^* according to

$$P_i^* = \int w_i'(\mathbf{x})P^*(\mathbf{x})d\mathbf{x} \tag{22}$$

Note that this last equation is represented as a summation in its computational implementation. Computationally, this is accomplished by a single call to the Poisson solver routine, which itself calls a fast Fourier transform (FFT) subroutine. We then solve the equation

$$k\mathrm{DG}P_i = w_i'(\mathbf{x})Q_i \tag{23}$$

(when $i = 1 \cdots N$) for all P_i, the pressure at source i with $Q_i = 1$ (i.e. for a *unit source*) and all other sources turned off. For each equation, the pressures at all the other sources (P_j) are also 'measured' using the type of formula seen in Equation 21. Equation 23 is solved by one call to the Poisson/FFT subroutines for each source; therefore, if there are N sources, these subroutines are called a total of N+1 times: one time for Equation 21, and N steps for Equation 23.

The final step is to construct an N X N matrix **A**, where A_{ij} are the values of the pressures measured at source j when the strength of source i, Q_i equals 1 (using Equation 23), together with an N X N diagonal matrix **R**, where R_{ii} is the resistance of source i and all other terms in **R** are equal to zero.

Expressing the total pressure as a linear combination of the pressure with all sources off and the pressures with unit strength times the source strength,

$$P_i' = \sum_{j=1}^{N} A_{ij}Q_j + P_i^* \tag{24}$$

Substituting the right hand side of Equation 24 into Equation 12,

$$P_i^s - P_i^* = Q_iR_i + \sum_{j=1}^{N} A_{ij}Q_j \tag{25}$$

This formula is now expressed in matrix notation:

$$(\mathbf{R} + \mathbf{A})\mathbf{Q} = \mathbf{P}^s - \mathbf{P}^* \tag{26}$$

and the source strengths Q_i are found by matrix factorization. These values for Q_i are then substituted back in to Equation 11 to find P_i'. All the values for P_i are added to the pressure field P^*, and it is this pressure field P^{n+1} (actually, the *gradient* of this field) that is used to compute the fluid velocity via the last step in Chorin's method:

$$\mathbf{u}^{n+1} = \mathbf{u}^{***} - \frac{\Delta t G P^{n+1}}{\rho} \tag{27}$$

It should be noted that the form for the divergence, D used above has been changed from the simple centered difference form used in Peskin's earlier work to a finite difference form based on the interpolation scheme used to communicate quantities between fluid grid points and boundary points. The reason for this change was to improve volume conservation, as will be discussed in Chapter 3.

In its present form, the number of sources is equal to two: an atrial inflow source that models the pulmonary venous return to the heart, and an aortic outflow source (i.e. a sink) located in the arch of the aorta (see Figure 2.1). The values of the parameters that determine the atrial inflow have not been changed from those listed above. The values for the aortic sink parameters have been assigned using an formula similar to Equation 1:

$$Q_{ao} = \frac{\bar{P}_{ao} - P_{ao}}{R_{ao}} \tag{28}$$

where $\bar{P}_{ao}$, the mean aortic reservoir pressure, arbitrarily has been set to 40 mm Hg, and P_{ao}, the aortic pressure, set to 39 mm HG in order to assign a value to R_{ao}. It is the value of R_{ao} that is of clinical significance. The reason for this arbitrariness is that with the original Peskin – McQueen model, the ventricle could not develop realistic peak ventricular pressures during systole. If the aortic pressure were assigned a value greater than the peak ventricular systolic pressure that was actually obtained, the heart would never eject. These parameters will be changes once it is determined what peak ventricular pressures can be

achieved with this expanded model.

The generalized source/sink procedure also makes it possible to include coronary sinks, more than one atrial source, and the flow of blood through branch vessels in the aorta. The only necessity is that the computational grid be large enough to accomodate these sources/sinks: at present the sources and sinks are squares with 8 gridpoints per side, although 4 X 4 sources and sinks also have been tested successfully.

Tethering of the aorta to fixed points in space

The aorta, including the aortic sinuses, has been tethered to fixed points in space by using links similar in design to those that represent the forces generated by the heart wall. These links have been used to retain the correct aortic shape without including the short links and cross links that represent the heart wall. The other reason for linking the aorta is that when sources and sinks are included, the floating heart both rotates and translates within its periodic computational domain in order to conserve linear and angular momentum. Neither the rotation nor translation are serious problems because the domain is periodic, as long as one similarly displaces the external sink used to defined the reference pressure (see above) so this sink does not overlap the heart. It is, however, more difficult to interpret the results as one always has to correct for this rotation and translation. Additionally, it seems physiologically accurate to fix the aorta since in reality there are connective tissue structures that hold the aorta in place.

The locations of these fixed points are assigned such that they overlay the initial aortic configuration. These links develop restoring forces that tend to bring the actual aortic configuration back to its initial configuration. The stiffness of these links was assigned arbitrarily to allow the aorta to contain reasonable pressures (compared to peak ventricular pressure) and still retain its shape; the value that has been used is STFFIX = 40. STFFIX is employed to calculate the force in the fixed links through the simple linear spring equation $\mathbf{F} = k(\mathbf{X} - \mathbf{X_0})$, where k is the spring stiffness (here STFFIX) and $\mathbf{X} - \mathbf{X_0}$ is the change in the length of the spring from its resting length $\mathbf{X_0}$ (which is here equal to zero). Because so much of the force ends up being concentrated at the aortic valve ring (where there is a sudden change from the tethered to the untethered portions of the heart wall), the stiffness of the links connected to the aortic ring and to the aortic sinus points has to be increased.

Without this increase, the untethered part of the heart separates from the aorta along the left side of the aortic ring during ventricular systole. This stiffness increase is achieved by a graduated method: the fixed links connected to the two aortic ring points have a stiffness equal to three times the stiffness of the points in the ascending aorta. The link stiffnesses in the aortic sinuses decrease by equal amounts from the aortic ring; the points joining the aortic sinuses with the ascending aorta have the same stiffness as those throughout the aorta. The effect of tethering the aortic sinuses is that one cannot study the physiological change in their dimensions during the cardiac cycle. The method is constructed in such a way, however, that the fixed links can begin anywhere (or even not be included), making such studies feasible.

Other Changes

There have been other changes made to the Peskin – McQueen model during this expansion. With the increase in the size of the computational grid to 128 X 128, the timestep also has been decreased. There were 960 timesteps for every heartbeat in the previous experiments performed using the Peskin – McQueen model. Given a heart rate of 75 beats per minute (what has been used), this corresponded to one timestep for about every 0.7 msec. This timestep is now four times smaller, or about 0.18 msec per timestep for a total of 3840 timesteps per heartbeat. As before, the timestep is refined further (by a factor of two) during ventricular systole to retain numerical stability.

The stiffness of the atrium and ventricle has been increased from the values previously used by decreasing the strain parameters that determine the ratio of the change in the length of the links that comprise the atrial and ventricular muscle from their initial lengths, $STRAIN = (R - REST)/REST$, where R is the instantaneous length of the link, and $REST$ is the resting length of the link when it is under no tension. The atrial strain parameter, STRA, has been decreased from 2 to 1.5, and the left ventricular parameter, STRV, has been decreased from 0.3 to 0.175. The reason for these changes were that initial experiments performed using the expanded model showed the ventricle to be expanding too much.

This model now also allows unequal stiffnesses in the short and cross links comprising the ventricle, making it possible for the heart to contract by different amounts along its long and short axes in order to simulate more physiological ventricular shape changes. In the present model, the strain parameter for the short ventricular links is now half as large as the strain parameter for the ventricular cross links. Thus, the short links are stiffer than the crosslinks; the strain parameter for these short links is therefore 0.0875, using the value

of STRV listed above. The stiffness of the links that define the mitral and aortic valves also contain factors, STFMV and STFAV, respectively, which are actual *stiffness* (versus strain) parameters that can multiply the leaflet stiffnesses used in the original model. Therefore, an increase in these parameters has the effect of *increasing* the stiffness of the mitral and aortic leaflets. The values used in the experiments included below were STFMV = 1 and 1.5, and STFAV = 2.0 and 3.0, as will be described below.

Results

Experiment I.

The expanded computer model has been run over two complete heart beats, with all parameters assigned as explained above. The aortic resistance, R_{ao}, was computed using an aortic pressure of 39 mm Hg and a ventricular pressure of 40 mm Hg; therefore, the resistance of this source/ sink is lower than the resistance of the atrial source). The atrium contracts at 350 msec, while the ventricle contracts at 450 msec for an atrial - ventricular delay (equivalent to an electrocardiographic PR interval of 100 msec). Ventricular systole begins at 450 msec (and at 1125 msec for the second heart beat: 675 msec duration of one beat, plus the 450 msec). Data generated from this experiment are shown in Figures 2.3 through 2.21. Figure 2.3 through Figure 2.8 illustrate different measurements with respect to time, while Figures 2.9 through 2.20 show the heart configuration and streamlines at equally spaced times throughout the two cardiac cycles. Figure 2.21 plots the heart configuration and fluid markers that are carried through the heart with the fluid itself, also at a number of different timesteps.

In order to interpret the data presented, a few comments are necessary. First, all flow quantities have been computed using an artificial length scaling factor, as described in [3]. This is necessary because of the two-dimensional nature of the method. Instead of using the value of one-quarter the length of the computational grid as was used previously, the length scaling factor has been set equal to the diameter of the mitral annulus (2.5 cm). The effect of this arbitrary scaling factor is that all flows only can be considered qualitative rather than quantitative. Pressures, velocities, lengths and tensions are not affected by this scaling.

Measurements concerning the valves have been made at two different locations: the

annulus (ring) and the cusp, which is defined as the location between the tips of the valve leaflets. The terms annulus and ring have been used interchangeably. Clinically-derived flow measurements usually are made at the level of the valve rings using electromagnetic ring flow probes. There also has been much progress made recently toward the use of Doppler ultrasound to measure the fluid velocity across both these levels. Flow through the valve ring can be thought of as consisting of two components: true flow from one chamber into another, and flow measured because the leaflets displace a certain volume of fluid when they move. These two components can be differentiated by looking at the difference between flow through the valve ring and flow through the valve cusp. If the valve were stationary, ring flow would equal cusp flow. If the valve were opening, there would be forward flow through the mitral ring that was not seen at the cusp; a closing valve would have greater negative flow through the ring than the cusp. Therefore, the difference between ring and cusp flow is a measure of the volume swept out by the leaflet's movement. This idea is explained further in [4] and in Chapter 4.

Atrial and aortic pressures are the average pressures at the atrial source and aortic sink relative to a reference pressure measured at the edge of the computational domain (as described in the above section regarding the source and sink procedure). The relative ventricular pressure is measured at a pressure 'tap' in the mid ventricle using the same procedure as for the atrial and aortic source/sinks, but with no actual flow allowed.

Figure 2.3 illustrates plots of mitral and aortic flow versus time over two heart beats, each of which lasts 675 msec. These flow events can be correlated with the atrial and ventricular pressures as shown in Figure 2.4. Looking at Figure 2.3, upper left panel, (mitral annular flow), one can see that early diastolic flow increases rapidly as atrial pressure exceeds ventricular pressure, peaking at about 50 msec. This is followed by a rapid decline

in flow as the atrial - ventricular pressure difference (the driving pressure for transmitral flow) decreases. There is then a small flow 'hump' before mitral flow returns to zero during mid-diastole (and even goes slightly below zero, as if flow was going in the reverse direction, from the ventricle to the atrium). The lack of mid-diastolic flow is associated with a *negative* pressure gradient, as ventricular pressure actually exceed atrial pressure. With atrial contraction at about 300 msec, the transmitral flow sharply increases as a positive transmitral pressure gradient is established again. The mitral valve closes as diastole ends and ventricular contraction begins. This valve closure is associated with a large negative flow transient and subsequent low-flow oscillations during systole. When the first heartbeat ends at 675 msec and the second heartbeat begins, there is again a rapid flow increase. The magnitude of the flow peak is lower, however, and the flow returns to zero by about 850 msec. This is followed by a second, mid-diastolic flow peak associated with a second reversal of the transmitral pressure gradient from negative to positive (even though this pressure difference is quite small). Transmitral flow again returns to zero prior to increasing with atrial contraction. The peak transmitral flow that occurs with this second atrial contraction is very similar to the one associated with atrial contraction of the first heartbeat, despite the lower amount of flow during the earlier part of diastole.

The flow through the mitral cusp is similar to the flow through the annulus, but there are a few important differences that should be noted when one compares the upper panels of Figure 2.3. There is no longer any mid-diastolic flow reversal: there is no flow between 260 and 350 msec. Second, the negative flow transient associated with mitral valve closure that is seen through the mitral ring (left panel) is not seen through the mitral cusp (right panel). There is, however, a small, short duration, *positive* flow spike at this time. Third, the early and mid-diastolic flow through the mitral cusp is much lower during the second heart beat

than the first. Finally, the flow does not return to zero before the second, mid-diastolic, flow peak during either the first or the second heart beat.

Flow through the aortic ring and cusp can be analyzed similarly. In the lower panels of Figure 2.3, negative flow is flow out of the aorta. Looking at Figure 2.3, lower left panel, and Figure 2.4, there is an initial oscillatory flow and pressure transient which decreases in amplitude over the first 100 msec. This flow transient is not seen across the cusps (Figure 2.3, lower right). The trans-aortic ring and cusp flow then is zero until isovolumic ventricular contraction increases the ventricular pressure until it is greater than aortic pressure, and the valve opens. The valve remains open, with flow through both the aortic ring and cusp, during systole. With the end of ventricular contraction, the ventricular pressure falls below aortic pressure and flow through the aortic valve decreases. Flow through both the aortic ring and cusps becomes positive, representing regurgitant flow from the aorta into the left ventricle across both the ring and cusp. The magnitude of this regurgitant flow across the cusps is less than the flow across the aortic ring, suggesting that most of the annular backflow is due to the aortic leaflets dispacing fluid as they move toward the ventricle as pressure falls. Again, there is an oscillatory component of this flow at the valve ring not seen at the cusp (as in Figure 2.3, top panels). Before the next beat begins at 675 msec, the trans-aortic cusp flow returns to zero: the aortic valve has now closed. The only difference between the aortic flow patterns for the two heart beats is that the initial flow transient seen at the aortic ring during the first beat does not occur during the second heartbeat.

Looking at the pressure versus time data in Figure 2.4, one should notice the small magnitude of the diastolic atrial - ventricular pressure gradient (the bottom two curves), as well as the crossovers between atrial and ventricular pressures. The ventricle reaches a peak systolic pressure of about 80 mm Hg, compared to a peak aortic pressure of about 60. This

peak ventricular pressure can be compared with the peak ventricular pressure of about 40 mm Hg obtained with the initial Peskin – McQueen model. Aortic pressure remains constant at about 40 mm Hg during diastole (recall that, according to Equation 26, aortic flow will be zero at this pressure, since 40 mm Hg was the value used for mean ventricular pressure). The aortic pressure decreases for a short time at end systole, temporally related to the small amount of regurgitant flow that was seen in Figure 2.3, lower panels.

Figure 2.5 illustrates the transmitral and transaortic velocities, again at both the annular and leaflet tip levels. These results are qualitatively very similar to the flow data seen in Figure 2.3. One difference should be noted: the velocity of the spurt of regurgitation through the aortic cusp is equal to the velocity through the aortic ring, whereas the flow volume through the ring was greater. Also, observe that the velocity through the cusp (Figure 2.5, upper right) is greater than the velocity through the annulus (Figure 2.5, upper left); the reverse pattern was seen in Figure 2.3.

The amount of flows entering and leaving the heart through the atrial source and aortic sink are shown in the upper left panel of Figure 2.6. One can see that the rate of atrial inflow (upper curve) initially increases, then remains about constant through early and mid-diastole. Pulmonary venous return then decreases during atrial contraction, as atrial pressure decreases relative to the assigned mean pulmonary arterial pressure of 9.33 (see Equation 1), and oscillates somewhat during ventricular systole. Atrial inflow increases again as systole concludes and the second cardiac cycle begins. A different representation of the same information is seen in the upper left panel of Figure 2.6, where the flows into or out of the source/sinks have been integrated (actually summed): the slope of the integrated atrial flow curve (upper curve) remains essentially constant through diastole and decreases slightly during systole. This process repeats during the second heartbeat.

The aortic sink flow can be seen in the lower curves of Figure 2.6, upper panels. At first, flow is negative: the aortic sink acts as a source to 'charge' the aorta by filling it with fluid. This is followed by damped oscillations through the first 150 msec, after which the flow remains zero until systole. During systole the aortic sink functions as expected, enabling fluid to leave the heart. There is again a short duration spurt of blood *entering* the aorta through this source/sink associated with the aortic regurgitant flow seen in Figure 2.3; the total volume of this spurt of aortic inflow is represented by the peaks at about 600 and 1250 msec in Figure 2.6, right upper panel.

There are a number of different points that should be mentioned concerning the changes in cardiac chamber volumes over time which are illustrated in the lower left of Figure 2.6. Atrial volume (bottom curve) decreases during early systole as blood leaves the atrium at a faster rate than it enters through the pulmonary venous source, reaching a relative minimum at about 200 msec. During the mid-diastolic decrease in transmitral flow, atrial size increases. Atrial contraction brings the atrial volume down to about 10 cc, only a third of what it began. Volume again increases as the mitral valve closes and flow continues into the atrium through the pulmonary venous source. The atrial volume at the end of the first heartbeat is about 20 cc, about one third lower than its initial volume. The decreased atrial volume (and decreased change in volume) during diastole of the second heartbeat is associated with a decrease in transmitral flow, as seen in Figure 2.3, upper panels. Atrial chamber volume remains at about 20 cc at the end of the second heartbeat.

Ventricular volume, on the other hand, *increases* over the the period of one cardiac cycle, as seen in curve (c) of Figure 2.6, from its original volume of 40 cc, to its volume of 50-55 cc at the end of the computational heart beats. Note that the total volume of blood ejected per heartbeat (equal to the change in ventricular volume) is 25 cc, for an

ejection fraction of about 50%. Remember, however, that all volumes have been obtained by using a "characteristic thickness" since the two-dimensional model heart has no actual thickness. The more important number is therefore the ejection fraction, rather than the stroke volume.

Overall, the decrease in atrial volume is about the same as the increase in ventricular volume, and the total volume (atrial plus ventricular plus aortic) is changed by less than 10 cc, as can be seen in the top curve. This was important for being able to continue the computation over the second heartbeat. Aortic volume (seen in the curve second from top) varies little through the two cycle, as would be expected as a consequence of tethering the aorta to fixed points in space (if these links can generate sufficient force).

Although it is not illustrated here, the heart is no longer "leaky" as it was in earlier versions. This is despite the increase in peak ventricular pressure by a factor of two using the expanded model as compared with the original model. Indeed, the volume error of a single heart beat is now less than 1%: the difference between net integrated inflow and the change in total chamber volume is approximately 1cc over one cardiac cycle. This improvement is due to the incorporation of a new form for the divergence, as will be discussed in Chapter 3.

Figure 2.7 shows the diameters of the mitral and aortic rings and cusps. In the upper left panel of Figure 2.7, one can see that the mitral annular diameter (top curve) decreases during atrial contraction, and then increases during ventricular systole as the atrium relaxes. The distance between the leaflet tips (the level where the blood actually passes from the atrium to the ventricle) is less than the mitral annulus diameter throughout the cardiac cycle. As in the mitral flow curves (Figure 2.3, top), the mitral cusp diameter curve contains an extra peak during mid-diastole of the second heart beat. It is also interesting that the

leaflet tips do not join completely as they reach their minimum separation during diastole, although flow through the annulus is zero. This is consistent with the small volume of mid-diastolic flow across the leaflet tips (Figure 2.3, top right), even in the face of a negative pressure gradient (Figure 2.4). Competent mitral valve closure can be seen by the mitral cusp diameter of 0.2 cm during systole (this is essentially zero in the computational method, as there is a "numerical glue" that causes points very close together to stick to one another).

Because the aortic ring is tethered to fixed points in space, it is not surprising that the aortic ring diameter (upper curve, top right of Figure 2.7) changes little throughout the cardiac cycle. It does expand slightly during ventricular systole, however. Competent aortic valve closure is seen throughout diastole, with the aortic valve opening for about 150 msec during ventricular contraction (lower curve).

Tensions in the links that represent the mitral chordae and papillary muscle can be seen in Figure 2.8, left panel. Note that these structures are under only very slight tension during early and mid-diastole. These tensions increase a small amount during atrial contraction, and then increase substantially as the mitral valve closes with ventricular contraction. The highest tensions are found in the papillary muscle link, as this link actively contracts during systole. Tensions all return to zero as the second beat begins. (The very narrow spike at the beginning of the second heart beat is an artifact produced when certain parameters are reset as the timestep is changes back to its original, non-refined, value.)

The tensions in the two artificial aortic chordae are seen in Figure 2.8B. After the initial damped oscillations of the tensions (due to the charging of the aorta as it is filled with blood), these chordae remain under a small amount of tension during diastole as they assist in keeping the aortic valve closed. During systole, the tensions fall to zero as the aortic leaflet tips separate and flow crosses the aortic valve. Competent aortic valve closure at the

end of systole occurs with a small amount of tension in the links. Note that the magnitude of these tensions throughout is smaller than those in the mitral valve chordae shown in the left panel of Figure 2.8.

Flow Patterns and Heart Configuration

The change in the heart's configuration and fluid streamlines are shown in Figures 2.9 through 2.20. Each of these figures is comprised of the flow patterns at four different timesteps, equally spaced 28 msec (160 timesteps) apart. The atrial source and aortic sink can be visualized as areas *without* streamlines, as these are areas where stream functions cannot be computed since the velocity divergence is not zero. The source and sink are connected to the external sink at the edge of the computational domain by cuts which also can be seen in certain frames. The location of the virtual points to which the mitral and aortic chordae are attached are indicated by the 'O's seen in the mid-ventricle and aorta, respectively. One can follow the change position of the point that attached the two chordae tendineae with the papillary muscle during the cardiac cycle. The position of the aortic virtual point does not change substantially, since it is linked to points along the ascending aorta that are also linked to fixed points in space. It is important to remember that the presence of streamlines crossing the heart walls and valve leaflets does not imply that there is actual fluid crossing these surface, but that these boundaries are moving.

As one proceeds from Figures 2.9 through 2.14 (the first cardiac cycle), one can watch the heart "beat". First, the mitral leaflets separate during early diastole as flow velocity across the mitral ring increases: the increased velocity can be inferred from the increased density of streamlines across the valve. The ventricle gradually elongates and vortices form behind the mitral leaflets (see Figure 2.9, bottom right, and 2.10). It should be noted that the transmitral flow aligns perpendicular to the mitral ring, with the central transmitral

streamlines pointing toward the left wall of the ventricle, *not* the apex, as seen in Figure 2.10, upper right and lower left panels. The vortices and the decreased transmitral pressure gradient serve to bring the mitral leaflets towards closure during mid-diastole (Figures 2.10 (lower left) through 2.12 (upper right)), and transmitral velocity decreases (less dense streamlines). Atrial contraction is seen in the four frames of Figure 2.12. This contraction is accompanied by an increase in transmitral flow as the leaflet tips again separate. These mitral leaflets have returned toward closure in Figure 2.12, lower right, again due to the vortices shed from the leaflet tips with additional assistance from the onset of ventricular contraction. Figure 2.13 illustrates ventricular systole. Competent mitral valve closure preceeding aortic valve opening can be seen in Figure 2.13A, followed by the opening of the aortic valve in Figure 2.13B. Aortic outflow peaks during mid-systole (Figure 2.13C), and then declines as contraction ends (Figures 2.13D through 2.14B). The aortic valve closes and stays closed for the remainder of the first cardiac cycle; this is accompanied by ventricular relaxation and lower blood velocities throughout the heart, as seen by the sparsity of streamline (Figures 2.14B through 2.14D). Note that the streamlines follow the aortic arch around and end at the aortic sink, as would be expected. Also note, however, that no vortices can be seen in the aortic sinuses. The mitral valve, as desired, remains closed throughout systole.

The flow patterns and heart configuration of the second heart beat are very similar to those for the first heart beat. However, the atrium begins from a smaller volume, and the ventricle begins from a larger volume. Mitral valve opening is delayed, and the transmitral flow has decreased (compare Figure 2.15 with Figure 2.9). This decreased flow is seen throughout mid-diastole in Figures 2.16, lower left, through Figure 2.18, upper left. Atrial contraction substantially increases transmitral flow velocity (note the increased streamline

density in Figure 2.18, remaining panels). The rest of the second cardiac cycle continues like the first cardiac cycle, as shown in Figures 2.19 and 2.20.

An alternative way to look at the fluid flow patterns within the heart is illustrated in Figures 2.21A through 2.21G. Fluid markers have been placed in the atrium and ventricle prior to the first heart beat. These particles move with the blood, as would be seen if one injected dye or bubbles intravenously and then observed their transit through the heart. Only a few representative frames from the first heart beat have been included here. In Figure 2.21A, which corresponds to a point during early systole, one sees how these fluid markers are initially aligned before any significant flow begins. Vortices can be seen forming behind the mitral leaflets in Figure 2.21B, which corresponds to the movement of the mitral leaflets toward closure during mid-diastole. Figure 2.21C illustrates the beginning of ventricular systole, when the fluid particles have first emerged into the ascending aorta. Finally, Figures 2.21D through 2.21G show the fluid markers collecting in the aorta (and especially near the aortic sink) with subsequent aortic valve closure. Note that washing of those particles located along the posterior ventricular wall is not complete.

Experiment II

In order to exhibit how this method can be used to study the change in any particular parameter, the results described above can be compared to another simulation that was performed. In this second simulation, the aortic valve pressure used to set the aortic valve resistance was decreased from 39 to 38 mm Hg. This has the effect of doubling the aortic resistance, as can be seen from Equation 28. There were also two other differences between these two experiments. The stiffness of the mitral leaflet links (STFMV above) was 50% less, as was the stiffness of the aortic leaflet links. The effects of these changes on the flow patterns can be seen in Figures 2.22 through 2.24. The solid curves correspond to this second simulation, while the dashed curves are the same as seen in Figures 2.4 through 2.6 above (although only the first heart beat is included). One can see that peak aortic pressure *increases* with this decrease in the pressure parameter P_{ao} (Figure 2.22), which may at first seem counterintuitive. However, remember that pressure is proportional to resistance in this linear model of aortic flow. This increased peak aortic pressure is associated with a decrease the pressure gradient between the left ventricle and aorta (it is in a sense behaving as a *less* stenotic aortic valve), a decrease in trans-aortic velocity (Figure 2.23C and 2.23D) and a decrease in flow out through the aortic sink, as shown in Figure 2.24. Thus, the heart has a net gain of 10 cc in volume over one heartbeat, versus 6 cc seen in Experiment I (compare with Figure 2.6). The transmitral velocities are essentially unchanged (Figure 2.23, upper panels), as are the mitral and aortic leaflet annular and cusp diameters (not shown), providing evidence that the aortic pressure changes were not the result of the change in the valve stiffness parameters. Therefore, this experiment also illustrated that the mitral and aortic flows were not very sensitive to changes in leaflet stiffness at the magnitudes used.

Discussion

This paper has described the changes that have been made to the Peskin – McQueen computer model of blood flow through the heart in the process of simulating the complete cardiac cycle. As the results presented above demonstrate, this expanded model is now capable on not only simulating a single heart beat, but of continuing over more than one heart beat.

As the intent of this cardiac model is to analyze normal and pathological cardiac physiology, the model should produce data that are comparable to those observed clinically. What follows is a discussion of how the results described above compare to both clinically-derived data and to the data generated with the original Peskin – McQueen model.

Diastolic Mitral Valve Motion and Transmitral Flow Characteristics

The diastolic mitral flow produced in this expanded model is qualitatively quite similar to data obtained experimentally and clinically; it is also similar in most respects with the computed flow patterns obtained previously. Comparing the mitral annular flow and pressure traces shown in Figure 2.3 (top left) and 4 with those generated using the old model (Figure 2.25), one can see that transmitral annular flow now goes to zero prior to atrial contraction, versus previously remaining elevated during mid-diastole. With the expanded model, there is an extra mid-diastolic flow peak, clearly seen in the second heartbeat. Flow again returns to zero before being accelerated by atrial contraction during late diastole. Looking at the pressure tracings, one should note that the atrial-ventricular pressure gradient is decreased throughout diastole in the new method, and the ventricular pressure actually exceeds atrial pressure at times during diastole (which temporally correlates with the changes in the transmitral annular flow).

The diastolic flow pattern generated by the original Peskin – McQueen model is consistent with a pattern of mild mitral stenosis, as discussed by Keren et. al. [16], Yellin et. al. [17], and Meisner et. al. [18]. In previous work done using the model, it was thought that this pattern *was* the normal flow pattern because it matched experimentally (in dogs) data obtained via implanted electromagnetic flow probes. Keren et. al., however, describe how the implantation of the flow probe may produce some degree of functional stenosis [16], resulting in a slower decline in diastolic mitral flow together with a larger pressure gradient between the atrium and ventricle. Recent use of pulsed Doppler ultrasound to non-invasively measure transmitral flow (actually) has shown that the normal transmitral annular flow *does* decrease rapidly during early to mid-diastole, often falling to zero in the presence of slow heart beats. Such a result can be seen in Figure 2.26, which was obtained via pulsed-Doppler echocardiography and high fidelity atrial and ventricular pressure recording. The data represent diastole in a normal conscious dog; they were obtained in the laboratory of E.L. Yellin. Comparing Figures 2.5A (mitral annular velocity) and 26, one should note the similarity in the flow traces. This similarity extends to the occurrence of the mid-diastolic flow peak during the second heartbeat. This is what has clinically been called the "L-wave". The presence of multiple diastolic pressure crossovers in both the computer-generated data and clinical data also should be noted. It is these crossovers that are responsible for the new 'normal' transmitral flow pattern shown above, as Keren [17] and Courtois [19] discuss.

Note that there are two main differences between the transmitral annular velocity computed using the expanded model and the clinical data shown in Figure 2.26. First, the computed velocities are lower than those measured clinically. This may be a result of the increased effective viscosity inherent in the computational method because of the length

and time scaling employed. It may have to do with the two-dimensional nature of this model mitral valve: flow is forced to converge more through a three-dimensional valve than through a two-dimensional valve, and greater flow convergence produces higher velocities. Second, the relative sizes of the three diastolic transmitral flow peaks are different. Because the atrium begins at a lower volume (and the ventricle at a higher volume, and is therefore stiffer) during the second heart beat, the driving pressure across the valve is lower and early diastolic ventricular filling is decreased. This decrease in early diastolic transmitral flow velocity with increased ventricular stiffness was seen by Thomas et. al. in an experiment using a lumped parameter model to study changes in ventricular filling [20]. This pattern is also consistent with the echocardiographic data obtained in the case of 'diastolic dysfunction', when a stiffer ventricle impairs early diastolic filling [17]. As in that clinical situation, the computed transmitral flow associated with atrial contraction (the third diastolic flow peak) remains constant, however.

The appearance of the mid-diastolic flow peak (L-wave) with the expanded model compared to its absence in the original model can be due to a number of factors. One factor that influences the absence or presence of this flow peak is the heart rate: faster heart rates do not allow enough time to transpire before atrial contraction. Since the heart rate has not been changed between the two forms of the model, it is not responsible for this different flow pattern. Another factor that seems to play a role in the presence of this L-wave is the stiffness of the ventricle. Experiments using Meisner's lumped-parameter model found that *decreasing* the ventricular stiffness led to the disappearance of this mid-diastolic flow peak [17],i.e., that the *stiffer* ventricle had more 'normal' diastolic transmitral flow. The ventricle was made stiffer in the experiments shown above, as compared with those performed with the original model. Thus, the increased ventricular stiffness could be the mechanism for

the appearance of the mid-diastolic flow peak. Another possibility is that the change in the ventricular anatomy produced a relative decrease in the mitral valve impedence, leading to more rapid decline in the early diastolic flow and a smaller transvalvular pressure gradient (together with pressure crossovers).

Mitral Valve Closure

Mitral valve closure is accompanied by a spurt of backflow seen through the mitral valve annulus which is not seen through the cusp. The mechanism for this flow is the displacement of fluid engulfed between the closed mitral leaflets moves toward the atrium at the end of diastole. Thus, the backflow is not true regurgitation. This closure transient has been seen using the original Peskin – McQueen model, and has been discussed previously (see [3,4]); its significance also will be discussed in Chapter 4). Following valve closure, one can see oscillations in the mitral annular flow trace due to vibration of the closed mitral valve with the force of ventricular contraction. Laniado and Yellin have attributed the first heart sound to these oscillations [17,21], as has Peskin previously [2]. Oscillations are similarly seen in the atrial pressure curve (Figure 2.4) and in the pulmonary venous return (upper left panel of Figure 2.6). The mitral valve then remains competently closed throughout systole. The end-systolic small shoulder of forward flow usually observed in the mitral annular flow trace is even discernable through the oscillations. One also can see from Figure 2.14 that the closed mitral valve has begun to move down toward the ventricle.

These differences between mitral annular flow patterns and mitral cusp flow patterns should be emphasized. Clinical studies often do not indicate at which of these locations any measurements have been made. As was seen in the top right panel of Figure 2.5, velocity through the mitral cusp was greater than velocity through the mitral ring, especially once atrial contraction begins. Since certain clinical measurements are based on the relative size

of these flow peaks (for example, the 'E to A ratio'), it is important to determine where a clinical measurement has actually been made before interpreting the significance of that measurement. This influence of sample volume location of flow measurement also has been described clinically by Dittrich et. al., who also found that the early and late peak velocities measured by Doppler ultrasound were significantly lower at the mitral annulus than at the cusp [22].

Aortic Flow

During the initial 100 msec of the first heart beat, the aortic flows and aortic pressure all exhibit damped oscillations associated with the 'charging' of the aorta and establishment of tension in the fixed aortic links. These oscillations are absent in the second heart beat, illustrating the advantage of continuing the computer simulation over more than one beat. Indeed, the method has been constructed in such a way that one can store the pressure, flow and boundary position at the end of a 'normal' beat, and then change any parameter to see its effect on subsequent cardiac function without the results being confounded by initial transients. Another way to overcome the initial transients might be to change the resting length of the fixed aortic links from zero to a value that takes into account the desired aortic pressure by using Laplace's law.

Competent aortic valve closure is maintained throughout diastole, but with the use of artificial 'chordae' to prevent the leaflets from prolapsing across the aortic ring due to the pressure gradient across the leaflets; the tension in these links is relatively low, however. Flow through the aortic valve is also qualitatively similar to clinical data: the curve has a steep downslope, peaks, and then decreases more slowly. The flow velocity, however, again is lower than seen clinically.

Vortices cannot be seen in the aortic sinuses, however, in contrast to studies by Bellhouse and Bellhouse, and vanSteenhoven [23,24,25]. Despite this lack of vortices, the aortic valve does close competently before the cardiac cycle begins anew. This closure is slightly delayed versus what is seen clinically, and accompanied by a spurt of regurgitation. A small amount of aortic regurgitation is often seen clinically, even with normal aortic valves. Since only two aortic leaflets have been included here because of the model's two-dimensional limitations, a bicuspid aortic valve actually has been modeled. It might be interesting to surmise that the increased aortic regurgitation seen with bicuspid aortic valves may be similar to the necessity of "aortic chordae" to retain competent closure of the aortic valve.

It is possible that vortices are present, but are too small to see. More likely, however, is that the lack of vortices is a consequence of the small size of the aortic sinuses relative to the computational grid, resulting in poor computational resolution within the sinuses. Also, a large portion of the sinus would contain the boundary layer, especially given the artificially low Reynold's number that increases the thickness of this layer. Another reason for this lack of vortices could be that the aortic leaflets are so long compared to the height of the aortic sinus that there is no room in two dimensions for blood to enter the aortic sinuses when the valve is opened (see Figure 2.13). In three dimensions, there has been evidence for that blood enters the center of the aortic sinus but leaves through the commissure. Obviously, this cannot occur in a two-dimensional model.

There are a few methodologic modifications that are planned to see if aortic vortices can be produced with the model. First would be to simply increase the grid resolution. Second, the aortic leaflets could be shortened such that they could still coapt, but would allow for increased flow between their tips and the aortic walls. Finally, there are different computational techniques that can be tried. The simplest would be substituting a Navier-

Stokes solver that could allow for increased Reynold's numbers (described below). A more complex technique would be to try a grid-free fluid solving algorithm such as one recently developed by Buttke [29], in order to concentrate more computational resources where they are most needed (here, in the aortic sinuses.). How these aortic vortices can aid in valve closure has been described by McCracken and Peskin [30].

Another complication of the relatively small size of the aortic sinuses compared to the computational grid is that modeling the coronary artery outflow is not possible at present, although it is hoped that with one of the above techniques this will become possible.

Pressure Comparison

Diastolic atrial and ventricular pressures generated with the expanded model agree well with the pressures seen clinically, as discussed above. However, the peak systolic ventricular pressure of 80 mm Hg is still somewhat lower than it should be (although it is twice as high as had been obtained with the original model). There are a number of possible explanations for this difference, many of which will be tested in the future. First, the aortic diastolic pressure is not physiologic at present. The ventricle therefore does not have to generate as much pressure before the aortic valve opens; following aortic valve opening, ventricular pressure must fall. If aortic pressure were higher, ventricular pressure would have to increase more before ejection begins. Second, the ventricular activation may be too low: a more forceful ventricular contraction may increase peak ventricular pressure. It is likely that by increasing both ventricular activation and aortic pressure, peak ventricular pressure will be increased. Third, the peak ventricular pressure could be increased by increasing ventricular stiffness (or decreasing compliance). Finally, the value used for the aortic resistance has been assigned arbitrarily and may be set incorrectly, as there seems to be a lot of "stenosis" across the

valve: there is a large difference between peak ventricular pressure and peak aortic sink pressure. A decrease in this pressure gradient was seen in Experiment 2, where the aortic sink resistance had been raised by a factor of two. These two seemingly inconsistent ideas can be explained as follows. An increase in aortic sink pressure makes it more difficult for blood to leave through the sink once it has already entered the aorta. This increases aortic pressure, and in essense shifts the stenotic point from across the aortic valve to the aortic sink itself. Peak ventricular pressure was not increased, however, in the second experiment. Besides studying the effect of other changes in this aortic sink resistance, a better solution would be to change the form for the aortic sink to a more physiologically accurate one (such as a Windkessel, or RLC circuit).

Chamber Volumes

Although the heart is initially constructed to closely match actual (two-dimensional) cardiac geometry, this is not the same geometry to which it returns at the end of the cardiac cycle (compare Figure 2.1 or the upper left panel of Figure 2.9 to Figure 2.14, lower right or Figure 2.20, lower right): the atrium has become about 30% smaller, and the ventricle about 30% larger. How these volume changes affect the flow patterns has been discussed above. The fact that the volumes at the end of the second heartbeat are about the same as the volumes at the end of the second illustrates that the heart has approximately "settled down" to this new geometry. There are two ways to alter the model's steady-state geometry. First, one can adjust the parameters used to construct the heart before the first timestep *such that* the heart reached the desired steady-state geometry. It may only be necessary to continue the simulation over a single heart beat to solve for this desired geometry, thereby decreasing the computational expense of this somewhat implicit technique.

Another method of altering the model's steady-state geometry would be to change other parameters that influence cardiac geometry, such as initial pressures and flow rates. For example, modifying the form for the pulmonary venous return from the simple linear resistance model used here to one that is more physiologically correct might augment atrial filling during systole, and thereby increase end-systolic atrial volume. There has been much progress recently in the study of pulmonary venous flow patterns, including work by Alexander who measured flow using an ultrasonic probe [26] and Keren who used Doppler ultrasound [27]. One improvement would be to included capacitance and inertance to Equation (1); alternately, the pulmonary pressure itself could be made time dependent. Instead of a single venous source, inflow could be modeled as the four separate pulmonary veins that are present by using the generalized source/sink solver described above. Finally, since this model now is capable of continuing over more than one heart beat, the atrial source could be connected to the amount of blood leaving the aorta through a lumped-parameter circulation model that includes the right heart [28]. This would indeed be the most physiological solution.

Another way to correct the volume difference may be to change the relative stiffnesses between the atrium and ventricle. Here, the atrium has also been made stiffer compared to the original model. This could decrease the atrial filling. By systematically changing the atrial stiffness parameter in this model, one can study how atrial size (and transmitral flow) are affected.

Computational Considerations

Simulations are at present being conducted on a Cray-YMP supercomputer, where each cardiac cycle takes about 50 minutes of CPU time. For comparison, the earlier method took about 5 minutes to run on the same computer. Many of the changes described above

are responsible for this increased computational demand, including the increased number of timesteps per beat and the increased grid resolution. Also, much more data is being generated: writing to files is computationally expensive. One therefore might ask, why not use a three-dimensional model if the two-dimensional model needs so much computer time? The answer is that three-dimensional models are even more time consuming. A compromise would be to simulate in two dimensions a large number of different clinical situations, then study those situations that give particularly interesting or important results using the three-dimensional model now being developed by Peskin and McQueen [32,33]. Other planned improvements are to optimize the entire two-dimensional computer code for performance on vector machines, and to rewrite the program to take advantage of the parallel-processing computers that recently have been developed.

The increase in the size of the heart and of the computational domain has had the advantage of increasing the Reynold's number by a factor of four, from about 80 to 320. As discussed in [2,3], the Reynold's number was artificially decreased by a factor of 25 when all lengths and times were scaled down by this factor to make the program computationally tractable, given available computing resources as well as the first-order accuracy of Chorin's projection method. This scaling has the effect of increasing viscous forces versus inertial forces; it does not affect the pressure or velocity measurements. Evidence has previously been given that the inertial forces still dominate, as can be seen by the mitral vortex formation and the occurrence of increasing transmitral flow in the presence of a decreasing pressure gradient during early and middiastole [3]. Of course, it would be better if such scaling was not employed. Progress toward this goal should soon be made with the incorporation of a second-order accurate Navier Stokes solver (also based on the projection method) recently been introduced by Bell, Collela and Glaz [31] into this method in place

of Chorin's original projection method. The modular nature of this model makes such a substitution straightforward. The incorporation of this new fluid solver will make it possible not only to increase the Reynold's number to physiological levels, but to also study in a contained manner the actual effect of a change in Reynold's number, such as occurs with exercise.

One might expect that it would not have been necessary to increase the timestep by the same factor of four that the grid was increased. However, the forces (hence pressures) that are now generated are much greater than before. It these forces that determine the convergence of the energy minimization routine, which has been the limiting step in the temporal resolution.

Limitations and Conclusions

This paper has described the steps that have gone into expanding the two-dimension Peskin – McQueen computer heart model to enable the modeling of blood flow through the heart during the complete cardiac cycle. These steps have included the addition of an aortic valve, two aortic sinuses, and a complete aortic structure. Changes have been made to the initial cardiac geometry to more accurately model human heart dimensions. However, the geometry of the heart at the end of one or two heart beats is not identical to this desired geometry. Some possible solutions to this problem will soon be attempted. The aorta is now fixed in space via links between the boundary points and fixed points in space; this simulates the relative immobility of the aorta due to its surrounding vascular structures and connective tissue. The method of modeling sources and sinks has been expanded to enable one to include any number of sources and sinks. In this way, it may be possible to directly model the four pulmonary venous sources into the left atrium, or even possibly model the

coronary arteries if the relative size of the aortic sinuses compared to the computational grid resolution can be increased. Finally, certain technical changes have been made to allow the above physical changes.

Results have been presented showing that this expanded two-dimensional model produces data that are qualitatively quite similar to data measured clinically, including the correct shape of the diastolic transmitral flow and atrial - ventricular pressure gradients. The aortic valve remains competently closed throughout diastole, albeit with the assistance of artificial "aortic chordae", and opens well during ventricular systole. Despite a lack of vortices seen in the aortic sinuses, the valve closes competently at end systole with only a small spurt of regurgitation. The ability of the expanded model to continue over more than one heartbeat has also been shown; this enables more steady-state physiology, as would be desired.

Although this expanded computer model has corrected some of the limitations of the original Peskin - McQueen model, limitations obviously still remain. Many of these have already been described, but should be emphasized: those due to the two-dimensional nature of this model, the still sub-physiologic Reynold's number, the simplified forms for the pulmonary venous return and aortic outflow, and the low peak pressures in the ventricle and aorta.

Despite these limitations, this expanded computer model of blood flow during the complete cardiac cycle produces data that is remarkably similar to that seen clinically. This model can now be used to systematically study a virtually limitless number of situations related to cardiac physiology and pathophysiology, including aortic valve pathophysiology, the influence of one diseased valve on another (for example, the Austin-Flint murmur of aortic regurgitation), and the interaction of diastolic and systolic cardiac function.

References

[1] Peskin CS. Flow patterns around heart valves: a numerical method. J Comput Phys 10:252-271, 1972.

[2] Peskin CS. Numerical analysis of blood flow in the heart. J Comput Phys 25:220-252, 1977.

[3] McQueen DM, Peskin CS, Yellin EL. Fluid dynamics of the mitral valve: physiological aspects of a mathematical model. Am J Physiol 242 (Heart Circ Physiol 11):H1095-1110, 1982.

[4] Meisner JS, McQueen DM, Ishida Y, Vetter HO, et. al. Effects of timing of atrial systole on LV filling and mitral valve closure: computer and dog studies. Am J Physiol 249 (Heart Circ Physiol 18):H604-619, 1985.

[5] Peskin CS, McQueen DM. Modeling prosthetic heart valves for numerical analysis of blood flow in the heart. J Comput Phys 37:113-132, 1977.

[6] McQueen DM, Peskin CS. Computer-assisted design of pivoting disc prosthetic mital valves. J Thorac Cardiovasc Surg 86:126-135, 1983.

[7] McQueen DM, Peskin CS. Computer-assisted design of butterfly bileaflet valves for the mitral position. Scand J Thor Cardiovasc Surg 19:139-148, 1985.

[8] Laniado S, Yellin EL et. al. Physiological mechanisms in aortic insufficiency: I. The effect of changing heart rate on flow dynamics. II. Determinants of Austin-Flint murmur. Circulation 66:226-35, 1982.

[9] Fortuin NJ, Craige E. On the mechanism of the Austin Flint murmur. Circulation 45:558-570, 1972.

[10] Triulzi M, Billam LD, et. al. Normal adult cross-sectional echocardiographic values: linear dimensions and chamber areas. Echocardiography: A Rev of Cardiovasc Ultras 1:403-426, 1984.

[11] Swanson WM, Clark EC. Dimensions and geometric relationships of the human aortic valve as a function of pressure. Circ Res 35:871-882, 1974.

[12] Friedewald VE. Textbook of Echocardiolgraphy. WB Saunders, Philadelphia, 1977.

[13] Rajagopalan B, Friend JA, Stallard T, DeJ Lee G. Blood flow in pulmonary veins: I. studies in dog and man Cardiov Res 13:667-676, 1979.

[14] Rajagopalan B, Friend JA, Stallard T, DeJ Lee G. Blood flow in pulmonary veins: II. the influence of events transmitted from the right and left sides of the heart. Cardiov Re 13:677-683, 1979.

[15] Rajagopalan B, Bertram CD, Stallard T, DeJ Lee G. Blood flow in pulmonary veins: III. simultaneous measurements of their dimensions, intravascular pressure, and flow. Cardiov Res 13:684-692, 1979.

[16] Keren G, Meisner JS, Sherez J, Yellin EL, Laniado S. Interrelationship of mid-diastolic mitral valve motion, pulmonary venous flow, and transmitral flow. Circ 74:36-44, 1986.

[17] Yellin EL, Nikolic S, Frater RWM. Left ventricular filling dynamics and diastolic function. Progr Cardiov Dis 32:247-271, 1990.

[18] Meisner JS, Keren G, Pajaro OE, et. al. Atrial contribution to ventricular filling in mitral stenosis. Circ 84:1469-1480, 1991.

[19] Courtois M, Kovacs SJ, Jr, Ludbrook PA. Transmitral pressure - flow velocity relation. Importance of regional pressure gradients in the left ventricle during diastole. Circ 78:661-671, 1988.

[20] Thomas JD, Choong CYP, Flachkampf FA, Weyman AE. Analysis of early transmitral Doppler velocity curve: effect of primary physiologic changes and compensatory preload adjustment.

[21] Laniado S, Yellin EL, Miller H, et. al. Temporal relation of the first heart sound to closure of the mitral valve. Circ 47:1006-1014, 1973.

[22] Dittrich HC, Blanchard DG, Wheeler KA, McCann HA, Donaghey LB. Influence of Doppler sample volume location on the assessment of changes in mitral inflow velocity profiles. J Am Soc Echo 3:303-309, 1990.

[23] Bellhouse BJ, Bellhouse FH. Mechansim of closure of the aortic valve. Nature 217:86-87, 1968.

[24] Bellhouse BJ, Bellhouse FH, Reid KG. Fluid mechanics of the aortic root with application to coronary flow. Nature 219:1059-61, 1968.

[25] vanSteenhoven AA, vanDongen MEH. Model studies of the closing behavior of the aortic valve. J Fluid Mech 90:21-32, 1979.

[26] Alexander J, Nikolic S, et. al. The role of the pulmonary venous impedence and the atrium in determining caharacteristics of left ventricular filling. Presented at the Cardiac Sytems Dynamics Society meeting, Halifax, Nova Scotia, 1988.

[27] Keren G, Pardes A, Miller HI, Scherez J, Laniado S. Pulmonary venous flow determined by Doppler echocardiography in mitral stenosis. Am J Cardiol 65:246-249, 1990.

[28] Peskin CS, Tu C. Hemodynamics in congenital heart disease. Comput Biol Med 16:331-359, 1986.

[29] Buttke TF. A Lagrangian numerical method for incompressible flow in three dimensions which preserves kinetic energy. Submitted to J Comput Phys, 1992.

[30] McCracken MF, Peskin CS. A vortex method for blood flow through heart valves. J Comput Phys 35:183-205, 1980.

[31] Bell JB, Collela P, Glaz HM. A second-order projection method for the incompressible Navier Stokes equations. J Comput Phys 85:257-83, 1989.

[32] Peskin CS, McQueen DM. A three-dimensional computational method for blood flow in the heart: I. Immersed elastic fibers in a viscous incompressible fluid. J Comput Phys 81:372-405, 1989.

[33] McQueen DM, Peskin CS. A three-dimensional computational method for blood flow in the heart: II. Contractile fibers. J Comput Phys 82:289-97, 1989.

Table 1

Parameters Used for Heart Geometry Initialization	
Parameter	**Initial Value**
AVNT	$\pi/16$
D1	4.1 cm
ZVW	3.3 cm
AMV	$\pi/12$
ZOL=ZOR	0.36 cm
ALVERT	$\pi/16$
ZE	0.88 cm
PHA	$\pi/16$

Table 2

Comparison between Initial and Clinically-Derived Measurements		
Parameter	Model Value	Clinical Value
DAORTA	1.7 cm	1.9 cm
DSM	2.4 cm	2.8 cm
Superior-Inferior Atrial Length	3.7 cm	4.8 cm
Atrial Width	3.5 cm	3.0 cm
Ventricular Length	5.0 cm	6.1 cm
Maximum Ventricular Width	4.1 cm	3.3 cm
Mitral Annulus Diameter	2.5 cm	2.5 cm
Atrial Area (2-D)	12 sq cm	13.7 sq cm
Ventricular Area (2-D)	16 sq cm	17.6 sq cm

Table 3

Dimensions Used for Aortic Structures versus Clinical Data		
Parameter	Model Value	Clinical Value
H	1.2 cm	0.7*(DAORTA)
DSM	2.4 cm	1.4*(DAORTA)
COAPT	0.29 cm	0.17*(DAORTA)
PAL	$\pi/6$	$\pi/6$
ZASC	3.3 cm	2.4 - 5 cm (see text)
ARCHANL	π	no 2-D clinical data
FARCH	0.1	no 2-D clinical data

Figure 2.1 Initial Heart Geometry

AVNT is the angle between the vertical axis and the straight segment of the ventricular wall and **D1** is the widest distance across the ventricle; (these two determine **RV**, the radius used to construct the arc that forms the ventricular apex).

ZVW is the length of the straight segment of the ventricular wall; **AMV** is the angle between the horizontal axis and the mitral valve ring; **ZOL** and **ZOR** are the lengths of the left and right portions of ventricular outflow tract, respectively (here are equal). **ALVERT** is the angle between the vertical axis and the left portion of the ventricular outflow tract (here equal to **AVNT**, such that the left portion of the ventricular outflow tract is a parallel continuation of the straight segment of the ventricular wall). **ZE** is the length of the straight portion of the atrium to allow for the aortic sinuses, as well as to increase the size of the atrium. **PHA** is the angle between the horizontal axis and the radius of the aorta that passes through the center of curvature. Changing this angle increases or decreases the size of the atrium.

Figure 2.1 Initial Geometry of Improved Cardiac Shape

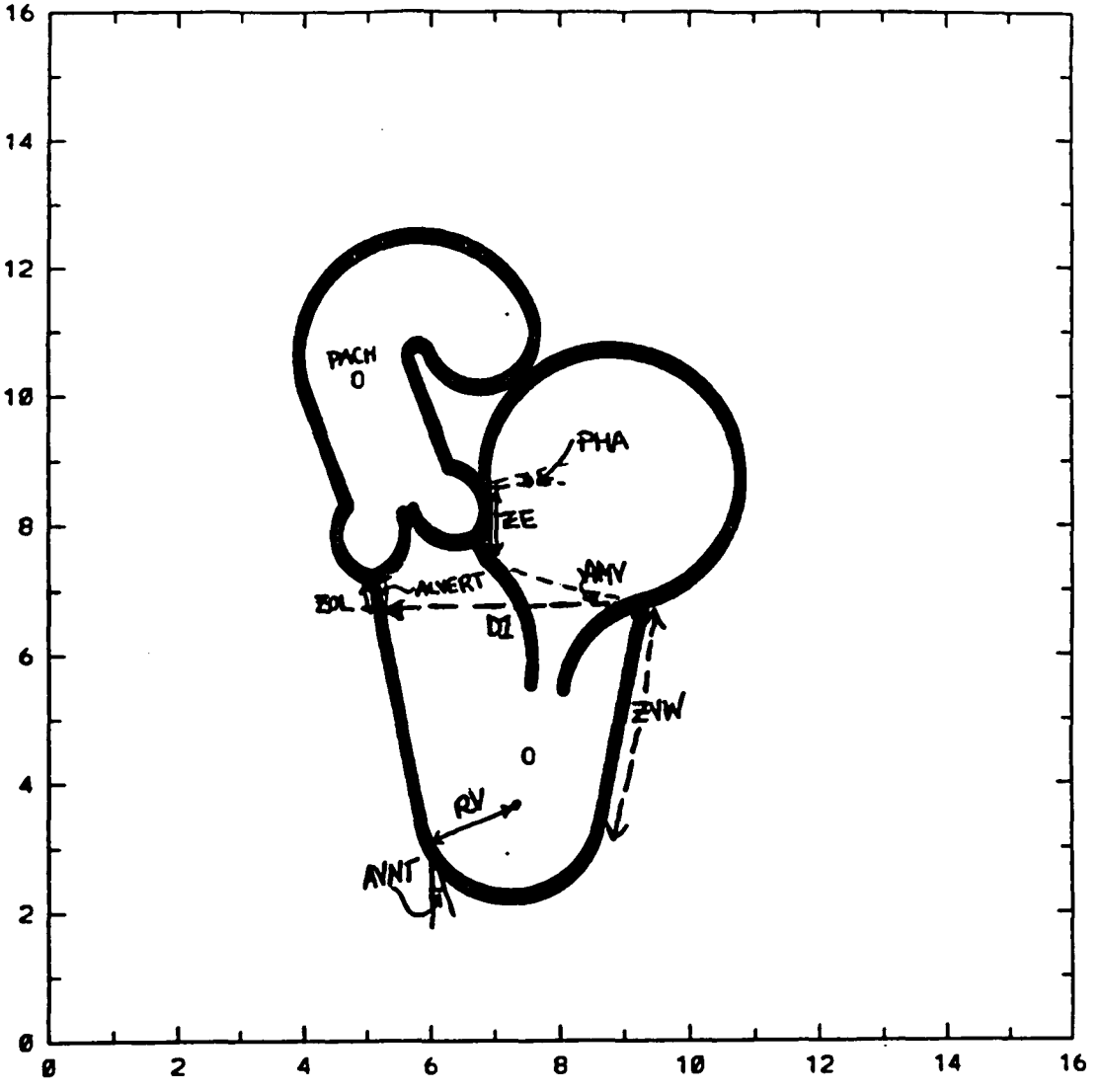

Figure 2.2 Initial Geometry of Aortic Structures

This is an enlargment of Figure 1 to better visualize the aortic construction. The parameters used in this construction are as follows:

DAORTA is the diameter of the aortic ring,

DSM is the widest diameter across the aortic sinuses,

H is the height of the aortic sinus, and

COAPT is the length of overlap (coaptation) between the two aortic leaflets.

PAL is the angle between the aortic ring and a line drawn between the aortic leaflet attachment point and the beginning of the **COAPT** segment of the leaflets.

ZASCis the length of the ascending aorta,

ARCHANL is the angle of the aortic arch,

RARCH is the radius of the aortic arch, and

FARCH is the factor relating the radius of the aortic arch to the aortic diameter.

Figure 2.2 Initial Geometry of Aortic Structures

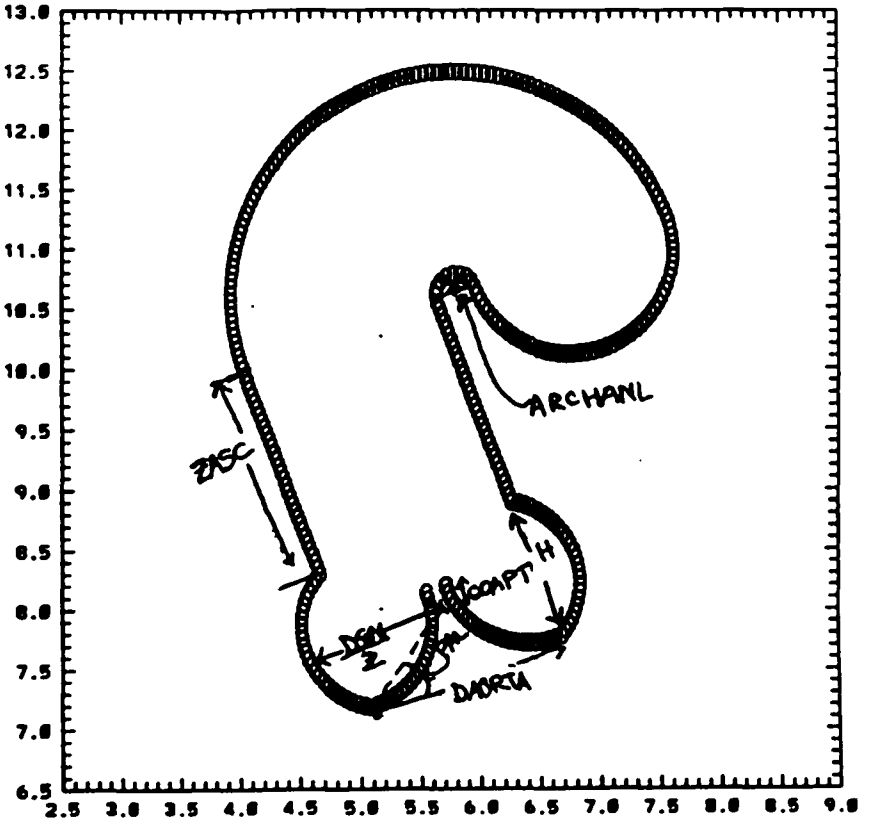

Figure 2.3 Plots of flow (cc/sec) versus time, two computational heartbeats

Upper panels illustrate the flow through the mitral valve: the left panel is flow through the mitral annulus or ring, and corresponds to the level of flow measured by electromagnetic flowmeters. The upper right panel illustrates flow through the mitral cusp (between the leaflets tips); this is flow actually moving from the atrium to the ventricle. See text for further explanation.

Lower panels similarly illustrate aortic ring (left panel) and aortic cusp (right panel).

Figure 2.3 Mitral and Aortic Flow versus Time, Two Beats

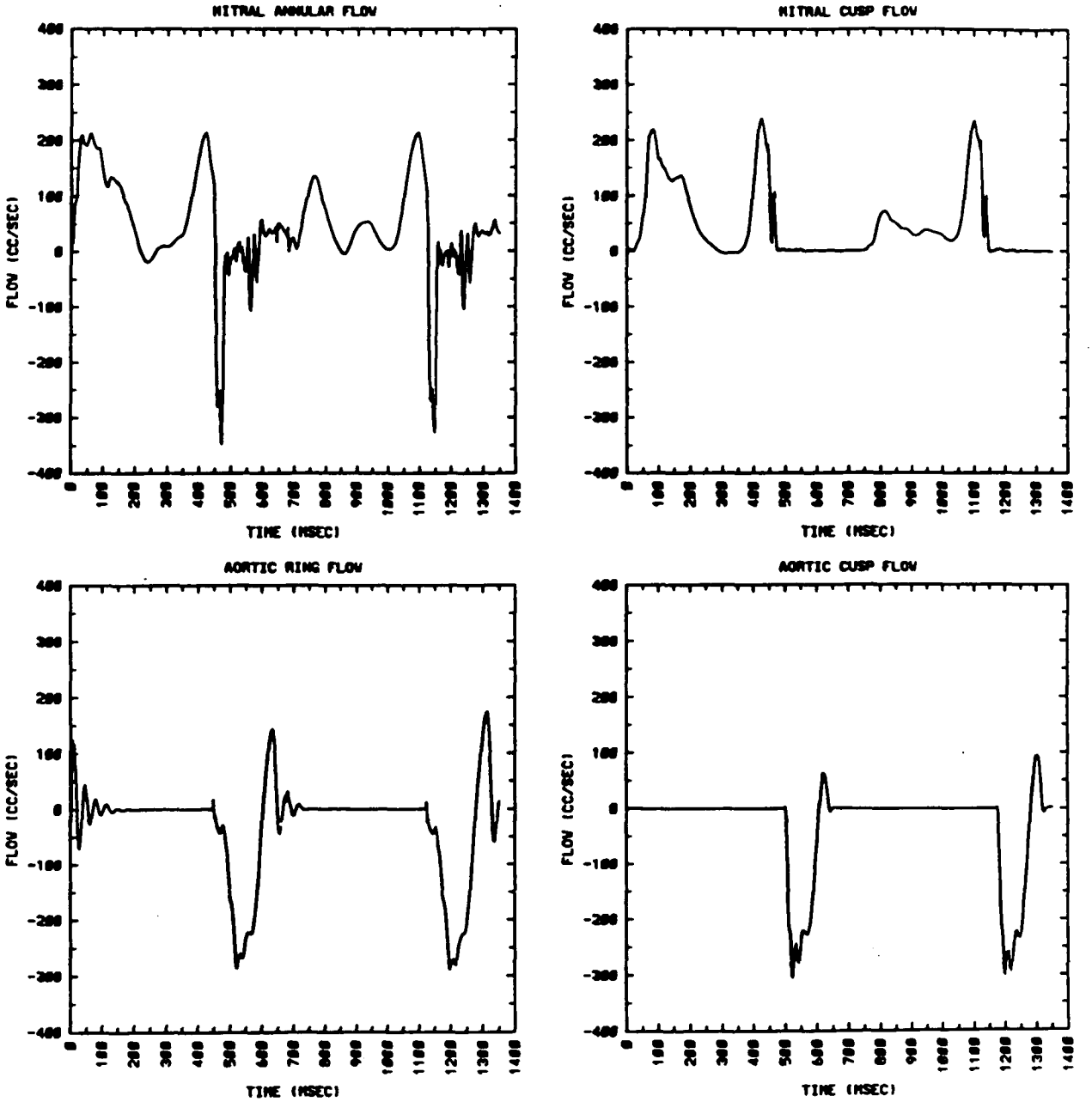

Figure 2.4 Atrial, Ventricular and Aortic Pressures versus Time

During diastole (until t= 450 msec), the atrial and ventricular pressures are very similar (bottom two curves), and actually cross over more than once. The atrial pressure is greater than ventricular pressure during atrial systole; this is followed by a large increase in ventricular pressure, which peaks at about 80 mm Hg. Note the oscillations in the atrial pressure trace during ventricular systole (lowest curve).

The curve which is approximately constant (following initial damped oscillations) corresponds to aortic sink pressure *not* the pressure measured across the aortic valve. This pressure inceases about 60 mm Hg during ventricular systole, then decreases to about 30 mm Hg before returning to its baseline.

Figure 2.4 Atrial, Ventricular and Aortic Pressure versus Time

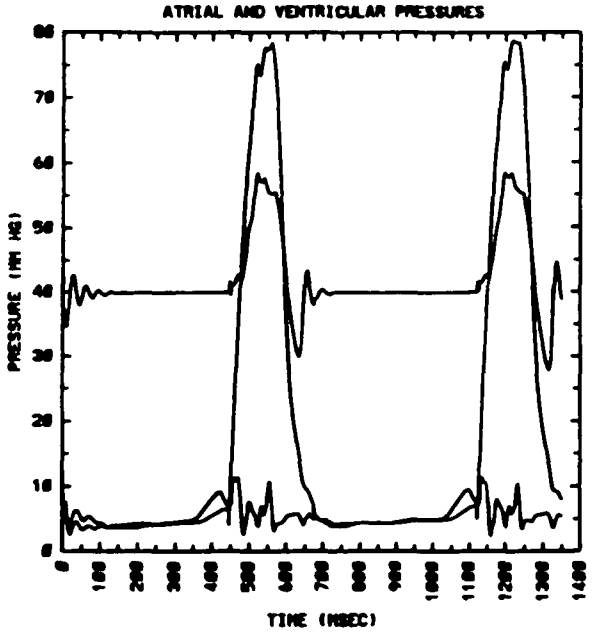

Figure 2.5 Mitral and Aortic Velocity (cm/sec) versus Time

As is Figure 3, the upper panels represent flow velocity through the mitral valve (ring shown on left, cusp shown on right), and the lower panels represent flow velocity through the aortic valve (again, ring velocity on the left and cusp velocity on the right).

Figure 2.5 Mitral and Aortic Velocity versus Time

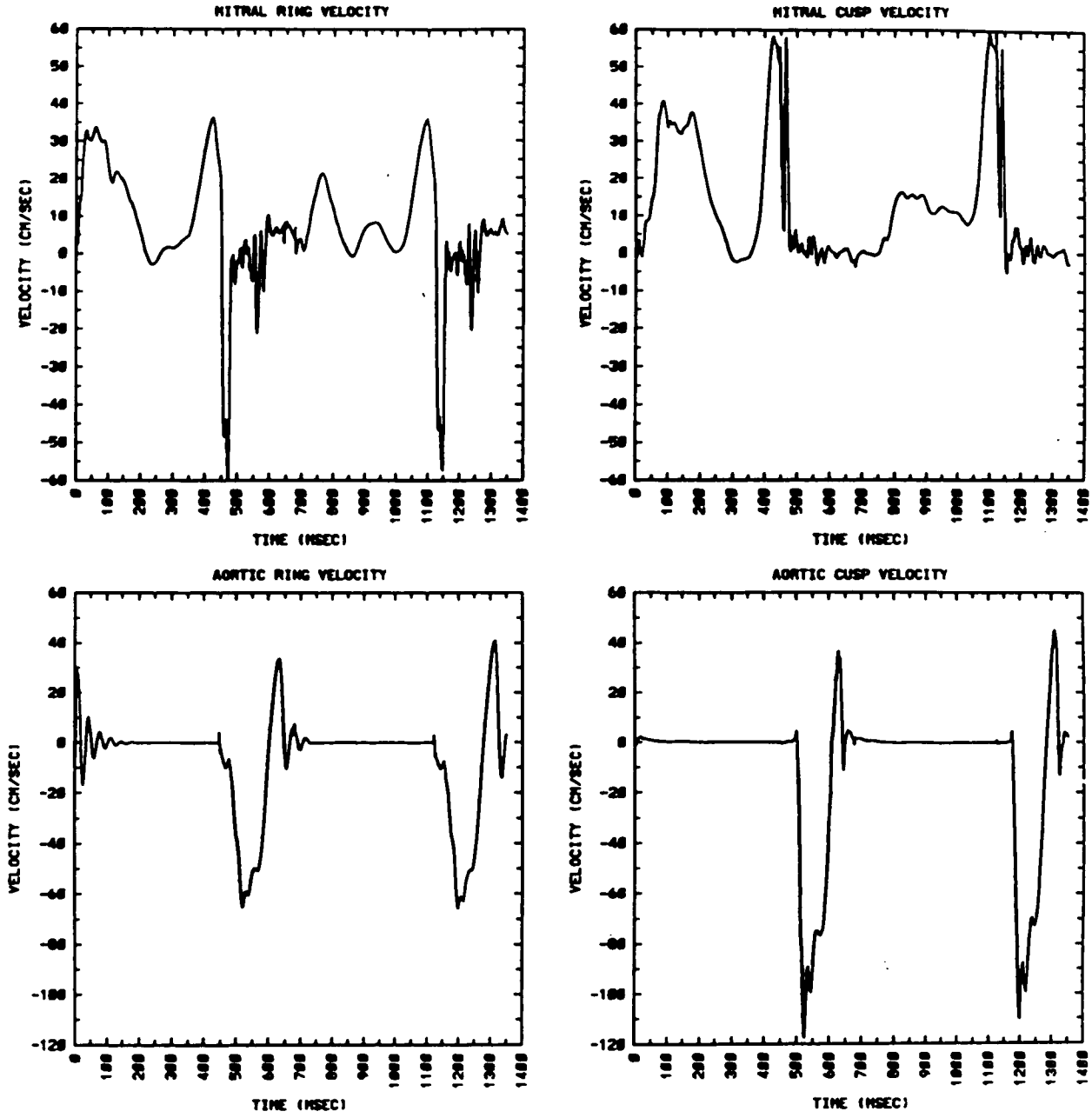

Figure 2.6 Atrial Inflow and Aortic Outflow versus Time, together with cardiac chamber volumes.

Upper left panel represents the atrial inflow (top curve during diastole), and aortic source flow which can be seen to oscillate about zero as the aorta is "charges" during the first few timesteps. Aortic outflow peaks at about 250 cc/sec during systole. Aortic sink flow becomes negative for a short time at the the end of systole, corresponding to flow *into* the aorta. Note that this is only transient, however.

Upper right panel represents the same data as in the upper left panel, but now integrated versus time to give total flow volume through the atrial source (top curve) and through the aortic sink (bottom curve). The difference between these two curves at the end of a heartbeat should be the change in total heart volume. Here, this difference is about 8 cc for the first heart beat and 11 cc over two heartbeats.

Lower left panel represents cardiac chamber volumes versus time.

Bottom curve: atrial volume

Second curve from bottom: aortic volume (note, this is constant throughout, as desired

Second curve from top: ventricular volume

Top curve: total volume (sum off all three previous curves)

The atrium can be seen to have decreased in volume by about 10 cc, and the ventricle to have increased in volume by about 15 cc, with a net increase in volume of about 5 cc.

Figure 2.6 Source/Sink Flow and Chamber Volumes vs Time

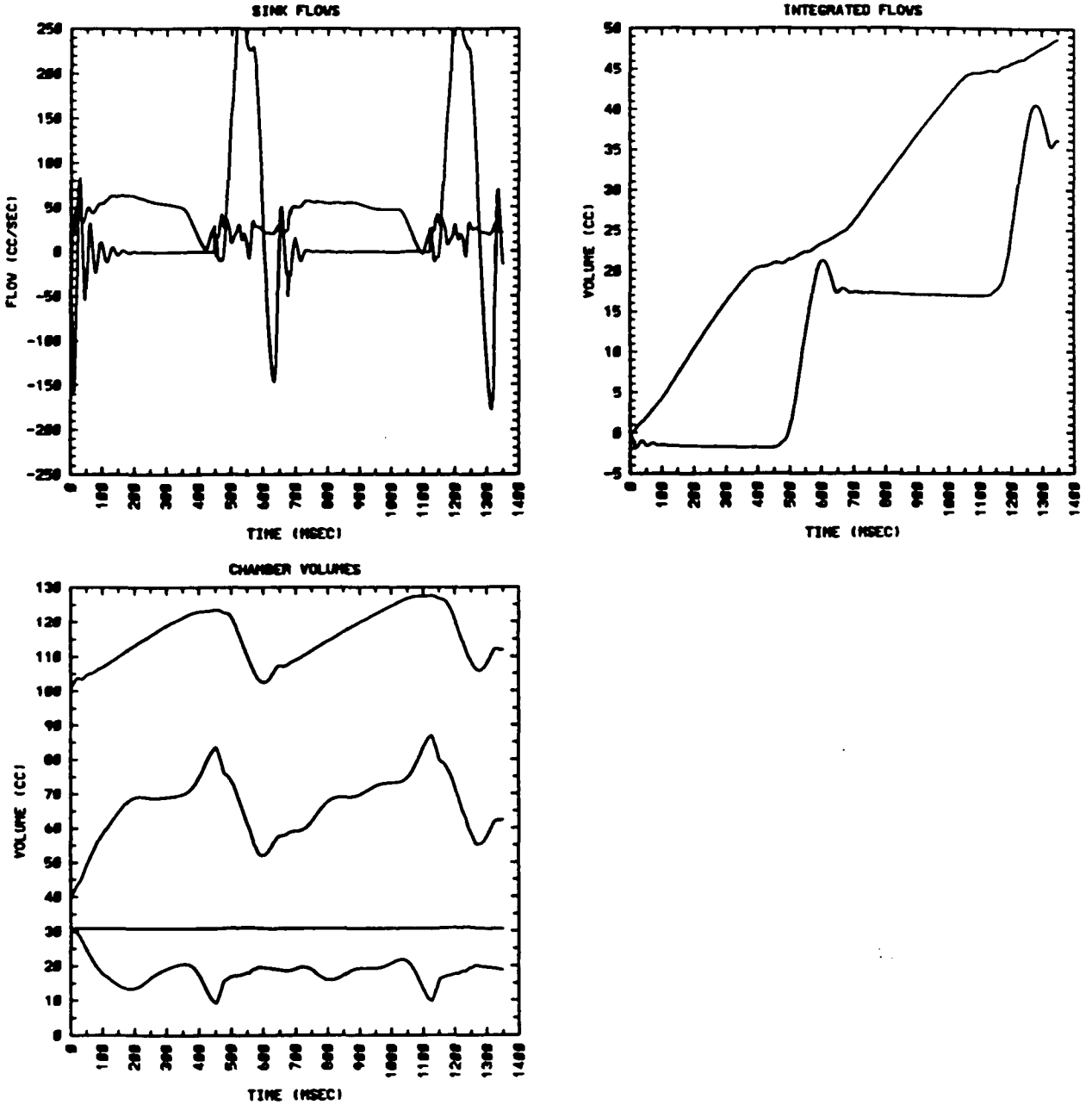

Figure 2.7 Diameters (cm) of mitral and aortic ring and cusp versus time

The left panel illustrates the mitral ring diameter (upper curve) and the mitral cusp diameter or leaflet tip separation (bottom curve).

The mitral ring diameter decreases during systole, helping to retain competent mitral valve closure. The increasing leaflet tip separation represents mitral valve opening. Note that a there is a mid-diastolic extra peak, although inter-leaflet is still positive. See text for further discussion.

The right panel illustrates aortic ring diameter (upper curve) and aortic cusp diameter (lower curve). Aortic ring diameter remains essentially constant except for a small increase during ventricular systole. The aortic leaflets remain together throughout diastole, opening between 500 and about 650 msec, and between 1175 and 1300 msec during the second heartbeat.

Figure 2.7 Mitral and Aortic Valve Diameters at Ring and Cusp

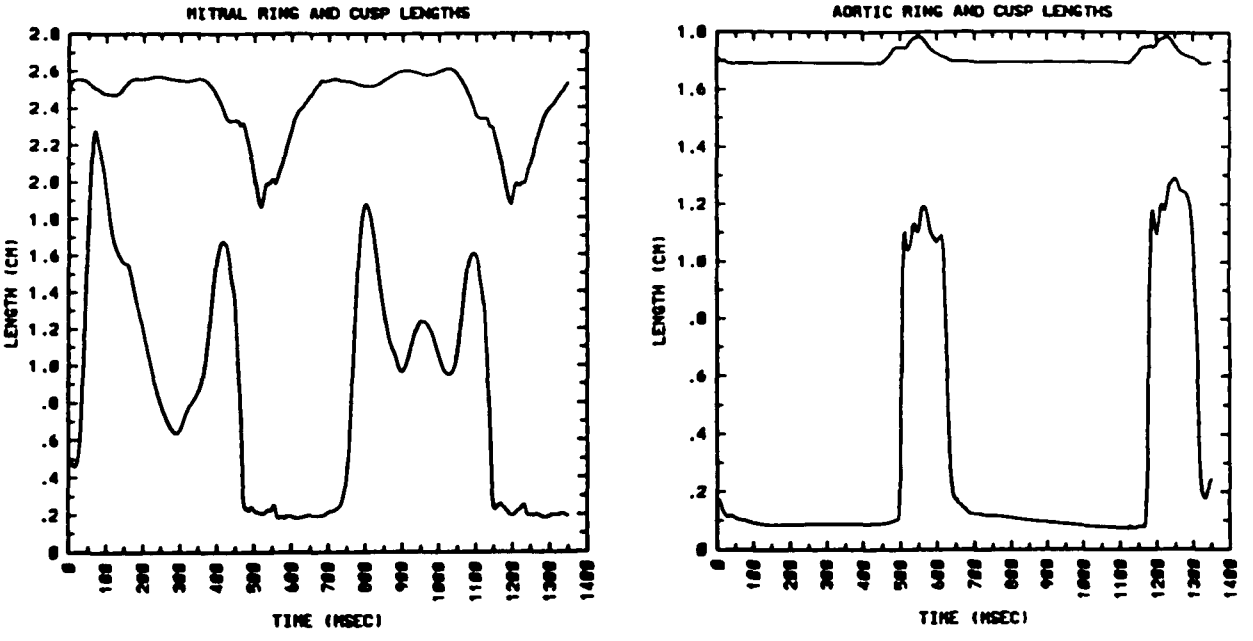

Figure 2.8 Tensions in Mitral and Aortic Support Structures vs Time

Left panel plots the tensions in the mitral chordae (lower two curves) and papillary muscle (upper curve). Note the low tensions in each throughout diastole, followed by the increased systolic tensions as these structures prevent the valve from prolapsing into the atrium.

Right panel plots the tensions in the artificial aortic chordae. Following the initial damped oscillations, the tensions remain relatively constant throughout diastole, and decrease to zero while the aortic valve is open during systole (at about 500 to 600 msec, and then again from about 1175 to 1300 msec).

Figure 2.8 Tensions in Mitral and Aortic Support Structures vs Time

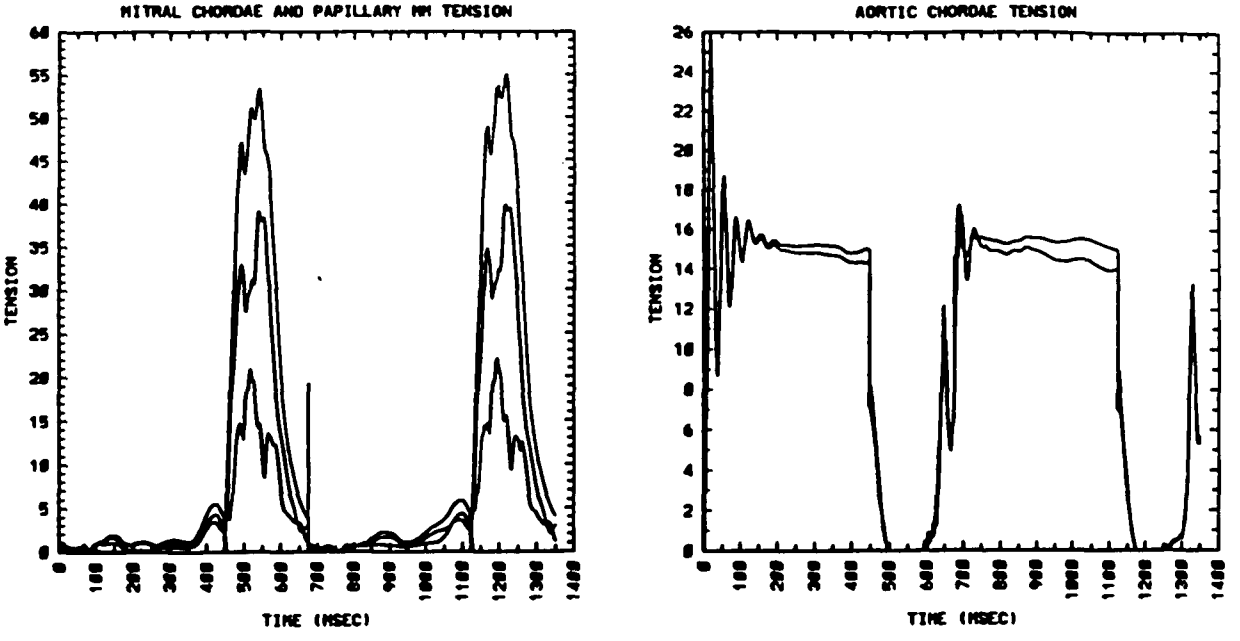

Figure 2.9 Frames illustrating heart boundary and flow streamlines at four different, equally-spaced, timesteps during early diastole.

Formats of Figures 10 through 20 are identical

The times represented here are: 28 msec (160 timesteps), upper left panel;

56 msec (320 timesteps), upper right panel;

84 msec (480 timesteps), lower left panel;

112 msec (640 msec), lower right panel.

The atrial source location is indicated by the clear area in the center of the atrium, the aortic sink by the clear area in the tail of the descending aorta. These are connected by cuts to the external sink, here through the right half of the frames. The reason for this are that in the presence of sources and sinks, the divergence is nonzero and a streamfunction cannot be constructed. See text for further details.

One can follow the opening of the mitral valve through these frames, together with the increasing volume of t ıe ventricle. The streamlines within the aorta in the first frame correspond to aortic filling from the aortic 'sink' to establish the set aortic pressure.

Compare the particu ar time frames to the corresponding time in Figures 3 through 8 to determine where in the cardiac cycle these frames are.

See text for frame-by frame details.

Figure 2.9 Early Diastolic Heart Boundary and Streamlines

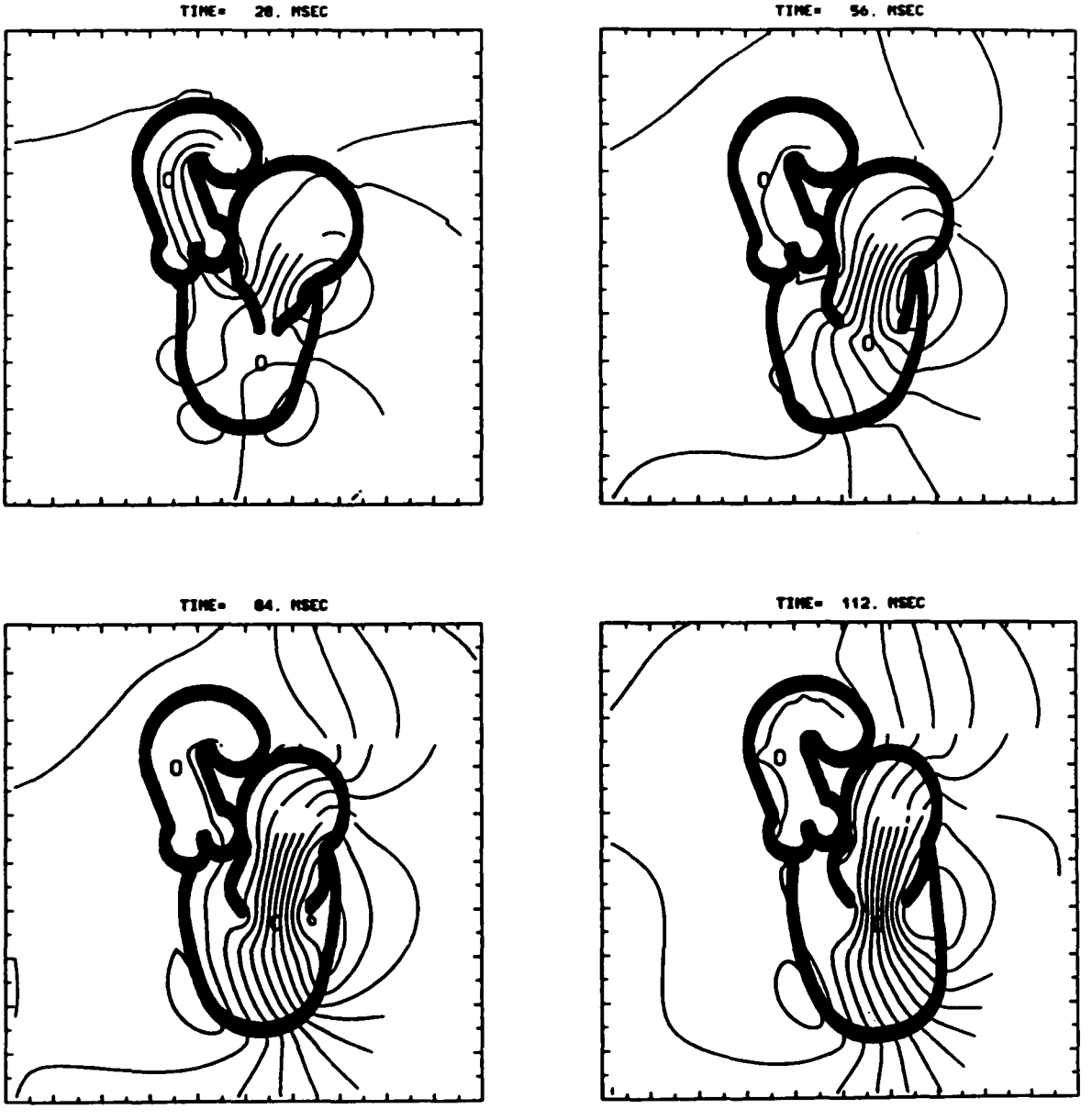

Figure 2.10 Heart Boundary and Streamlines, Early to Mid-Diastole

140 msec, upper left panel;

169 msec, upper right panel;

197 msec, lower left panel;

225 msec, lower right panel

Figure 2.10 Early to Mid-Diastolic Heart Boundary and Streamlines

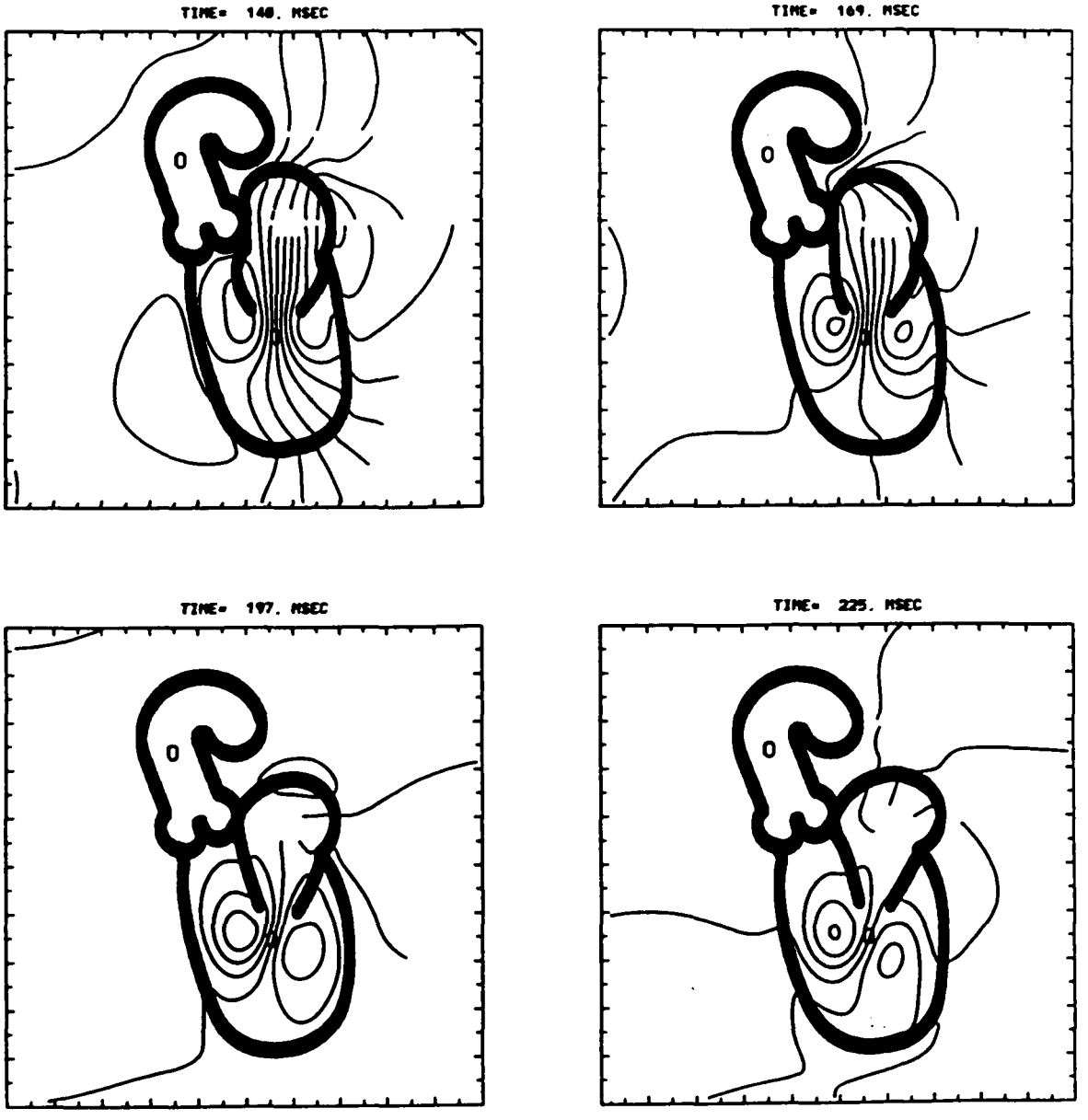

Figure 2.11 Heart Boundary and Streamlines, Mid-Diastole

253 msec, upper left panel;

281 msec, upper right panel;

309 msec, lower left panel;

337 msec, lower right panel

Figure 2.11 Mid-Diastolic Heart Boundary and Streamlines

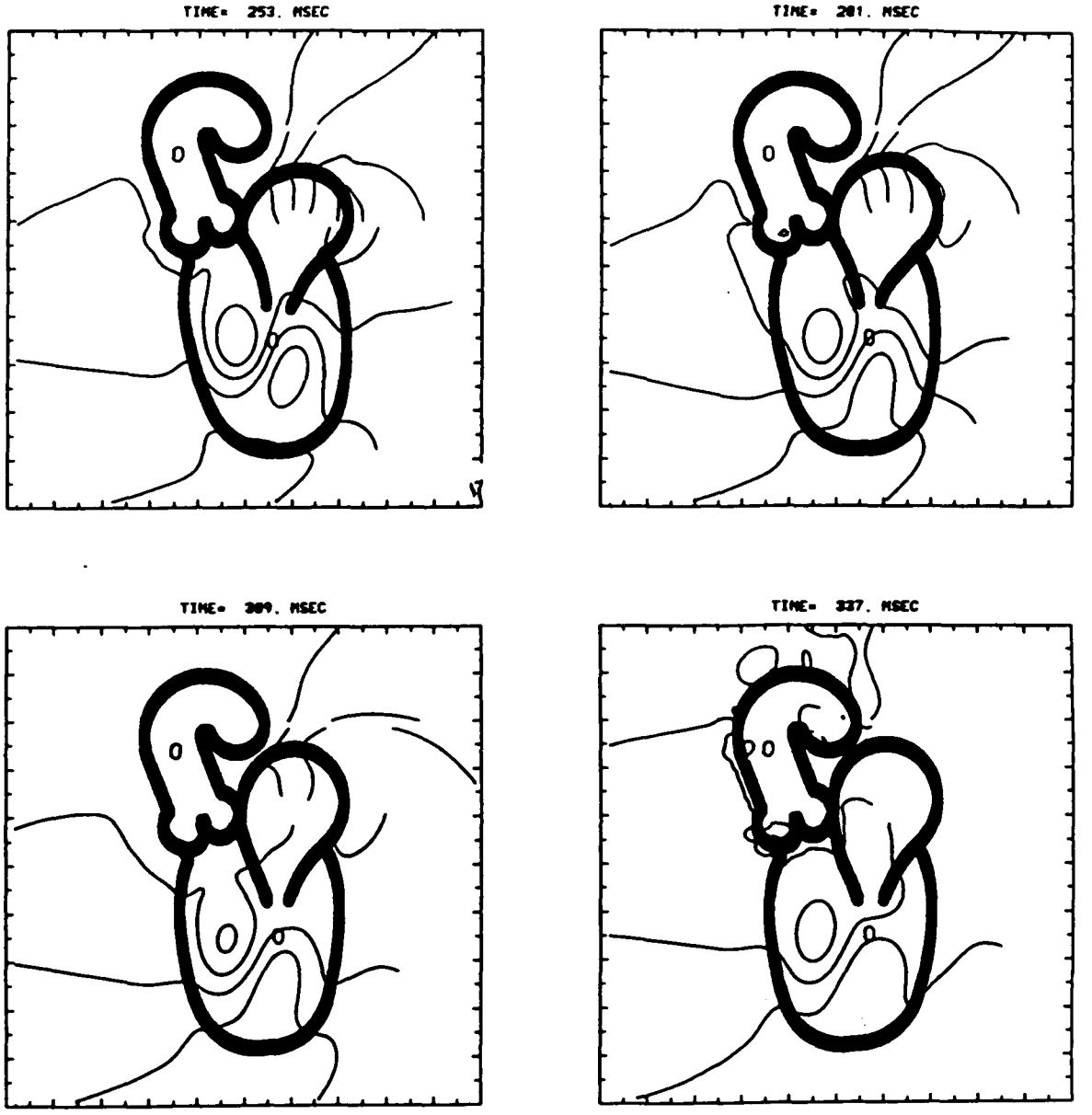

Figure 2.12 Heart Boundary and Streamlines, Atrial Contraction

365 msec, upper left panel;

394 msec, upper right panel;

422 msec, lower left panel;

450 msec, lower right panel

Figure 2.12 Heart Boundary and Streamlines during Atrial Contraction

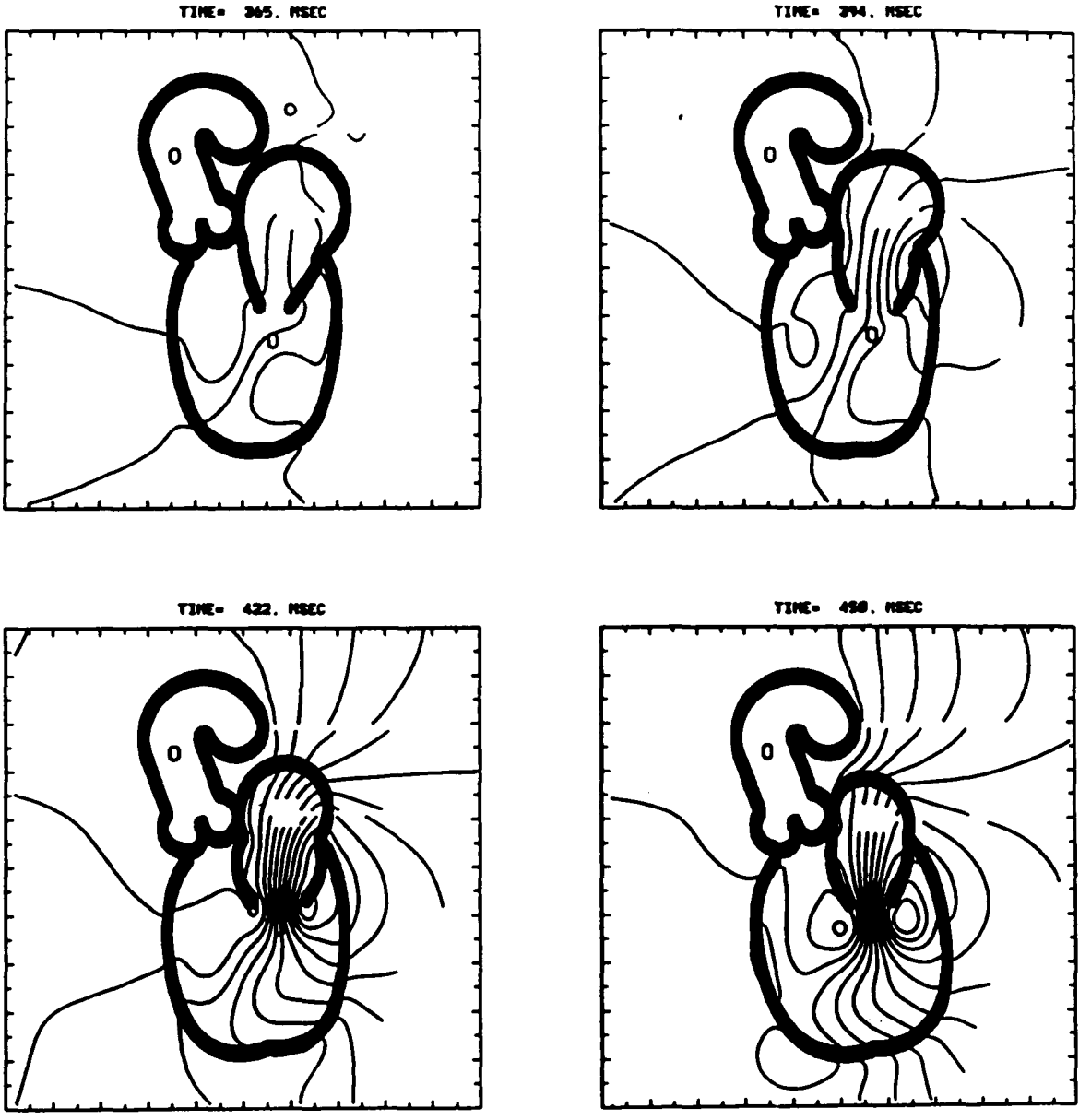

Figure 2.13 Heart Boundary and Streamlines, Ventricular Systole

478 msec, upper left panel;

506 msec, upper right panel;

534 msec, lower left panel;

562 msec, lower right panel

Figure 2.13 Heart Boundary and Streamlines during Ventricular Systole

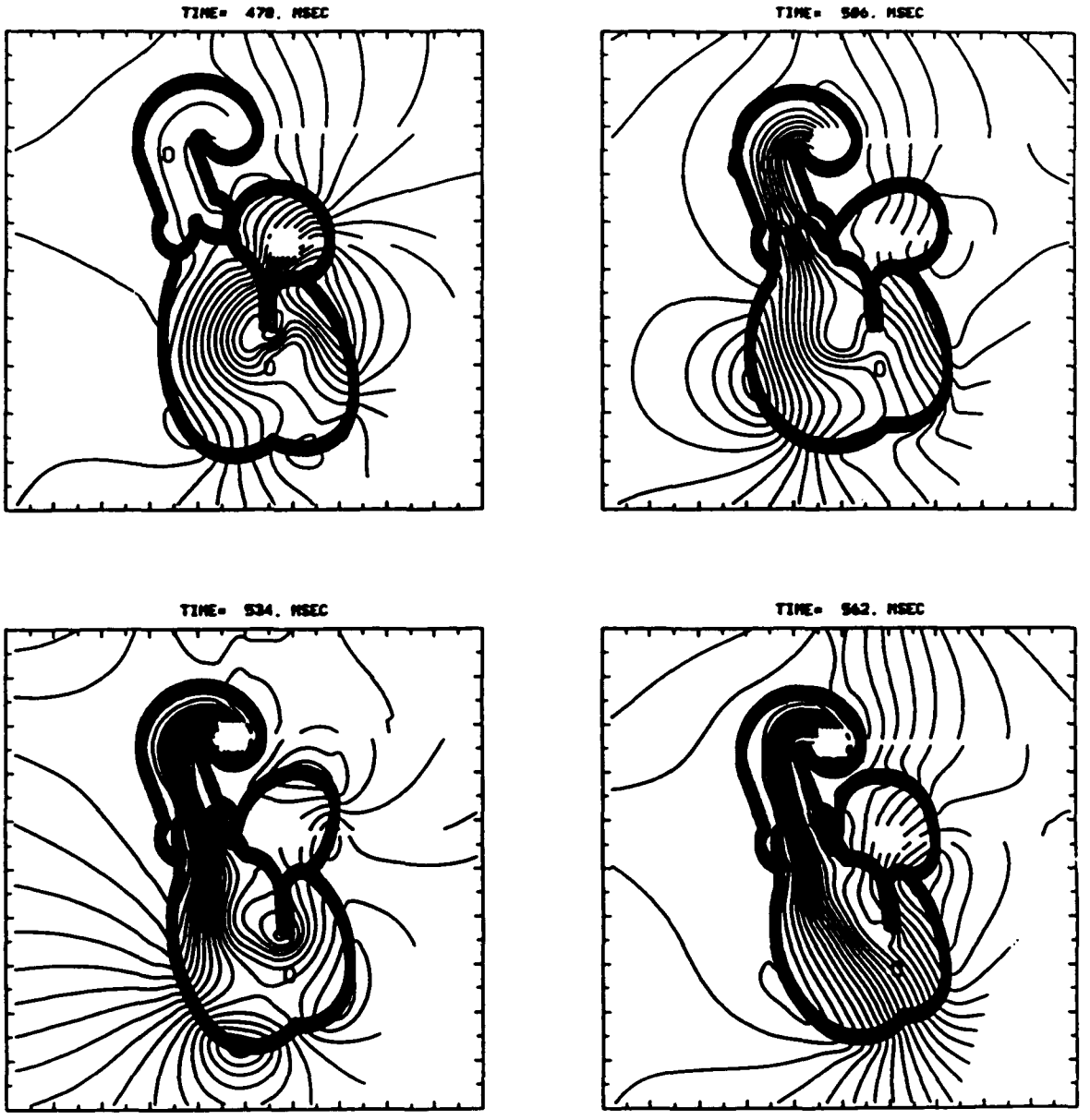

Figure 2.14 Heart Boundary and Streamlines, Aortic Valve Closure

590msec, upper left panel;

619 msec, upper right panel;

647 msec, lower left panel;

675 msec, lower right panel

This is the end of the first heartbeat (and the initial configuration for the second heartbeat).

Figure 2.14 Heart Boundary and Streamlines during Aortic Closure

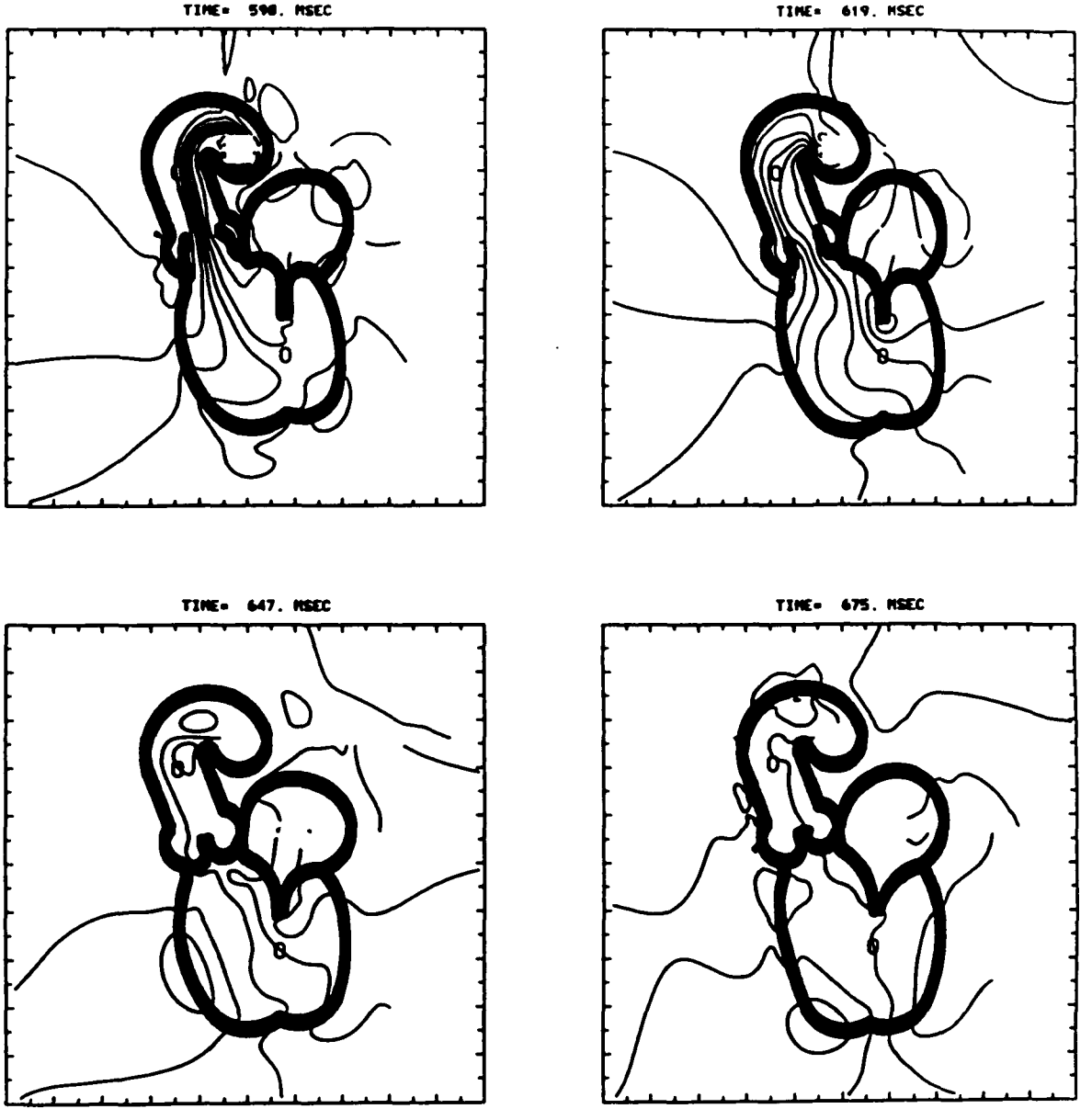

Figure 2.15 Heart Boundary and Streamlines, 2nd Beat, Early Diastole

703 msec, upper left panel;

731 msec, upper right panel;

759 msec, lower left panel;

787 msec, lower right panel

Figure 2.15 Heart Boundary and Streamlines. 2nd Beat, Early Diastole

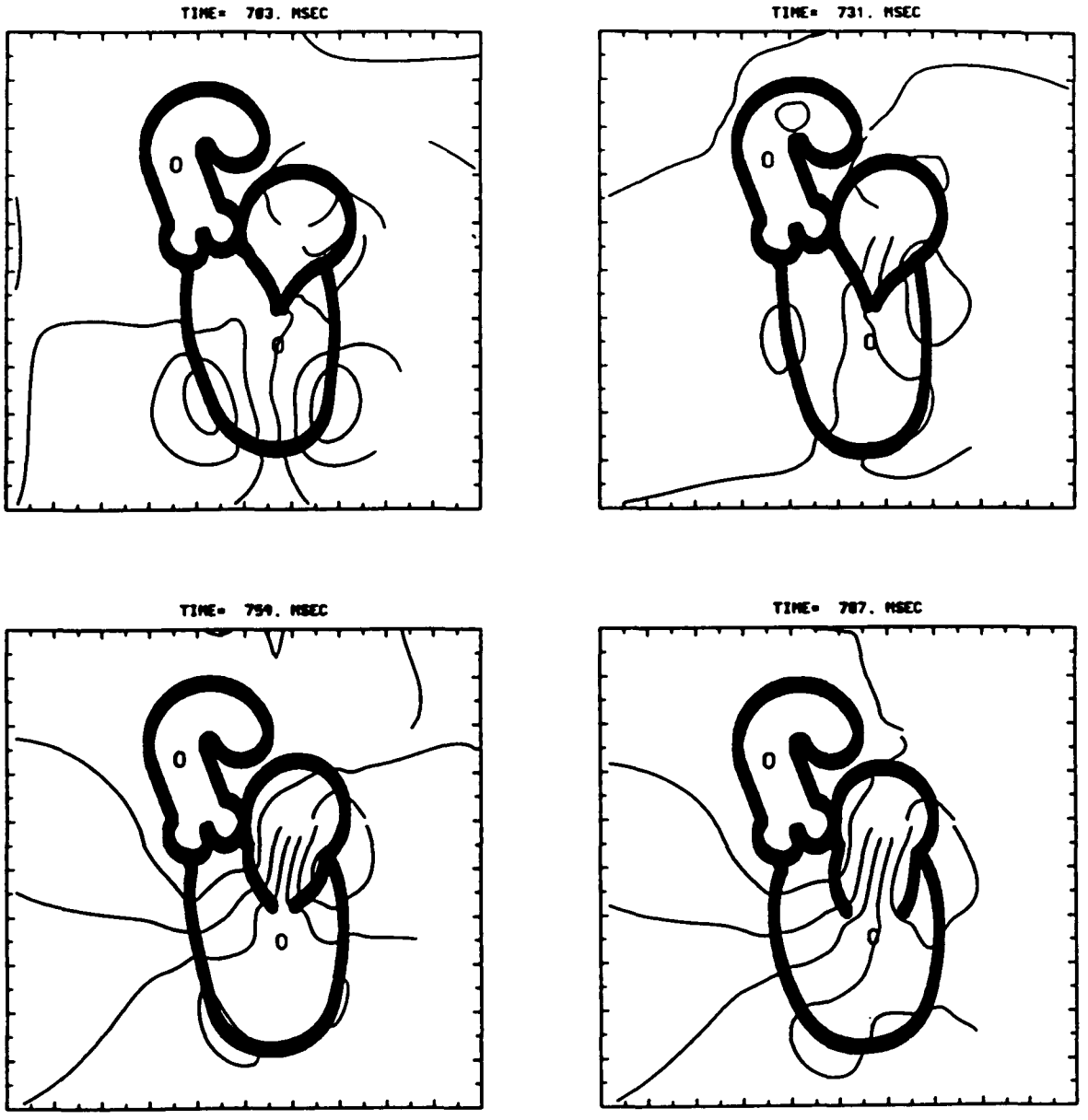

Figure 2.16 Heart Boundary and Streamlines, 2nd Beat, Early to Mid-Diastole

815 msec, upper left panel;

844 msec, upper right panel;

872 msec, lower left panel;

900 msec, lower right panel

Figure 2.16 Heart Boundary and Streamlines, 2nd Beat, Early to Mid-Diastole

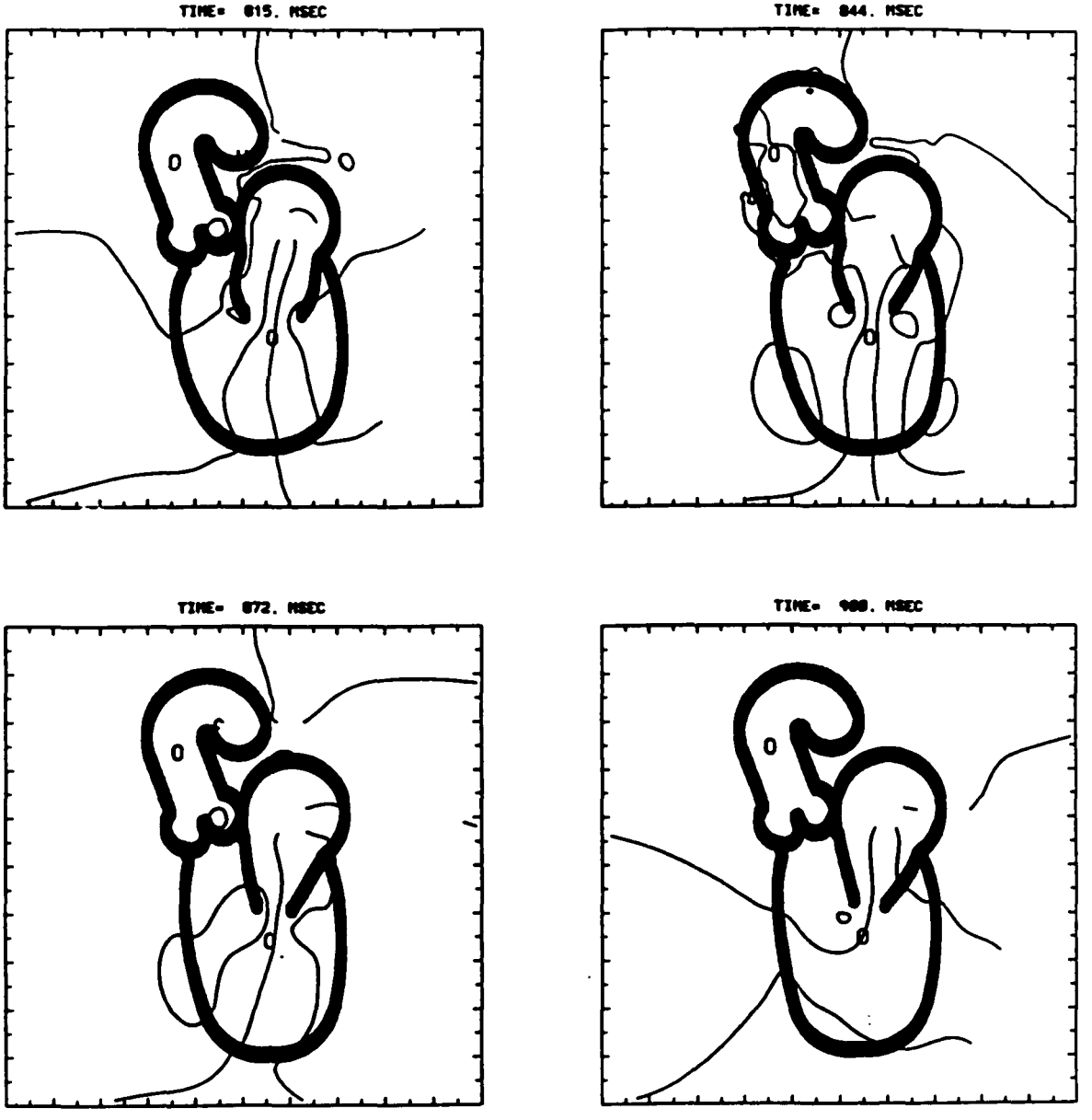

Figure 2.17 Heart Boundary and Streamlines, 2nd Beat, Mid-Diastole

928msec, upper left panel;

956 msec, upper right panel;

984 msec, lower left panel;

1012 msec, lower right panel

Figure 2.17 Heart Boundary and Streamlines, 2nd Beat, Mid-Diastole

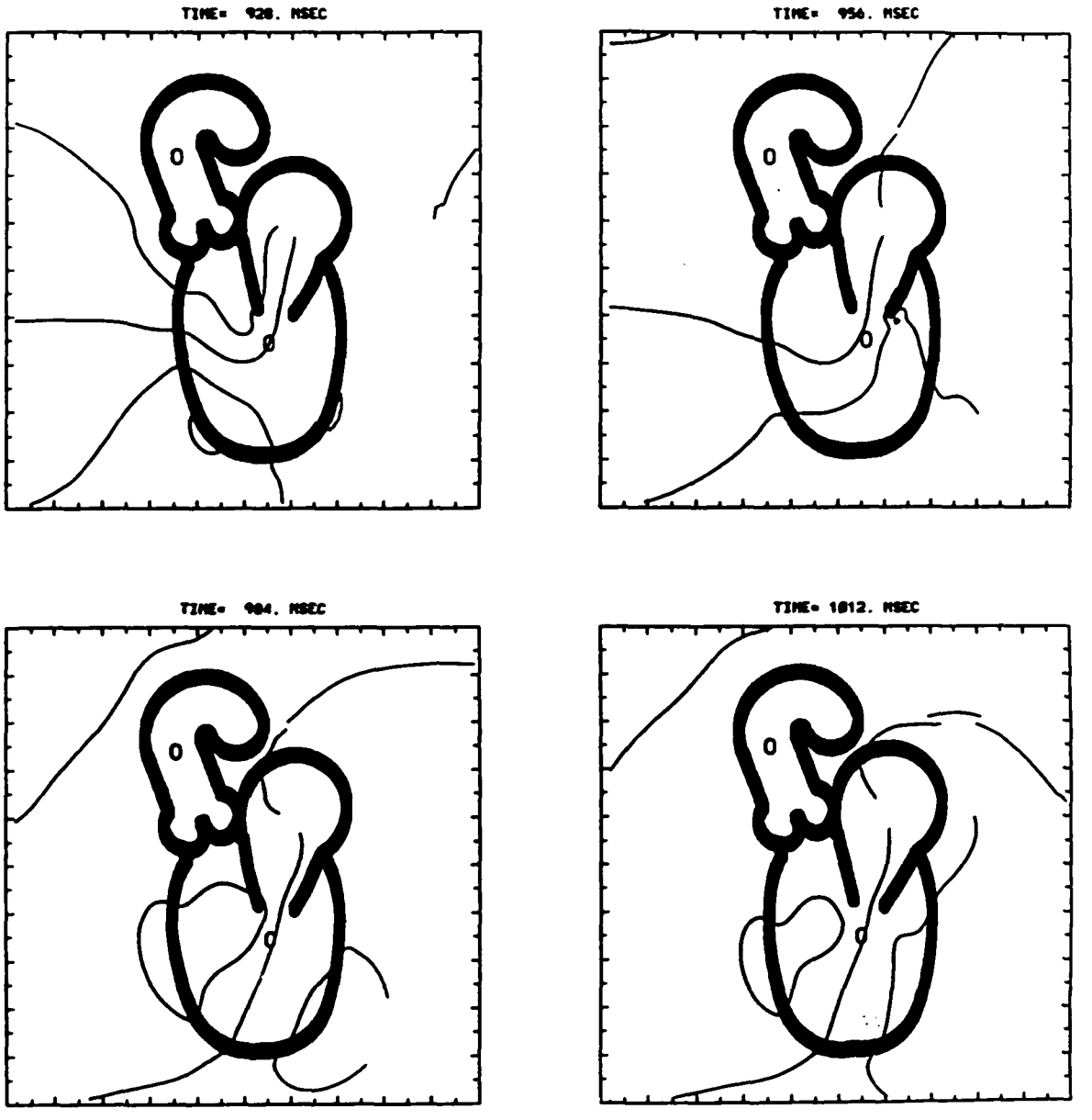

Figure 2.18 Heart Boundary and Streamlines, 2nd Beat, Atrial Contraction

1040 msec, upper left panel;

1069 msec, upper right panel;

1097 msec, lower left panel;

1125 msec, lower right panel

Figure 2.18 Heart Boundary and Streamlines, 2nd Beat, Atrial Contraction

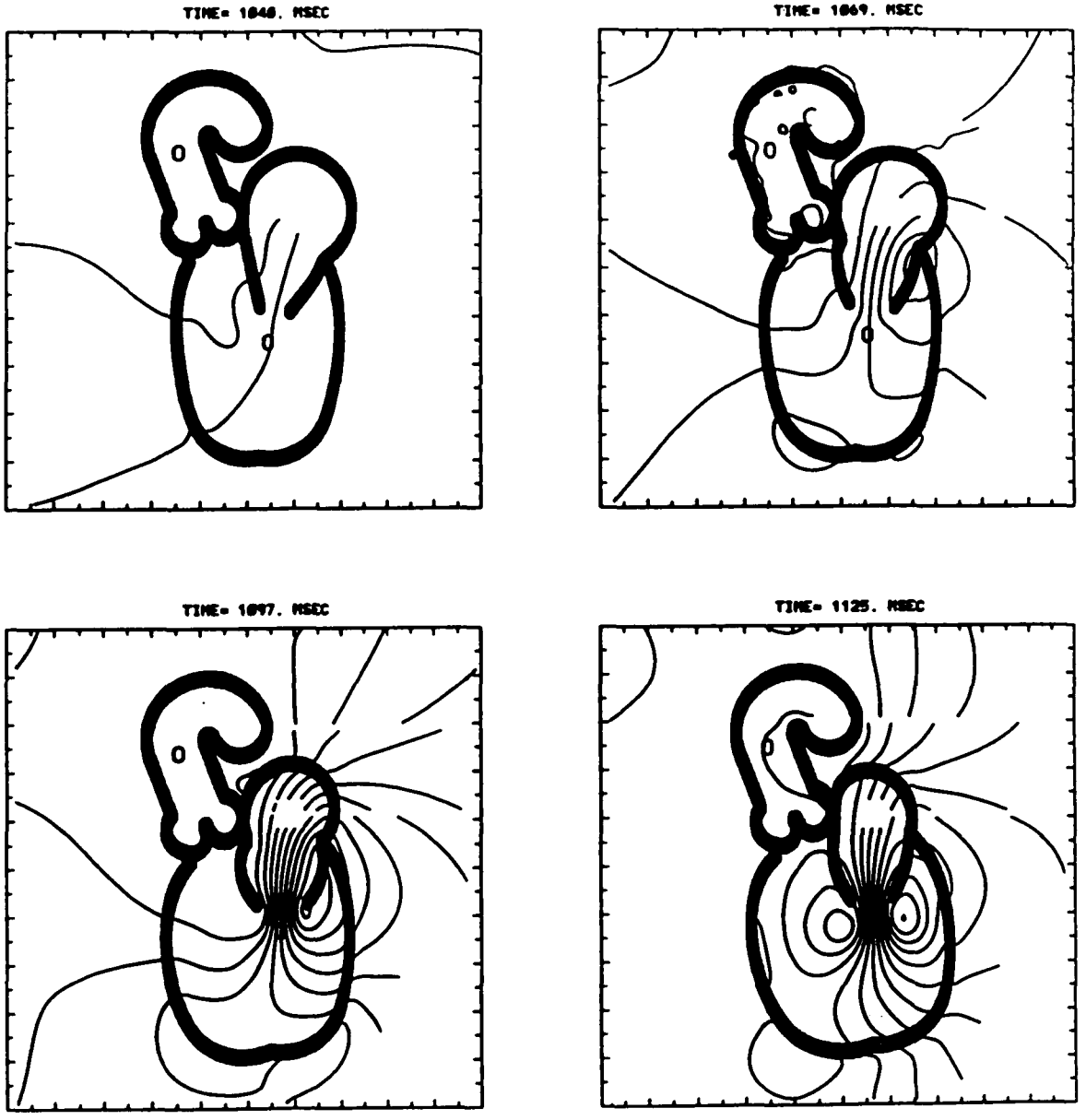

Figure 2.19 Heart Boundary and Streamlines, 2nd Beat, Ventricular Systole

1153 msec, upper left panel;

1181 msec, upper right panel;

1209 msec, lower left panel;

1237 msec, lower right panel

Figure 2.19 Heart Boundary and Streamlines, 2nd Beat, Ventricular Systole

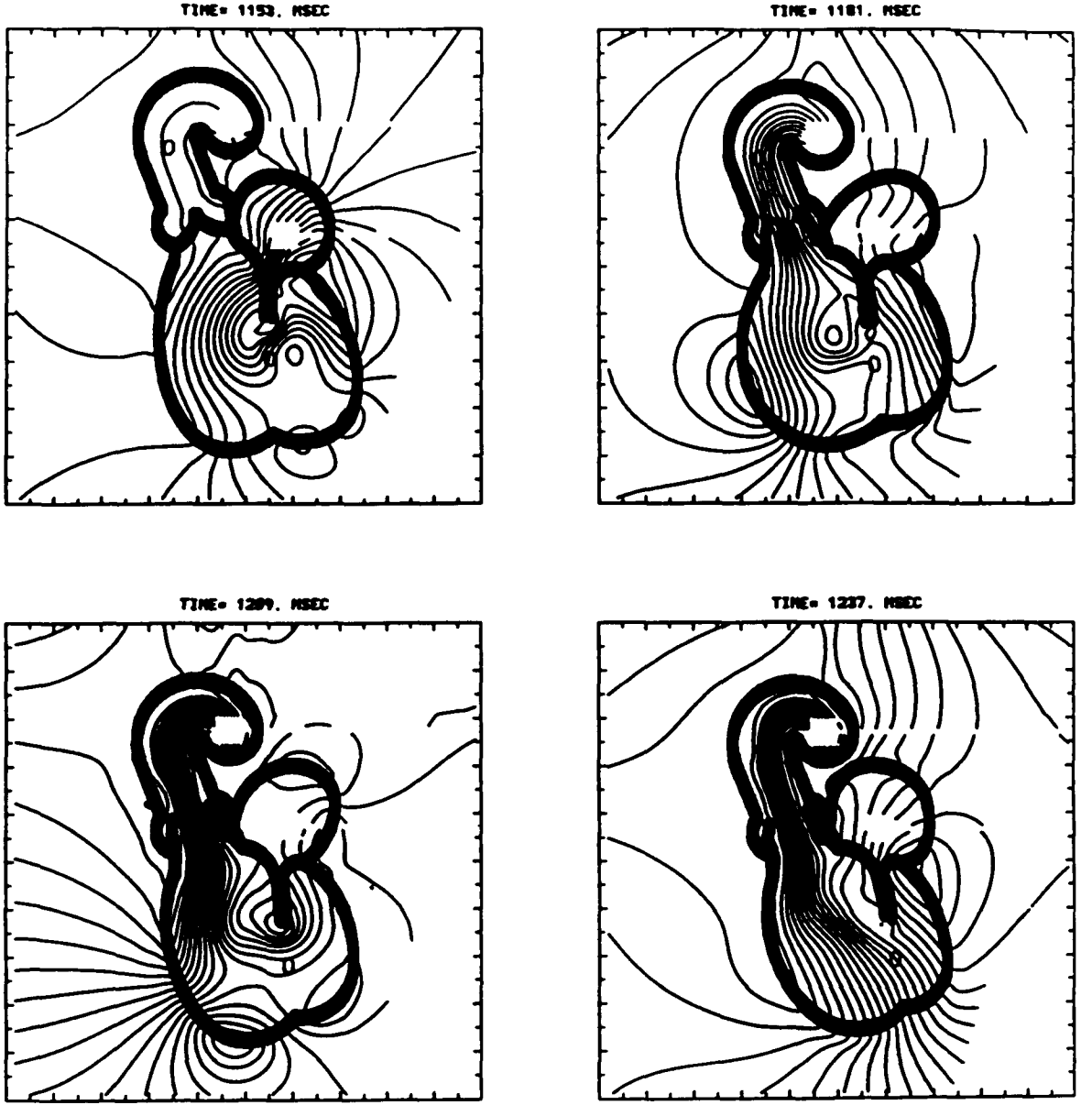

Figure 2.20 Heart Boundary and Streamlines, 2nd Beat, Aortic Valve Closure

1265 msec, upper left panel;

1294 msec, upper right panel;

1322 msec, lower left panel;

1350 msec, lower right panel

Figure 2.20 Heart Boundary and Streamlines, 2nd Beat, Aortic Valve Closure

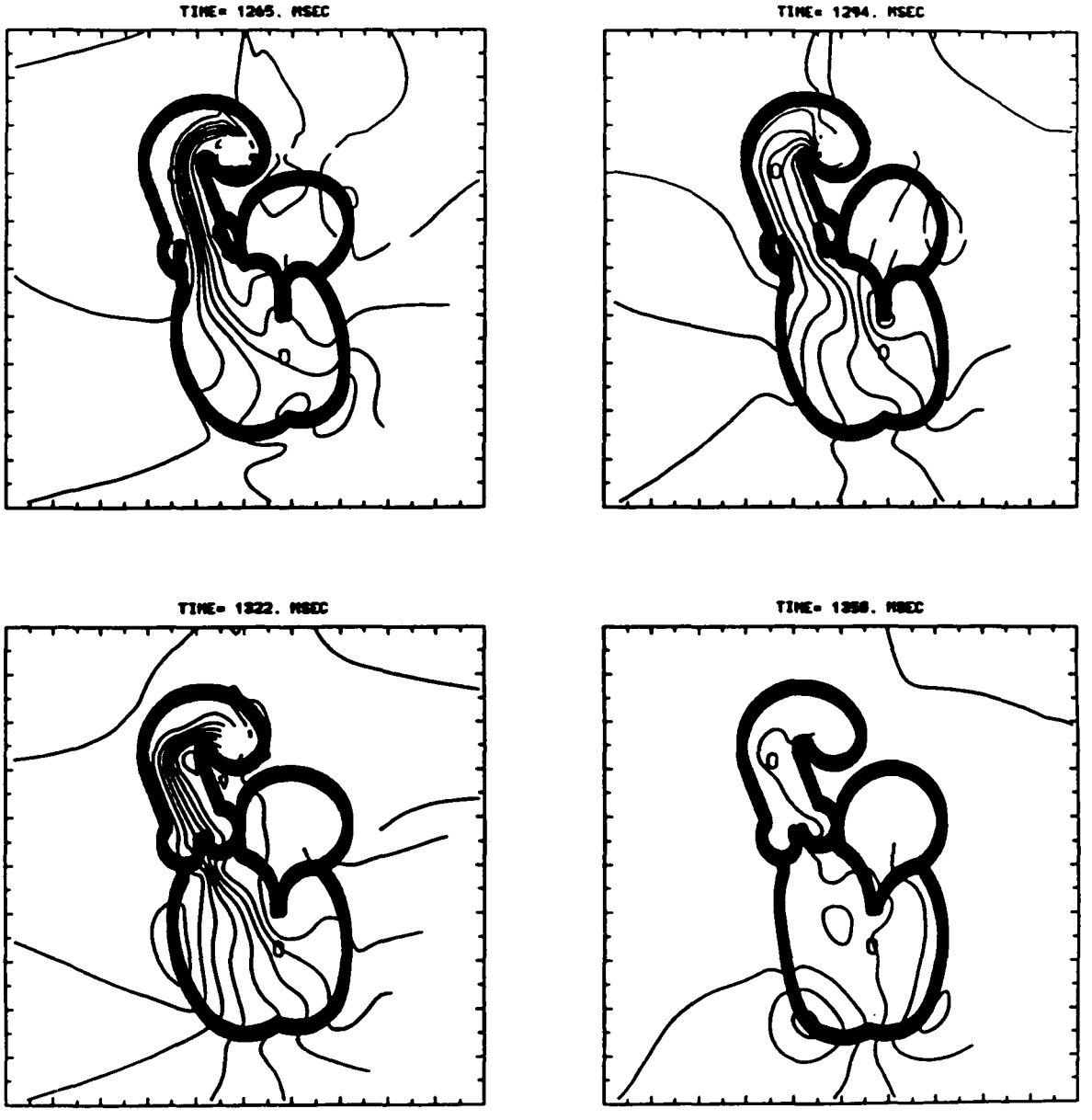

Figure 2.21A through 2.21G Heart Boundary and Fluid Markers, First Beat

Note unequal spacing; only frames that showed the most interesting results have been included.

2.21A 28 msec, early diastole to show initial configuration of fluid markers

2.21B 253 msec, mid-diastole, showing vortices forming behind the mitral leaflets

2.21C 534 msec, ventricular systole, illustrating the initial outflow of particles into the aorta

2.21D 590 msec, ventricular systole, with the aortic valve just beginning to close

2.21E 619 msec, ventricular systole, continued aortic valve closure

2.21F 647 msec, near end of ventricular systole, aortic valve now closed

2.21G 675 msec, last timestep before second heartbeat begins

Figure 2.21A Heart Boundary and Fluid Markers 1.

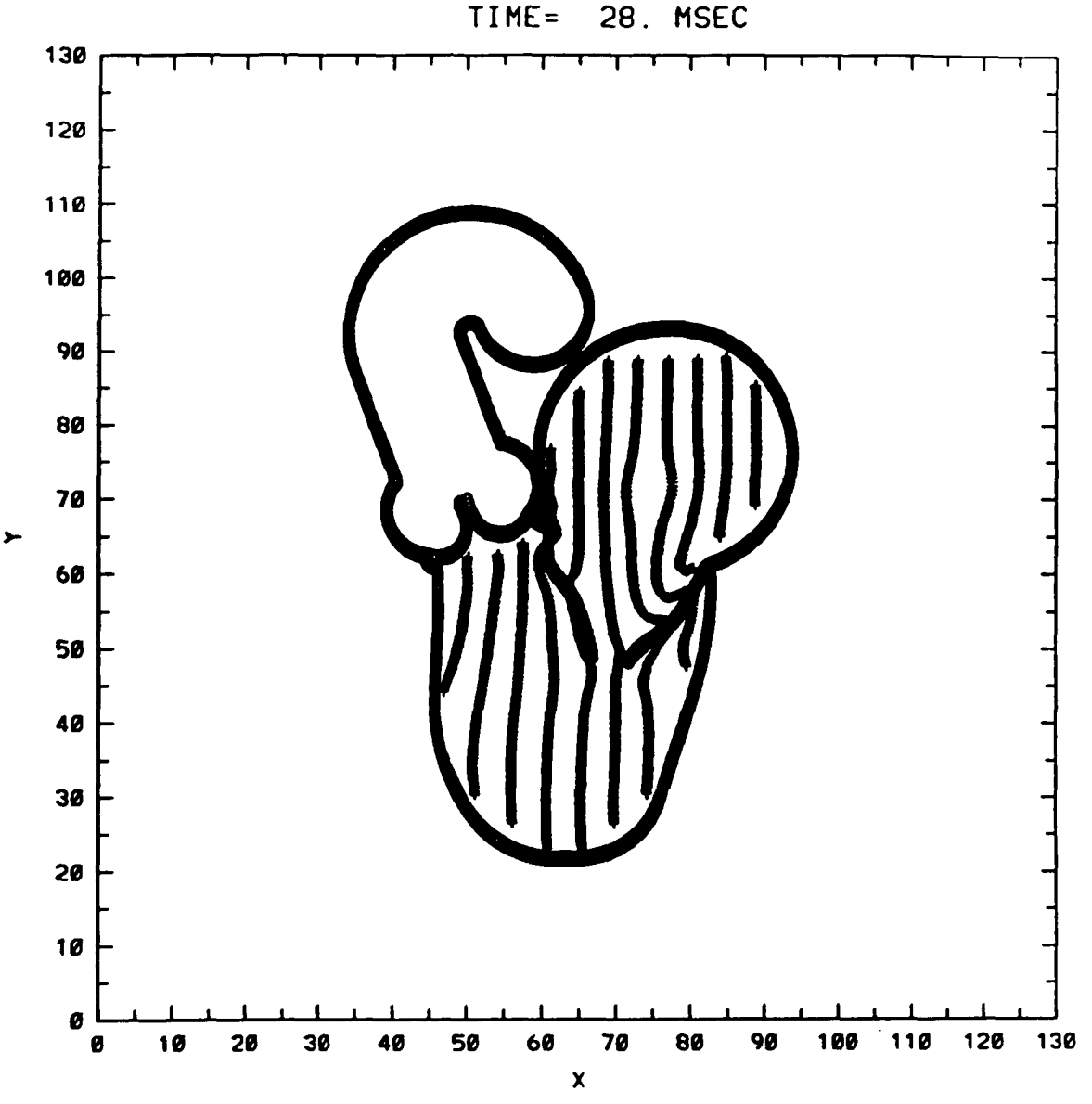

Figure 2.21B Heart Boundary and Fluid Markers 2.

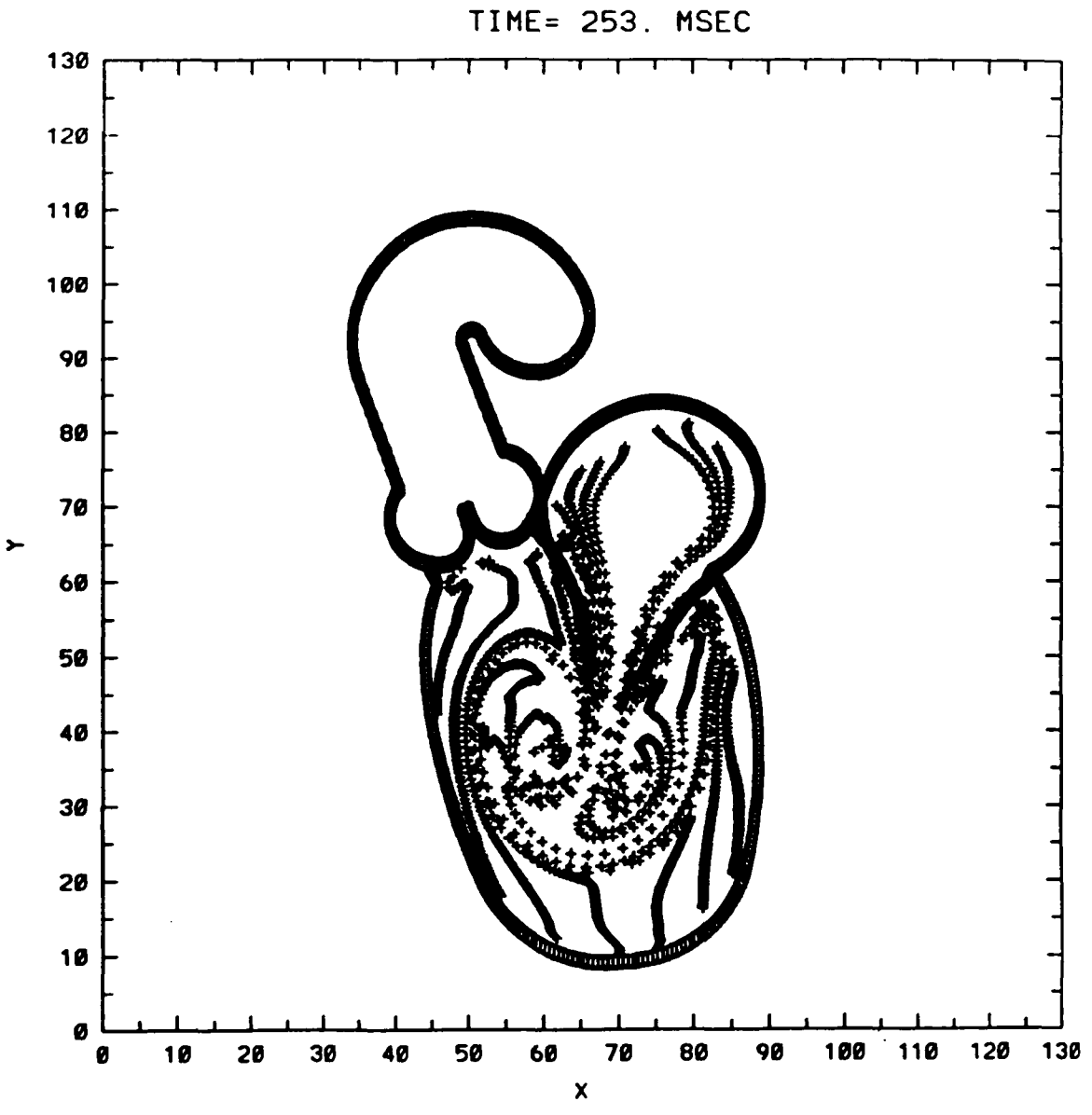

Figure 2.21C Heart Boundary and Fluid Markers 3.

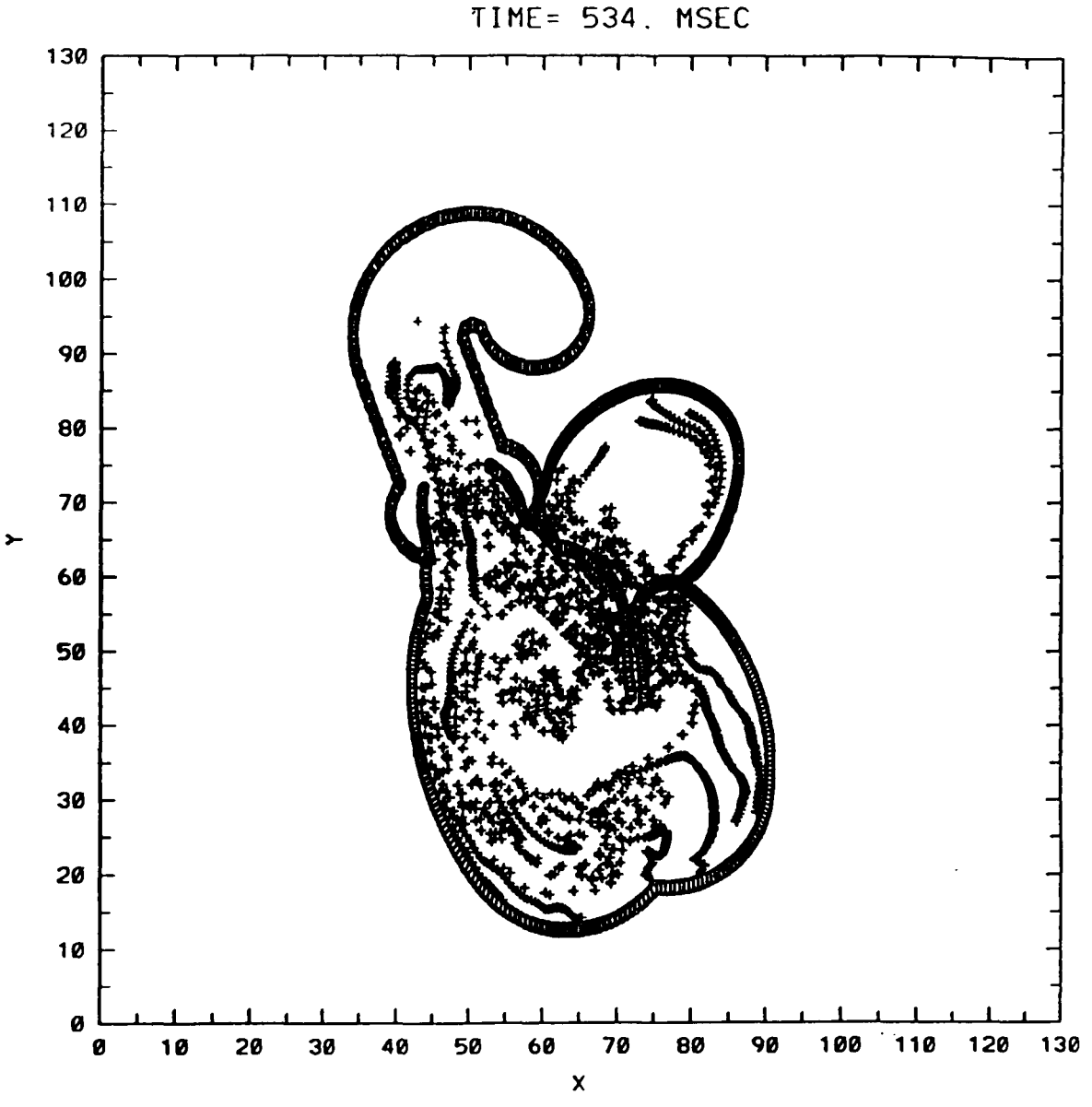

Figure 2.21D Heart Boundary and Fluid Markers 4.

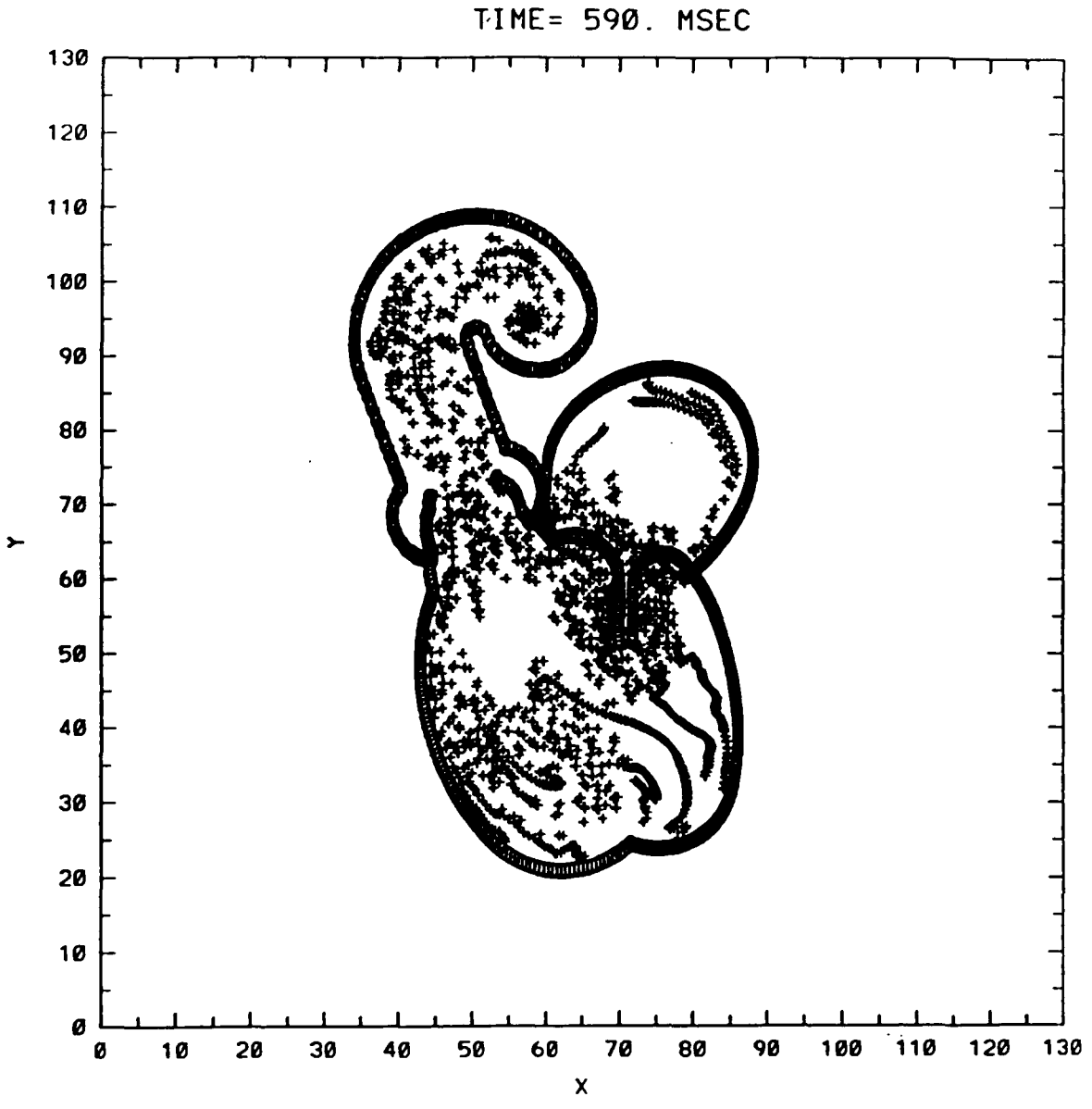

Figure 2.21E Heart Boundary and Fluid Markers 5.

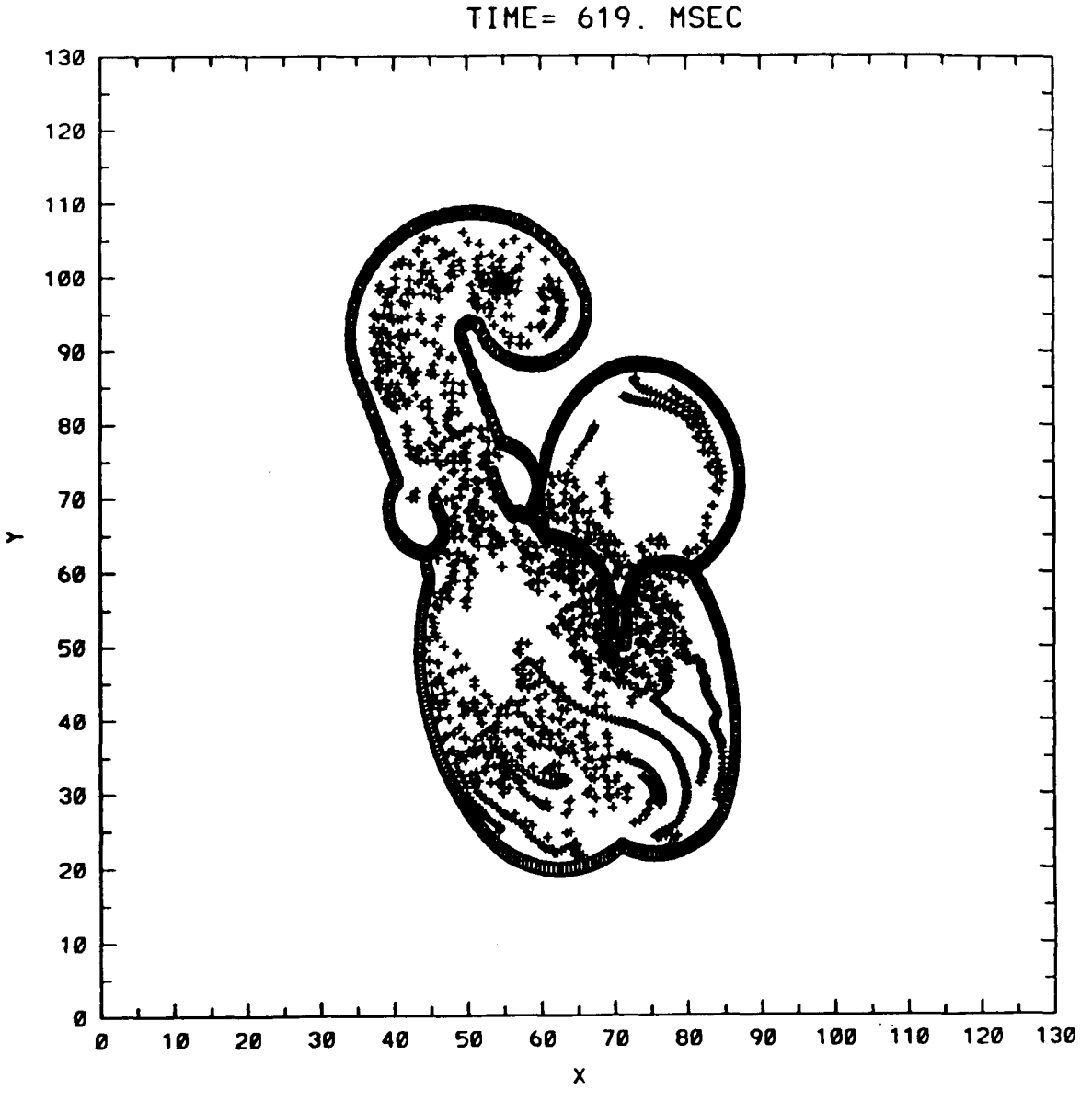

Figure 2.21F Heart Boundary and Fluid Markers 6.

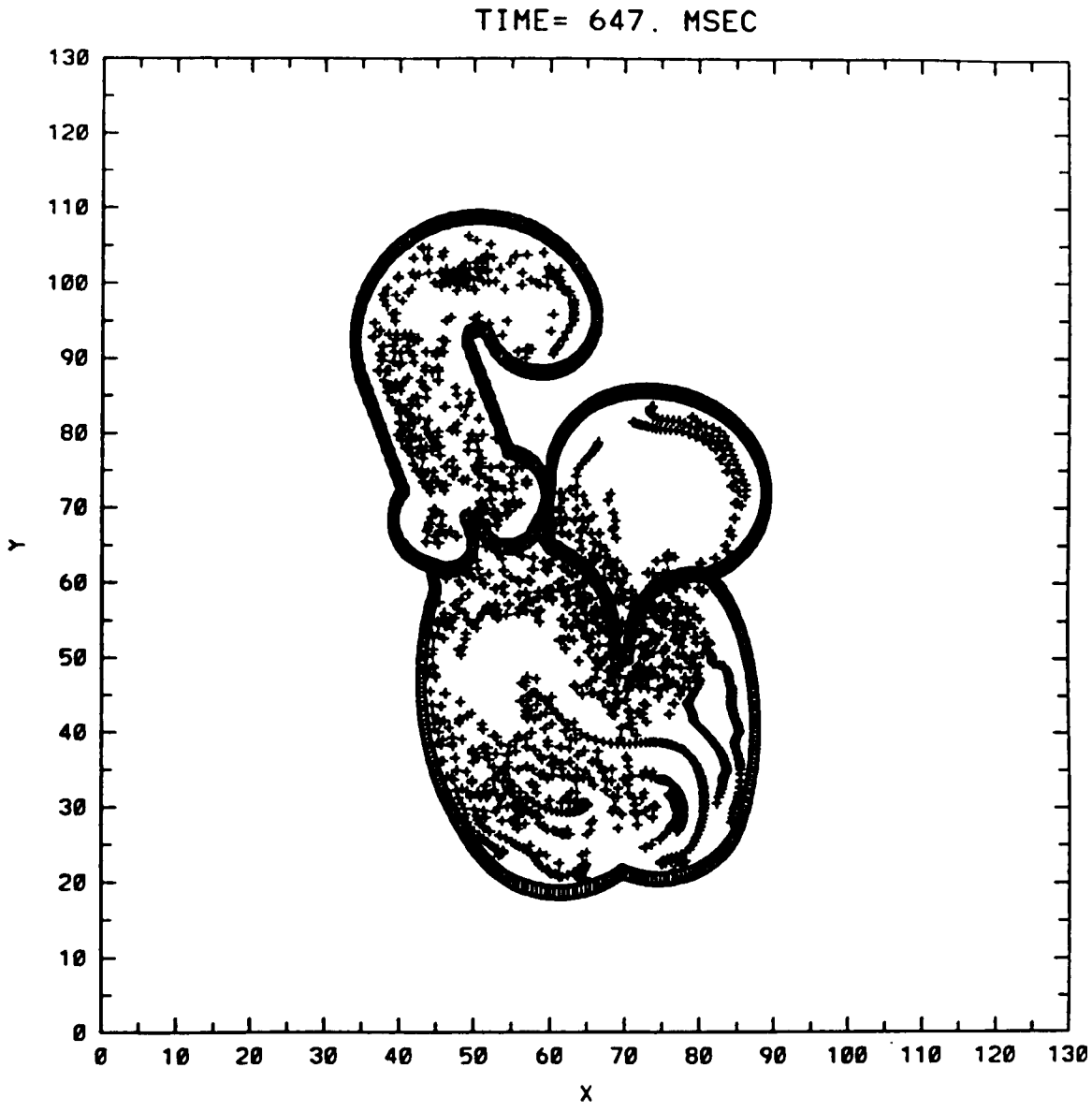

Figure 2.21G Heart Boundary and Fluid Markers 7.

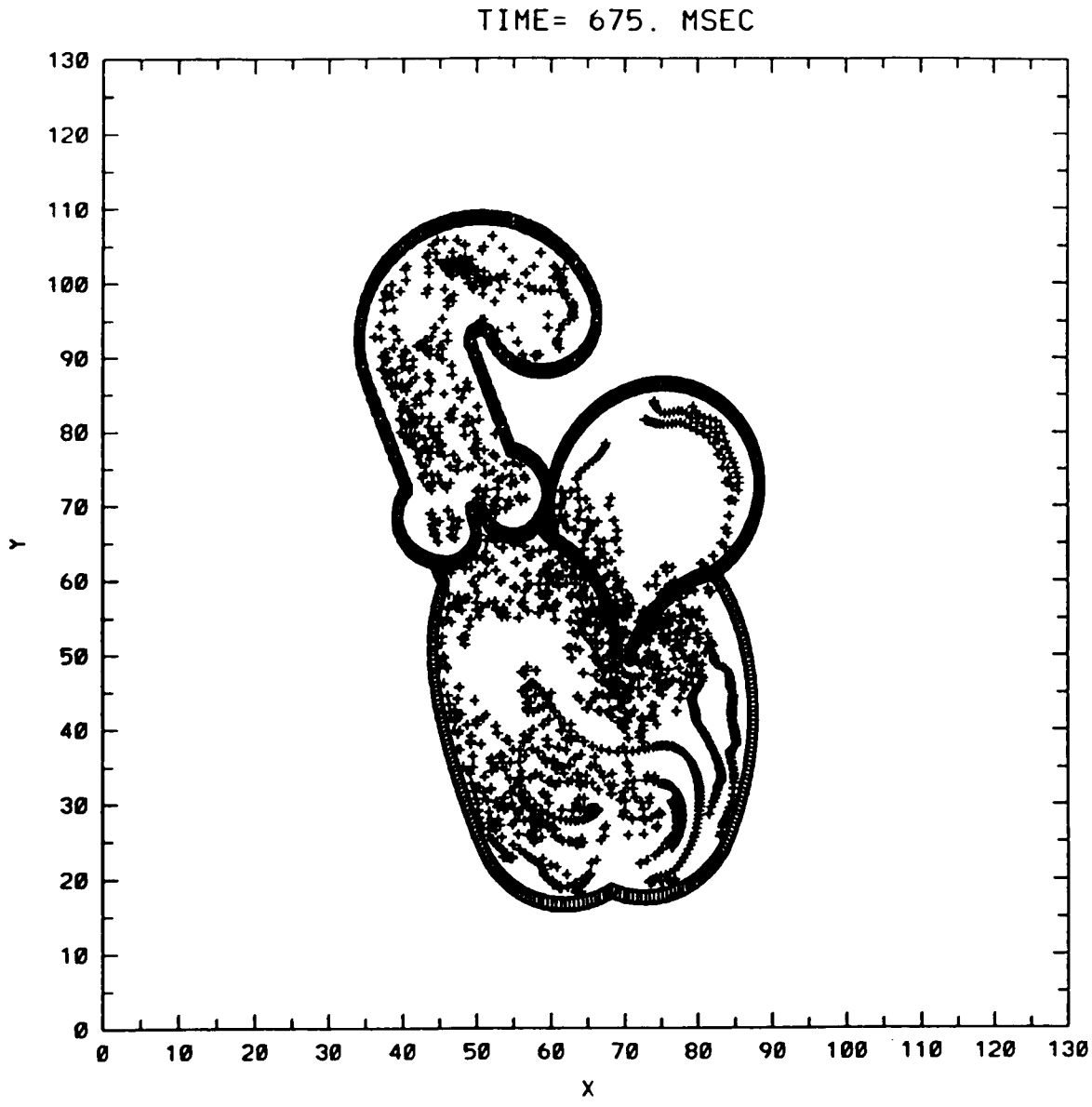

Figure 2.22 Mitral and Aortic Velocity (cm/sec) versus Time, Experiment II

Same as Figure 2.5, but with only the first heartbeat shown.

Solid curves in Figures 2.22 through 2.24 correspond to the results of Experiment II, while broken curves illustrate the identical data as was seen in Figures 2.5, 2.4, and 2.6, respectively.

Upper panels: flow velocity through the mitral valve (ring shown on left, cusp on right).

Lower panels: flow velocity through the aortic valve (ring on left, cusp on right).

Note that the magnitude of aortic velocity has been decreases versus Experiment I, while the mitral velocity has not changed.

Figure 2.22 Mitral and Aortic Velocity, Experiment II

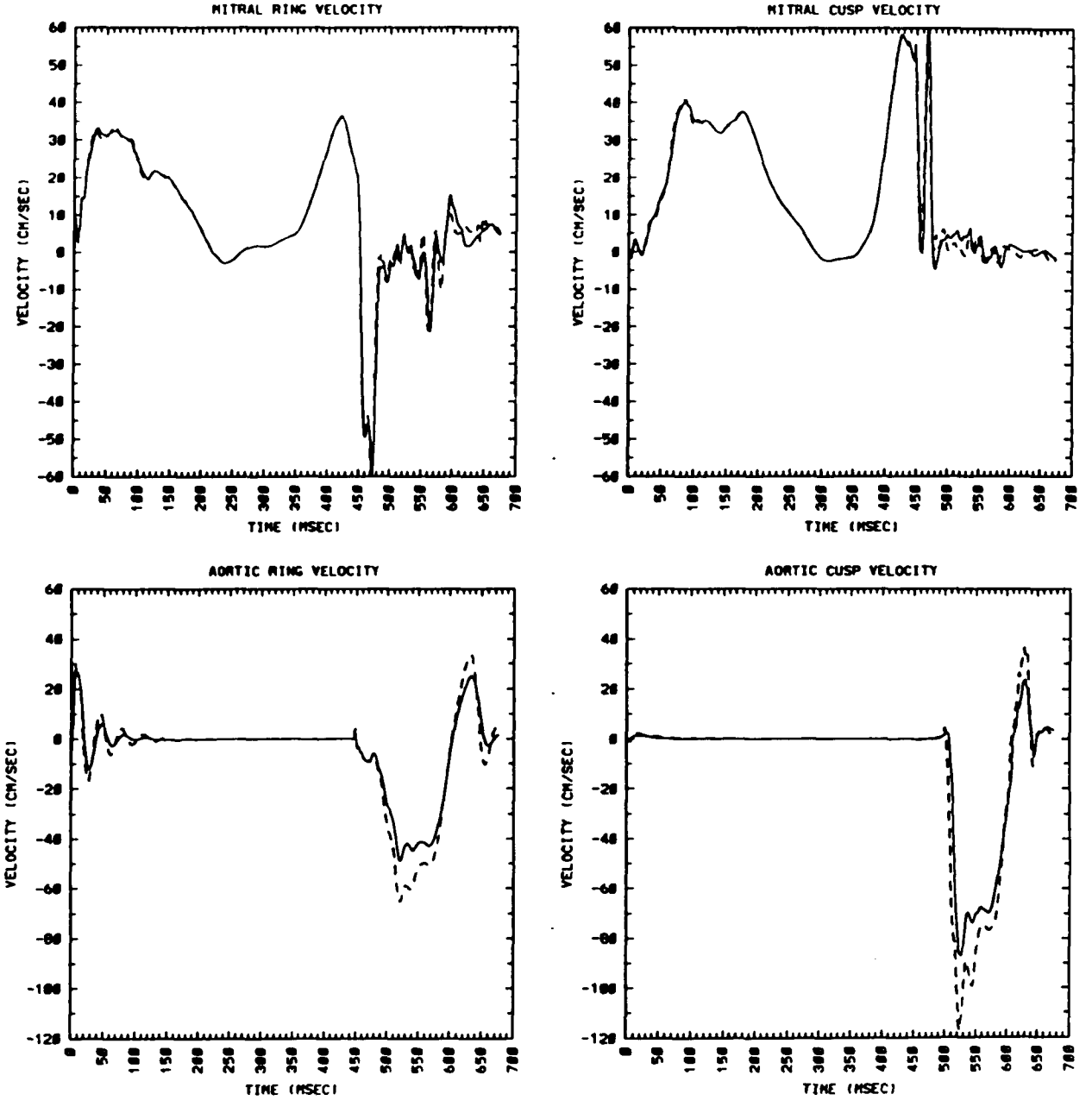

Figure 2.23 Atrial, Ventricular and Aortic Pressures vs Time, Experiment II

Again, the curve which is approximately constant (following initial damped oscillations) corresponds to aortic sink pressure *not* the pressure measured across the aortic valve. This pressure for Experiment II inceases to about 65 mm Hg during ventricular systole, versus Experiment I's peak pressure of about 55 mm Hg. Note that the atrial and ventricular volumes are the same for both experiments, leading to a decrease in the ventricular - aortic pressure gradient (although this has not been measured across the mitral valve ring). See text.

Figure 2.23 Atrial, Ventricular and Aortic Pressure, Experiment II

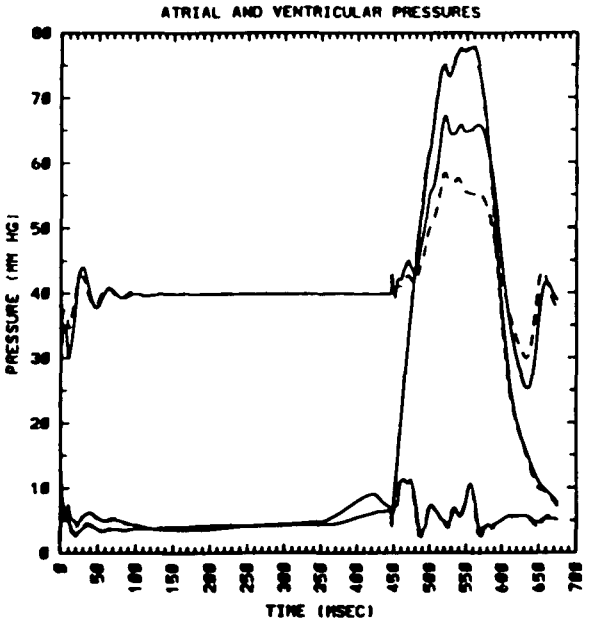

Figure 2.24 Atrial Inflow and Aortic Outflow vs Time, with cardiac chamber volumes.

Upper left panel represents the atrial inflow (top curve during diastole) and aortic source flow.

Systolic aortic sink outflow is less in Experiment II vs Experiment I.

Upper right panel represents the same data as in the upper left panel, but here integrated versus time to give total flow volume through the atrial source (top curve) and through the aortic sink (bottom curve). The difference between these two curves at the end of a heartbeat should be the change in total heart volume. Here, this difference is about 8 cc for Experiment I, while it has increased to 12 cc for Experiment II.

Lower left panel represents cardiac chamber volumes versus time.

Bottom curve: atrial volume

Second curve from bottom: aortic volume (note, this is constant throughout, as desired)

Second curve from top: ventricular volume

Top curve: total volume (sum off all three previous curves)

Ventricular volume and total volume are greater in Experiment II, as less blood was ejected through the aorta.

Figure 2.24 Source/Sink Flow and Chamber Volumes, Experiment II.

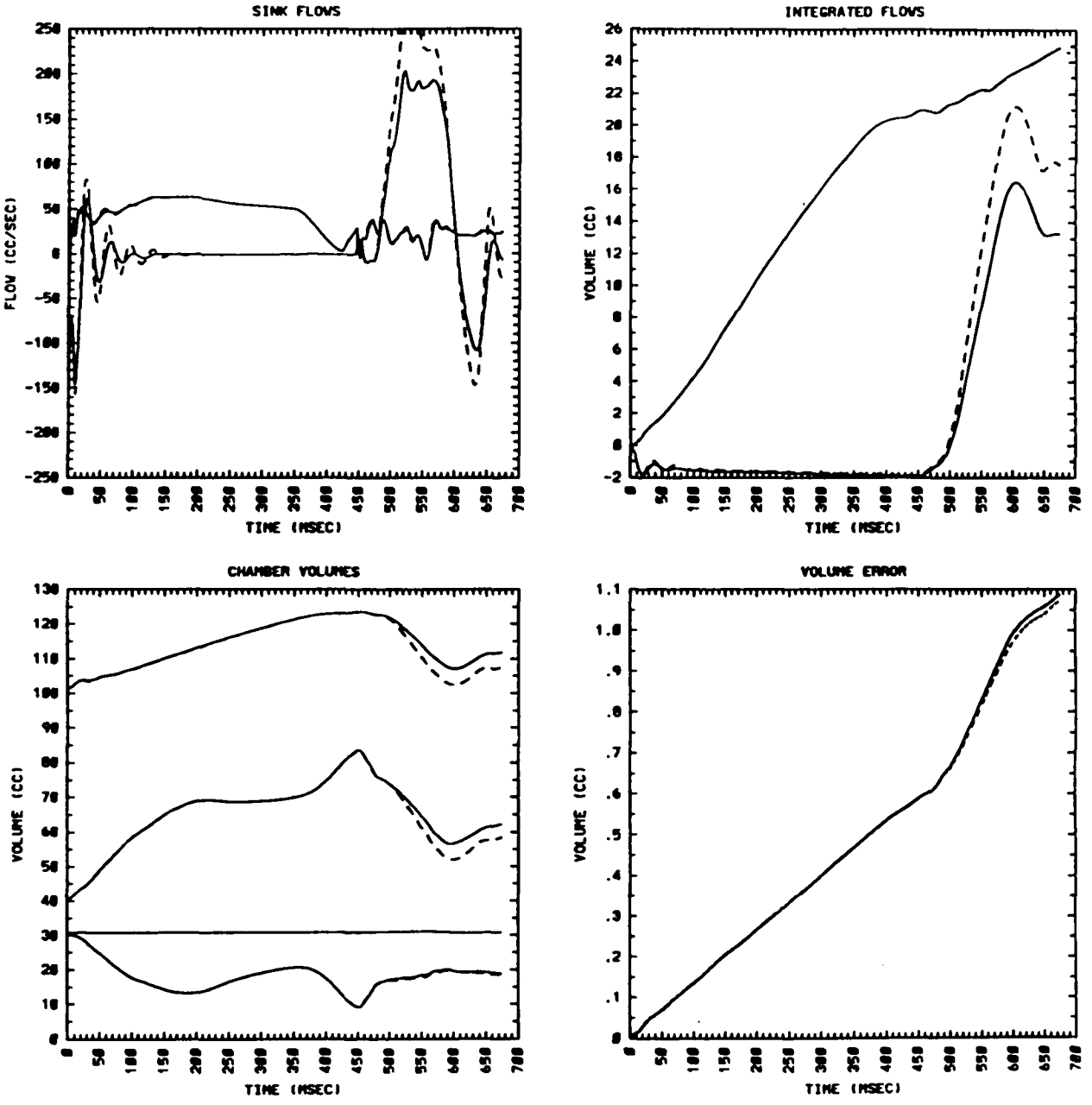

Figure 2.25 Plots of mitral flow and pressure, old model (corrected volume error method).

A Computed mitral annular flow (cc/sec). Note that mid-diastolic flow decreases gradually, and does not reach zero before atrial contraction. Compare with Figure 2.3A.

B Computed atrial, ventricular and aortic sink pressures, old model. The atrial and ventricular pressure curves do not cross during mid-diastole. Also, peak ventricular pressure is only about 40 mm Hg.

Figure 2.25 Mitral Flow and Chamber Pressure, Old Model

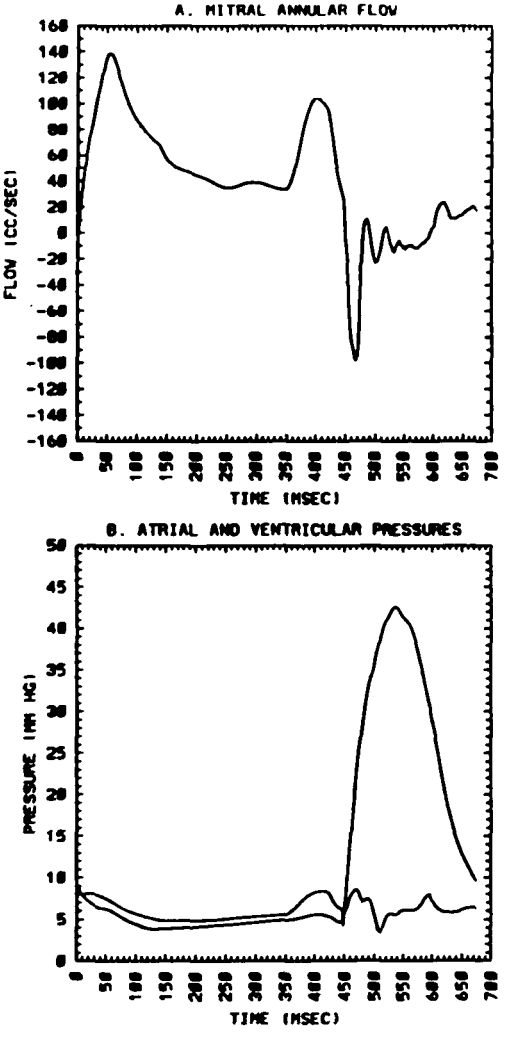

Figure 2.26 Oscillographic record from a normal conscious dog of high fidelity left atrial and ventricular pressures with a superimposed simultaneous pulsed-Doppler recording of transmitral flow. LVP, LAP: left ventricular, left atrial pressure; E, L, A: Peak rapid early filling velocity, mid-diastolic peak velocity, peak velocity during atrial contraction.

Courtesy of Dr. Edward Yellin.

Figure 2.26 Pulsed-Doppler Velocity and Pressure Measured in a Conscious Dog

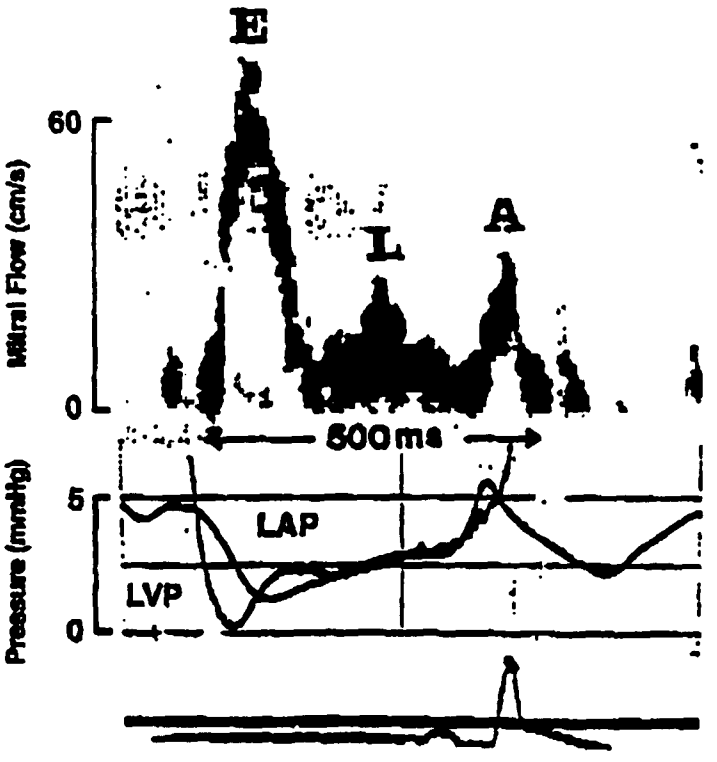

Chapter 3.

Implementation of a New Divergence Operator to Improve Volume Conservation in the Computer Heart Model[1]

Beth Feller Printz [2], and Charles S. Peskin, Ph.D.[3]

[1]This is a modification of Peskin C.S., Printz B.F. Improved volume conservation in the computation of flow with immersed elastic boundaries (In Press, Journal of Computational Physics) that includes the work primarily performed by the first author; the mathematical basis and formulation was devised by C.S. Peskin.

[2]Department of Physiology, Mount Sinai School of Medicine

[3]Courant Institute of Mathematical Sciences, New York University

Abstract

This paper describes the computational implementation of a new finite– difference divergence operator in the two dimensional model of blood flow through the heart. This divergence operator is based on the average, over a stencil surrounding each grid point, of the continuous divergence of the interpolated velocity field. Substituting this divergence operator in place of the centered-difference technique used previously results in a substantial improvement in the overall volume conservation, especially when left ventricular pressure increases during ventricular systole.

Introduction

This paper describes the computational implementation of a new finite-difference divergence operator in the two dimensional model of blood flow through the heart. This model is based on the immersed boundary technique developed by Peskin [1-5]. The motivation for this change was that the immersed boundary technique would occasionally seem to be "leaky": an increase in chamber pressure (here, the left ventricular pressure) resulted in a loss of volume at a rate proportional to the pressure difference across the wall. Because the previous applications of the immersed boundary technique were all at relatively low pressures, this effect was tolerable. However, when the ventricular pressures increased during systole, this volume loss was as much as one third of the total cardiac volume during a single heart beat, obviously too great to be ignored.

The most likely explanation that indeed the walls were allowing fluid to flow through was unfortunately not the case. This was proven by two experiments. First, when fluid markers were placed between the boundary points that determine the heart wall, they moved with the wall instead of being pushed out, as one might expect if the walls were actually leaking. Second, when the distance between wall points was decreased by doubling the number of points (without refining the computational grid), the leak did not change. A possible mathematic explanation is that although the discrete divergence of the velocity *on the computational grid* equals zero through Chorin's projection method, this does not imply that the *continuous* divergence of the interpolated velocity field (the velocity by which the boundary points actually move) is exactly zero. The implementation of a new finite-difference divergence operator, constructed in such a way that the interpolated velocity field in which the immersed boundary moves is more nearly divergence free, virtually eliminates this volume error without substantially increasing computational time.

Methods

A summary of the immersed boundary technique in general appears in Chapter 1.3 and [3,4,5]. As a description of the mathematical formulation of this new divergence procedure is not the intent of this paper, this discussion will be limited to the procedure's salient features. For the complete mathematical description please see APPENDIX, which reprinted from the methodology section of [1]. In the prior formulation of the mathematical model of blood flow in the heart, a simple centered-difference divergence method was used in the final steps of Chorin's projection method to solve for the new velocity. These two steps, shown in Chapter 1.3 Equations 1.11 and 1.12, are the only places where the divergence enters into the calculations. A centered difference divergence can be expressed as:

$$D\mathbf{u} = 1/2h((\mathbf{u}_{i+1,j} - \mathbf{u}_{i-1,j}) + (\mathbf{u}_{i,j+1} - \mathbf{u}_{i,j-1})) \tag{1}$$

where $D\mathbf{u}$ is the discrete divergence, h is the grid spacing (here, 1/64 or 1/128), and $\mathbf{u}_{i,j}$ is the velocity on the gridpoint (i,j). This centered-difference formula is written as $\mathbf{D} = (D_x^0, D_y^0)$

This formula produces a zero divergence on the computational grid through Chorin's method. However, the boundary particles that represent the heart walls and valves are moved under an interpolated field. This interpolated velocity field is computed by using the grid velocities weighted by a discrete delta function, as described in APPENDIX. The interpolated velocity field is defined everywhere by

$$\mathbf{U}(\mathbf{X}) = \sum_{\mathbf{x}} \mathbf{u}(\mathbf{x})\delta_h(\mathbf{x} - \mathbf{X})h^2 \tag{2}$$

The new divergence operator $\mathbf{D}$ is then constructed in such a way that

$$(\mathbf{D} \cdot \mathbf{u})(\mathbf{x}) = h^{-2} \int_{B(\mathbf{x})} (\nabla \cdot \mathbf{U})(\mathbf{X})\, d\mathbf{X} \tag{3}$$

where $B(\mathbf{x})$ is a square box of side h alligned parallel to the grid and centered on the grid point $\mathbf{x}$. In other words, $\mathbf{D} \cdot \mathbf{u}$ at the grid point $\mathbf{x}$ is defined as the average value of $\nabla \cdot \mathbf{U}$ over the box $B(\mathbf{x})$ centered on $\mathbf{x}$. For the actual evaluation of the operator $\mathbf{D}$, Equation [3] can be rewitten using the divergence theorem:

$$(\mathbf{D}\cdot\mathbf{u})(\mathbf{x}) = h^{-2}\int_{-h/2}^{h/2} U_x(x+X,\, y+Y)\,dY\Big|_{X=-h/2}^{X=h/2} + h^{-2}\int_{-h/2}^{h/2} U_y(x+X\ ,\, y+Y)\,dX\Big|_{Y=-h/2}^{Y=h/2} \tag{4}$$

where we use the notation $\mathbf{x} = (x,y)$, $\mathbf{X} = (X,Y)$, $\mathbf{U} = (U_x, U_y)$.

By substituting the particular form for the delta function, this new form for the divergence, $\mathbf{D}$, can be calculated. The substitution of this divergence method entails changing the coefficients of the Fourier-transformed Poisson equation that is used to solve $-\mathbf{D} \cdot \mathbf{D}p = q$, during the last two steps of Chorin's method, as described in APPENDIX. These coefficients are actually an array based on a 5 X 5 grid stencil centered on the boundary point in question; the stencil size is a function of the particular delta function employed. This coefficient array is computed during preprocessing, and therefore does not increase computational time. However, the actual application of the new divergence operator $\mathbf{D}$ to the grid takes slightly more time due to the increased stencil size.

Results

The two different forms of the divergence operator, *old* based on a simple centered-difference approach, and *new* based on the finite-difference technique briefly described above, were compared by using each in the two- dimensional model of blood flow through the heart. The modular nature of this program is such that implementation of one or the other can be accomplished without changing any other parameters.

The heart model is shown in Figure 3.1. It includes a left atrium, left ventricle, mitral valve, and crude aortic valve, as described below. The details of this model were described previously (Chapter 1.3). The only change is that now in addition to the atrial source that models the pulmonary venous return there is an aortic sink located in the ventricular outflow tract that models the ejection function of the aortic valve. Thus, the results presented are for the complete heart beat (diastole plus systole), not only for diastole through early systole as was possible before the addition of this aortic sink. A complete description of this aortic sink addition (together with that of a true aortic valve) are found in Chapter 3. There is still a third source/sink located outside the heart to accommodate the instantaneous volume changes that occur during the cardiac cycle, since volume is constant with incompressible fluid.

The old and new divergence methods are compared in Figures 3.2-3.5. Figures 3.2 and 3.3 are the results of a computational heart beat where all sources and sinks have been turned off in order to enable a straightforward calculation of volume conservation: the sum of the chamber volumes should be equal throughout the heart beat. Figures 3.4 and 3.5 show the results if the sources and sinks are turned back on, as they would be for a beating heart. Volume conservation can still be checked, however, as the sum of all flow through the sources and sinks should equal the change in total volume (atrium plus ventricle).

Figures 3.2 and 3.4 compare the old and new methods in terms of the computed waveforms of flow, pressure, and volume. Of note, there is an additional pressure trace seen in the lower left panel of Figure 3.4 which is the pressure in the ventricular outflow tract. This trace has a flat top during ventricular systole because it is clamped near the aortic pressure while the aortic valve is open. Data from the computational simulation using the new divergence formula are shown as solid curves, while the experiment using the old divergence formula are shown as broken curves. Selected streamline plots generated during the same computations can be seen in Figures 3.3 and 3.5. In each figure, the top row corresponds to the old method, while the bottom was generated by the new method.

In Figures 3.2 and 3.4, the upper right panel contains graphs of the atrial volume (lowest curve), the ventricular volume (middle curve), and the combined atrial plus ventricular volume (upper curve) as functions of time. For the experimental run without sources or sinks seen in Figure 3.2, if there was no loss of volume the upper curve should be a straight line, (since combined volume would be constant). This is virtually true for the new method (solid curve). The old method, however, shows a large volume loss particularly once ventricular pressure begins to rise during systole ($T > 450msec$). Looking at the expanded-scale volume error plotted in Figure 3.2 (bottom right), the volume error of the new method barely can be distinguished from zero.

Another demonstration of the volume loss can be seen by looking at the actual heart boundary and streamline plots, displayed in Figure 3.3. As one looks from left to right (as time advances through the cardiac cycle), the heart decreases in size in the upper panels (old method) but retains its size in the lower panels (new method).

When one examines the data from the experimental run where sources and sinks have been turned back on, one should now consider the volume error as the *difference* between

the sum of all flow though the sources and sinks, and the total chamber volume. These results are shown in Figure 3.4. If this difference were zero (no leak), flow into and out of the heart would be exactly balanced by a change in heart volume. Again, the volume error for the new method is just barely distinguishable from zero, even on the expanded scale. Figure 3.5 shows the corresponding streamlines for these two experiments comparing the old and new methods with source and sink on. The volume loss in the old method (top row) is less evident here, as ventricular volume is decreasing in both cases because of normal ejection through the aortic valve. However, about a third of the ventricular volume (8 cc) is lost in the old method through the numerical leakiness rather than being ejected through the aorta. The heart can be seen to rotate once ventricular systole begins; there is also a small amount of translation, which has not been shown. The reason for movement is that unlike the real heart which is tethered to some extent by the surrounding connective tissue and other structures, the model heart is free to float inside its computational domain. The greater heart rotation seen in the new method may be a consequence of the greater systolic ejection.

Since the volume errors of the new method are too small to be read off easily from Figures 3.2 and 3.4, the volume errors at the end of each of the computational experiments are listed in Table 3.1. The improvement achieved through the use of the new method can be measured by the ratio of the old volume error to the new volume error. For the two experiments reported here (with and without sources/sinks), these improvement factors are 67 and 225.

One should note that the left-hand panels in Figures 3.2 and 3.4 illustrate that other physiological variables are not very sensitive to the changes in the divergence method that has been described above (and hence they are not very sensitive to the volume error of

the old method). The agreement between the old and new results is particularly good in the left-hand panels of Figure 3.4, perhaps because the sources and sinks tend to regulate the ventricular volume independent of the numerical leakiness of the old method. This relative insensitivity is an important finding, since it serves to validate the results previously reported in spite of this volume error.

Summary and Conclusions

This paper describes the implementation of a finite-difference divergence operator based on the interpolation scheme used for the two dimensional modeling of blood flow through the heart. The construction is such that the discrete divergence at a mesh point is the same as the average over a 5 by 5 stencil surrounding that mesh point of the continuous divergence of the interpolated velocity field.

The substitution of this divergence operator in place of the simple centered- difference approach used previously involves changes only in the projection step of the fluid dynamics subroutine (Chorin's Method). This substitution yields a substantial improvement in volume conservation by reducing volume errors by up to a factor of 225. This improvement is especially important when high pressure differences between chambers are generated, as occurs during ventricular systole.

Appendix

This Methods section is reprinted from [1], Peskin CS, Printz BF. *Improved volume conservation in the computation of flows with immersed elastic boundaries.* In Press, J Comput Physics.

Summary of the immersed-boundary method

Consider a closed elastic curve immersed in a two-dimensional incompressible fluid. The equations of motion of the system may be written as follows:

$$\rho(\frac{\partial \mathbf{u}}{\partial t} + \mathbf{u}\cdot\nabla\mathbf{u}) + \nabla p = \mu\nabla^2\mathbf{u} + \mathbf{F} \tag{1}$$

$$\nabla\cdot\mathbf{u} = 0 \tag{2}$$

$$\mathbf{F}(\mathbf{x},t) = \int_0^L \mathbf{f}(s,t)\,\delta(\mathbf{x}-\mathbf{X}(s,t))\,ds \tag{3}$$

$$\frac{\partial \mathbf{X}}{\partial t}(s,t) = \mathbf{u}(\mathbf{X}(s,t),t) = \int \mathbf{u}(\mathbf{x},t)\,\delta(\mathbf{x}-\mathbf{X}(s,t))\,d\mathbf{x} \tag{4}$$

$$\mathbf{f}(s,t) = \frac{\partial}{\partial s}(T\tau) \tag{5}$$

$$T = S(|\frac{\partial \mathbf{X}}{\partial s}| - 1) \tag{6}$$

$$\tau = \frac{\partial \mathbf{X}/\partial s}{|\partial \mathbf{X}/\partial s|} \tag{7}$$

Here $\mathbf{u}(\mathbf{x},t)$ is the fluid velocity, $p(\mathbf{x},t)$ is the fluid pressure, and $\mathbf{F}(\mathbf{x},t)$ is the force-density generated by the boundary in the fluid. ($\mathbf{F}(\mathbf{x},t)$ is a δ-function layer, see Eq. (2)). The constants ρ and μ are the fluid density and viscosity. The boundary configuration is given by $\mathbf{x} = \mathbf{X}(s,t)$, $0 \le s \le L$, where fixed s marks a material point and L is the unstressed length of the boundary. Since the boundary is a closed curve, $\mathbf{X}(0,t) = \mathbf{X}(L,t)$. The force exerted by the element of boundary ds on the fluid is $\mathbf{f}(s,t)\,ds$. This force is computed from the boundary tension $T(s,t)$ and the unit tangent $\tau(s,t)$, see Eq. (5).

Since the formation given above is somewhat unusual, it is important to remark that it can be reduced to a standard formulation in terms of boundary conditions which hold on the immersed elastic interface. The only technical assumption we need in order to make this reduction is that the fluid velocity is continuous across the interface. (Without this assumption Eq. 4 becomes ambiguous.) Then Eq. (4) is equivalent to the no-slip condition that the fluid sticks to the boundary. Note that this condition here plays the role of an equation of motion for the boundary rather than that of a constraint on the fluid motion, since the boundary motion is not specified in advance. The remaining boundary condition concerns the jump in stress across the immersed boundary. To find it, combine Eqs. (1) and (3) and write the result as follows

$$\rho\frac{Du_i}{Dt} = \frac{\partial\sigma_{ij}}{\partial x_j} + \int_0^L f_i(s)\,\delta(\mathbf{x} - \mathbf{X}(s,t))\,ds \tag{8}$$

where

$$\frac{D}{Dt} = \frac{\partial}{\partial t} + \mathbf{u}\cdot\nabla \tag{9}$$

is the material derivative and where

$$\sigma_{ij} = -p\delta_{ij} + \mu\left(\frac{\partial u_i}{\partial x_j} + \frac{\partial u_j}{\partial x_i}\right) \tag{10}$$

is the fluid stress tensor. In the foregoing we have used the summation convention that a repeated index is summed from 1 to 2. Now integrate Eq. (8) over an arbitrary region $\Omega(t)$ that moves with the fluid. Let the boundary of Ω be denoted $\partial\Omega$, let $\mathbf{n}$ be the outward normal on $\partial\Omega$, and let $d\ell$ be the arc length on $\partial\Omega$. The result is

$$\frac{d}{dt}\int_{\Omega(t)} \rho\, u_i\, d\mathbf{x} = \int_{\partial\Omega(t)} \sigma_{ij} n_j\, d\ell + \int_{\{s:\,\mathbf{X}(s,t)\in\Omega(t)\}} f_i(s,t)\, ds \tag{11}$$

Finally, let $\Omega(t)$ collapse to a thin strip of finite length with the immersed boundary running

down its center. Take the limit as the width of the strip approaches zero. Then

$$0 = \int ([\sigma_{ij} n_j]\, d\ell + f_i\, ds) \tag{12}$$

where n is now the normal on one side of the immersed boundary and where [ ] denotes the jump in a quantity across the immersed boundary. Since the domain of integration is arbitrary

$$[\sigma_{ij}] n_j = -f_i \frac{ds}{d\ell} = -\frac{f_i}{|\partial \mathbf{X}/\partial s|} \tag{13}$$

Taking normal and tangential components, we get

$$n_i [\sigma_{ij}] n_j = -\frac{\mathbf{f} \cdot \mathbf{n}}{|\partial \mathbf{X}/\partial s|} \tag{14}$$

$$\tau_i [\sigma_{ij}] n_j = -\frac{\mathbf{f} \cdot \boldsymbol{\tau}}{|\partial \mathbf{X}/\partial s|} \tag{15}$$

where $\boldsymbol{\tau} = (\partial \mathbf{X}/\partial s)\,/\,|\partial \mathbf{X}/\partial s|$ is the unit tangent to the immersed boundary. Now

$$n_i [\sigma_{ij}] n_j = -[p] \tag{16}$$

and

$$\tau_i [\sigma_{ij}] n_j = \mu \boldsymbol{\tau} \cdot [\mathbf{n} \cdot \nabla \mathbf{u}] = \mu \boldsymbol{\tau} \cdot [\frac{\partial \mathbf{u}}{\partial n}] \tag{17}$$

where $\partial/\partial n$ denotes the normal derivative. We leave the proofs of Eqs. (16–17) as exercises for the reader with the following hints: To prove (16) make use of the identity $n_i n_j + \tau_i \tau_j = \delta_{ij}$, the fact that $\nabla \cdot \mathbf{u} = 0$, and the fact that $[\tau_i \frac{\partial u_j}{\partial x_i}] = [(\boldsymbol{\tau} \cdot \nabla \mathbf{u})_j] = 0$ since $[\mathbf{u}] = 0$ and since $\boldsymbol{\tau} \cdot \nabla$ is the *tangential* derivative. To prove (17), use the last of these facts and also $\boldsymbol{\tau} \cdot \mathbf{n} = 0$.

It follows from Eqs. (14-17) that

$$[p] = \frac{\mathbf{f} \cdot \mathbf{n}}{|\partial \mathbf{X}/\partial s|} \tag{18}$$

$$\mu \boldsymbol{\tau} \cdot [\frac{\partial \mathbf{u}}{\partial n}] = -\frac{\mathbf{f} \cdot \boldsymbol{\tau}}{|\partial \mathbf{X}/\partial s|} \tag{19}$$

which are the expected conditions for force balance at a massless interface along which the force $\mathbf{f}\,ds$ is applied to the interval ds of the boundary. (The factor $|\partial \mathbf{X}/\partial s|$ appears because s is not arc length in general.)

We have derived Eqs. (18–19) only to show that our formulation of the problem in terms of a delta-function layer of force reduces to well-known boundary conditions for the jump in stress at an interface. The strength of our formulation, however, is that it makes no explicit use of these jump conditions, which would be awkward to discretize along a moving boundary, the motion of which is unknown.

The discretization and numerical solution of Eqs. (1–7) proceeds as follows [1-5]. Let each independent variable be restricted to a lattice of equally spaced points: $\mathbf{x} = (jh, kh)$, $s = \ell\,\Delta s$, $t = n\,\Delta t$, where j, k, ℓ, n are integers and where $h = \Delta x = \Delta y$. In particular we shall use notations such as $\sum_{\mathbf{x}}$ and $\sum_s$ to denote sum over these computational lattices. Let D^+, D^-, D^0 denote the forward, backward, and centered divided difference operators. A subscript on such an operator indicates the variable to which it should be applied. Let the time step index n be written as a superscript, so that $\mathbf{u}^n(\mathbf{x}) = \mathbf{u}(\mathbf{x}, n\,\Delta t)$. The goal of the method is to compute $(\mathbf{u}^{n+1}, \mathbf{X}^{n+1})$ from $(\mathbf{u}^n, \mathbf{X}^n)$. This is done as follows.

1) Find the boundary force $\mathbf{f}^n$ from the boundary configuration $\mathbf{X}^n$:

$$T^n = S(|D_s^+ \mathbf{X}^n| - 1) \tag{20}$$

$$\tau^n = \frac{D_s^+ \mathbf{X}^n}{|D_s^+ \mathbf{X}^n|} \tag{21}$$

$$\mathbf{f}^n = D_s^-(T^n \tau^n) \tag{22}$$

Remark. This is an *explicit* method for the computation of the boundary force. For more stable alternatives, see [1-5,14].

2) Apply the force $\mathbf{f}^n$ to the grid of the fluid computation:

$$\mathbf{F}^n(\mathbf{x}) = \sum_s \mathbf{f}^n(s)\,\delta_h(\mathbf{x} - \mathbf{X}^n(s))\,\Delta s \tag{23}$$

where, for $\mathbf{x} = (x, y)$,

$$\delta_h(\mathbf{x}) = \delta_h(x)\,\delta_h(y) \tag{24}$$

and

$$\delta_h(x) = \begin{cases} \frac{1}{4h}(1 + \cos\frac{\pi x}{2h}) & |x| \le 2h \\ \\ 0 & |x| \ge 2h \end{cases} \tag{25}$$

3) Update the fluid velocity under the influence of the force density $\mathbf{F}^n$. This is done by Chorin's projection method [15,16] which solves the following systems successively for $\mathbf{u}^{n+1,0}$, $\mathbf{u}^{n+1,1}$, $\mathbf{u}^{n+1,2}$, $(\mathbf{u}^{n+1}, p^{n+1})$:

$$\rho\frac{\mathbf{u}^{n+1,0} - \mathbf{u}^n}{\Delta t} = \mathbf{F}^n \tag{26}$$

$$\rho\left(\frac{\mathbf{u}^{n+1,1} - \mathbf{u}^{n+1,0}}{\Delta t} + u_x^n D_x^0 \mathbf{u}^{n+1,1}\right) = \mu D_x^+ D_x^- \mathbf{u}^{n+1,1} \tag{27}$$

$$\rho\left(\frac{\mathbf{u}^{n+1,2} - \mathbf{u}^{n+1,1}}{\Delta t} + u_y^n D_y^0 \mathbf{u}^{n+1,2}\right) = \mu D_y^+ D_y^- \mathbf{u}^{n+1,2} \tag{28}$$

$$\begin{cases} \rho\left(\frac{\mathbf{u}^{n+1} - \mathbf{u}^{n+1,2}}{\Delta t}\right) + \mathbf{D}p^{n+1} = 0 \\ \\ \mathbf{D}\cdot\mathbf{u}^{n+1} = 0 \end{cases} \tag{29}$$

(The proper choice of $\mathbf{D}$ is the subject of this paper; see below.)

4) Interpolate the new velocity to the old boundary positions and move the boundary points:

$$\mathbf{X}^{n+1}(s) = \mathbf{X}^n(s) + \Delta t \sum_{\mathbf{x}} \mathbf{u}^{n+1}(\mathbf{x})\,\delta_h(\mathbf{x} - \mathbf{X}^n(s))\,h^2 \tag{30}$$

where δ_h is the approximate δ-function defined above, see Eqs. (24)-(25).

This completes the time step.

The vector difference operator $\mathbf{D}$ corresponding to the vector derivative operator ∇ has been left unspecified in the foregoing. In all previous work we used $\mathbf{D} = (D_x^0, D_y^0)$. An improved recipe for $\mathbf{D}$ is introduced in the next section.

Construction of a divergence operator based on the interpolation scheme

The velocity field in which the boundary points actually move is not the discrete velocity field $\mathbf{u}(\mathbf{x})$, which is defined only at grid points, but the interpolated velocity field $\mathbf{U}(\mathbf{X})$, which is defined everywhere by the formula

$$\mathbf{U}(\mathbf{X}) = \sum_{\mathbf{x}} \mathbf{u}(\mathbf{x})\, \delta_h(\mathbf{x} - \mathbf{X})\, h^2 \tag{31}$$

Because of the properties of δ_h (see Eqs. (24)-(25)), $\mathbf{U}(\mathbf{X})$ is continuous and has continuous first derivatives. Thus $\nabla \cdot \mathbf{U}$ is well-defined, and we can construct the operator $\mathbf{D}$ in such a way that

$$(\mathbf{D} \cdot \mathbf{u})(\mathbf{x}) = h^{-2} \int_{B(\mathbf{x})} (\nabla \cdot \mathbf{U})(\mathbf{X})\, d\mathbf{X} \tag{32}$$

where $B(\mathbf{x})$ is a square box of side h alligned parallel to the grid and centered on the grid point $\mathbf{x}$. In other words, $\mathbf{D} \cdot \mathbf{u}$ at the grid point $\mathbf{x}$ is defined as the average value of $\nabla \cdot \mathbf{U}$ over the box $B(\mathbf{x})$ centered on $\mathbf{x}$. For the actual evaluation of the operator $\mathbf{D}$, we rewrite Eq. (32) with the aid of the divergence theorem

$$\begin{aligned} (\mathbf{D} \cdot \mathbf{u})(\mathbf{x}) \;=\; & h^{-2} \int_{-h/2}^{h/2} U_x(x + X, y + Y)\, dY \Big|_{X=-h/2}^{X=h/2} \\ & + h^{-2} \int_{-h/2}^{h/2} U_y(x + X, y + Y)\, dX \Big|_{Y=-h/2}^{Y=h/2} \end{aligned} \tag{33}$$

where we use the notation $\mathbf{x} = (x, y)$, $\mathbf{X} = (X, Y)$, $\mathbf{U} = (U_x, U_y)$. Substituting into this equation the expression for $\mathbf{U}$ from Eq. (31) and making use of the fact that δ_h is even, we

find

$$\begin{aligned}(\mathbf{D}\cdot\mathbf{u}) &= \sum_{\mathbf{x}'} u_x(x',y')\delta_h(X+x-x')\Big|_{X=-h/2}^{X=h/2}\int_{-h/2}^{h/2}\delta_h(Y+y-y')dY \\ &\quad + \sum_{\mathbf{x}'} u_y(x',y')\int_{-h/2}^{h/2}\delta_h(X+x-x')dX\,\delta_h(Y+y-y')\Big|_{Y=-h/2}^{Y=h/2} \\ &= \sum_{\mathbf{x}'}[u_x(x',y')\gamma(x-x')\omega(y-y') + u_y(x',y')\omega(x-x')\gamma(y-y')]\end{aligned} \tag{34}$$

where we have introduced the notation

$$\gamma(x) = \delta_h(x+X)\Big|_{X=-h/2}^{X=h/2} \tag{35}$$

$$\omega(x) = \int_{-h/2}^{h/2}\delta_h(x+X)\,dX \tag{36}$$

(We shall only make use of the values of γ and ω on the lattice points $x = jh$.) Note that

$$\sum_x \gamma(x) = \delta_h(\infty) - \delta_h(-\infty) = 0 \tag{37}$$

$$\sum_x \omega(x) = \int_{-\infty}^{\infty}\delta_h(x)\,dx = 1\ . \tag{38}$$

Thus the values of γ are like coefficients of a difference operator and the values of ω are like coefficients of an averaging operator.

From Eq. (34) we may read off the form of the vector difference operator **D**. Its components D_x and D_y are given by

$$(D_x\phi)(x,y) = \sum_{x'y'}\phi(x',y')\,\gamma(x-x')\omega(y-y') \tag{39}$$

$$(D_y\phi)(x,y) = \sum_{x'y'}\phi(x',y')\,\omega(x-x')\gamma(y-y') \tag{40}$$

These equations (together with the definnitions of γ and ω, Eqs. (35)-(36)) give a definite recipe for the construction of D in terms of any choice that one might happen to make of the function δ_h. In our particular case, the values of γ and ω are found as follows.

Since δ_h is even, γ is odd and ω is even. Also, since $\delta_h(x) = 0$ for $|x| \geq 2h$, $\gamma(x) = \omega(x) = 0$ for $|x| \geq 5h/2$. We have

$$\gamma(0) = \delta_h(\frac{h}{2}) - \delta_h(-\frac{h}{2}) = 0 \tag{41}$$

$$-\gamma(-h) = \gamma(h) = \delta_h(\frac{3h}{2}) - \delta_h(\frac{h}{2}) = -\frac{1}{2h}\frac{\sqrt{2}}{2} \tag{42}$$

$$-\gamma(-2h) = \gamma(2h) = \delta_h(\frac{5h}{2}) - \delta_h(\frac{3h}{2}) = -\frac{1}{4h}(1 - \frac{\sqrt{2}}{2}) \tag{43}$$

$$\gamma(jh) = 0 \quad \text{for } |j| \geq 3 \tag{44}$$

$$\omega(0) = \int_{-h/2}^{h/2} \delta_h(x)\,dx = \frac{1}{4} + \frac{\sqrt{2}}{2\pi} \tag{45}$$

$$\omega(-h) = \omega(h) = \int_{h/2}^{3h/2} \delta_h(x)\,dx = \frac{1}{4} \tag{46}$$

$$\omega(-2h) = \omega(2h) = \int_{3h/2}^{2h} \delta_h(x)\,dx = \frac{1}{8} - \frac{\sqrt{2}}{4\pi} \tag{47}$$

$$\omega(jh) = 0 \quad \text{for } |j| \geq 3 \tag{48}$$

This completes the construction of the vector difference operator $\mathbf{D} = (D_x, D_y)$. The value of $\mathbf{D} \cdot \mathbf{u}$ at a particular grid point $\mathbf{x}$ is a function of the values of $\mathbf{u}$ on a 5×5 stencil of the grid centered on $\mathbf{x}$.

Implementation of the projection operation

Chorin's projection method gets its name from the system of Eqs. (17), which we rewrite here in the form

$$\begin{aligned} \rho\frac{\mathbf{u} - \mathbf{w}}{\Delta t} + \mathbf{D}p &= 0 \\ \mathbf{D} \cdot \mathbf{u} &= 0 \end{aligned} \tag{49}$$

These equations define the orthogonal projection of $\mathbf{w}$ onto the space of vector fields that are divergence-free in the sense that $\mathbf{D} \cdot \mathbf{u} = 0$. This is the only place that the operator $\mathbf{D}$ appears in the computational method.

Given $\mathbf{w}$, the system of Eqs. (49) can be solved for the unknowns $(\mathbf{u}, p)$ in the following way. First evaluate

$$\mathbf{q} = -\frac{\rho}{\Delta t}\mathbf{D} \cdot \mathbf{w} \tag{50}$$

Next, solve a discrete Poisson equation for p:

$$-\mathbf{D} \cdot \mathbf{D}p = q \tag{51}$$

Finally, evaluate $\mathbf{u}$ as follows:

$$\mathbf{u} = \mathbf{w} - \frac{\Delta t}{\rho}\mathbf{D}p \tag{52}$$

It is easy to check that this procedure constructs a solution to Eqs. (49). First note that Eq. (52) is just a rewritten version of the first equation in the system of Eqs. (49). Then, to show that $\mathbf{D} \cdot \mathbf{u} = 0$, apply $\mathbf{D}\cdot$ to both sides of Eq. (52) and make use of Eqs. (50)-(51).

We now consider the solution of the discrete Poisson equation $-\mathbf{D} \cdot \mathbf{D}p = q$. This will be done by the discrete Fourier transform.

Up to now we have not made any statement about the domain occupied by the fluid in which our elastic boundary is immersed. Suppose this domain is a square periodic box covered by an $N \times N$ grid. We define the discrete Fourier transform of a grid function $p_{jk} = p(jh, kh)$ by the formula

$$\hat{p}_{\ell m} = \sum_{jk} p_{jk}\, e^{-i\frac{2\pi}{N}(j\ell + km)} \tag{53}$$

The inversion formula is

$$p_{jk} = \frac{1}{N^2}\sum_{\ell m} \hat{p}_{\ell m}\, e^{i\frac{2\pi}{N}(j\ell + km)} \tag{54}$$

and the discrete convolution theorem reads as follows:

$$\sum_{j'k'} p_{j'k'} q_{j-j',k-k'} = \frac{1}{N^2} \sum_{\ell m} \hat{p}_{\ell m} \hat{q}_{\ell m} \, e^{i\frac{2\pi}{N}(j\ell+km)} \tag{55}$$

Applying this convolution theorem to the definition of **D**, Eqs. (39)-(40), we see that

$$(D_x \phi)^{\wedge}_{\ell m} = \hat{\gamma}_\ell \hat{\omega}_m \hat{\phi}_{\ell m} \tag{56}$$

$$(D_y \phi)^{\wedge}_{\ell m} = \hat{\omega}_\ell \hat{\gamma}_m \hat{\phi}_{\ell m} \tag{57}$$

These results may be summarized by the statement that

$$\hat{\mathbf{D}}_{\ell m} = (\hat{\gamma}_\ell \hat{\omega}_m \, , \, \hat{\omega}_\ell \hat{\gamma}_m) \tag{58}$$

which defines the Fourier transform of the vector difference operator **D**. The Fourier transform of the discrete Poisson equation $-\mathbf{D} \cdot \mathbf{D}p = q$ therefore reads as follows:

$$-(\hat{\gamma}_\ell^2 \hat{\omega}_m^2 + \hat{\omega}_\ell^2 \hat{\gamma}_m^2) \, \hat{p}_{\ell m} = \hat{q}_{\ell m} \tag{59}$$

and, of course, the solution of this equation for $\hat{p}$ is

$$\hat{p}_{\ell m} = \frac{\hat{q}_{\ell m}}{-(\hat{\gamma}_\ell^2 \hat{\omega}_m^2 + \hat{\omega}_\ell^2 \hat{\gamma}_m^2)} \tag{60}$$

It remains only to evaluate $\hat{\gamma}$ and $\hat{\omega}$ (and to be careful of those cases in which the denominator in Eq. (60) is zero!).

The values of γ and ω are listed in Eqs. (41–48). From these we conclude that

$$\begin{aligned} \hat{\gamma}_\ell &= \frac{\sqrt{2}}{2} \frac{1}{2h} 2i \sin \frac{2\pi\ell}{N} + (1 - \frac{\sqrt{2}}{2}) \frac{1}{4h} 2i \sin \frac{4\pi\ell}{N} \\ &= \frac{i}{h} (\sin \frac{2\pi\ell}{N}) (\frac{\sqrt{2}}{2} + (1 - \frac{\sqrt{2}}{2}) \cos \frac{2\pi\ell}{N}) \end{aligned} \tag{61}$$

$$\begin{aligned}
\hat{\omega}_\ell &= (\frac{1}{4} + \frac{\sqrt{2}}{2\pi}) + \frac{1}{4} 2\cos\frac{2\pi\ell}{N} + (\frac{1}{8} - \frac{\sqrt{2}}{4\pi}) 2\cos\frac{4\pi\ell}{N} \\
&= (\frac{1}{4} + \frac{\sqrt{2}}{2\pi}) + \frac{1}{2}(1 - 2\sin^2\frac{\pi\ell}{N}) + (\frac{1}{4} - \frac{\sqrt{2}}{2\pi})(1 - 2\sin^2\frac{2\pi\ell}{N}) \\
&= 1 - \sin^2\frac{\pi\ell}{N} - (\frac{1}{2} - \frac{\sqrt{2}}{\pi}) 4\sin^2\frac{\pi\ell}{N}\cos^2\frac{\pi\ell}{N} \\
&= (\cos^2\frac{\pi\ell}{N})(1 - 2(1 - \frac{2\sqrt{2}}{\pi})\sin^2\frac{\pi\ell}{N})
\end{aligned} \tag{62}$$

Note that $\hat{\gamma}_\ell = 0$ if and only if $\sin(2\pi\ell/N) = 0$. The other factor in $\hat{\gamma}_\ell$ cannot be zero, since $1 - \sqrt{2}/2 < \sqrt{2}/2$. Similarly, $\hat{\omega}_\ell = 0$ if and only if $\cos^2\frac{\pi\ell}{N} = 0$. The other factor in $\hat{\omega}_\ell$ cannot be zero, since $2(1 - 2\sqrt{2}/\pi) < 1$. Thus $\hat{\gamma}_\ell = 0$ where $\ell = 0$, $N/2$ and $\hat{\omega}_\ell = 0$ when $\ell = N/2$. These are the only zeros of $\hat{\gamma}$ and $\hat{\omega}$ on the interval $[0 \cdots (N-1)]$.

We now consider the denominator of Eq. (60), which may be written in the form $(-\hat{\gamma}_\ell^2)\hat{\omega}_m^2 + \hat{\omega}_\ell^2(-\hat{\gamma}_m^2)$. Since $\hat{\gamma}$ is imaginary and $\hat{\omega}$ is real, both terms in this expression are real and nonnegative. The expression as a whole can only be zero if both of its terms are zero. This will happen if $\ell = N/2$, if $m = N/2$, or if $(\ell, m) = (0,0)$. There are no other cases. (We consider only those possibilities in which ℓ and m are integers in the interval $[0 \cdots (N-1)]$.)

The values of (ℓ, m) for which the denominator in Eq. (60) is zero are precisely the values of (ℓ, m) for which $\hat{\mathbf{D}}_{\ell m} = (0,0)$. Since q is computed by applying $\mathbf{D}\cdot$ to some vector, the numerator in Eq. (60) is also zero at these wave numbers. Thus $\hat{p}_{\ell m}$ is undefined in these cases. Its value is of no consquence, however, since $\hat{\mathbf{D}}\hat{p}_{\ell m}$ is zero for these special wave numbers. In practice, we set $\hat{p}_{\ell m} = 0$ for $(\ell, m) = (0,0)$, for $\ell = N/2$ (with any m), and for $m = N/2$ (with any ℓ).

In the practical implementation of this method, we make use of an array $\hat{a}_{\ell m}$, which is

computed and stored during preprocessing, and which is defined as follows:

$$\hat{a}_{\ell m} = \begin{cases} 0\,, & (\ell,m) = (0,0),\ \ell = N/2, \text{ or } m = N/2 \\ \\ \dfrac{1}{(-\hat{\gamma}_\ell^2)(\hat{\omega}_m^2) + \hat{\omega}_\ell^2(-\hat{\gamma}_m^2)}\,, & \text{otherwise} \end{cases} \tag{63}$$

Then, when it is time to compute $\hat{p}$ from $\hat{q}$, we simply use

$$\hat{p}_{\ell m} = \hat{a}_{\ell m}\, \hat{q}_{\ell m} \tag{64}$$

for all (ℓ, m) including the special values noted above.

The overall algorithm for the solution of the discrete Poisson equation $-\mathbf{D}\cdot\mathbf{D}p = q$ may now be summarized as follows

$$p = (FFT)^{-1}(\hat{a} \quad (FFT)(q)) \tag{65}$$

where (FFT) denotes the Fast Fourier Transform algorithm and where $(FFT)^{-1}$ stands for the version of that algorithm that applies the inverse Fourier transform. Because the array $\hat{a}$ is computed during preprocessing, the computational effort involved in the solution of the discrete Poisson equation is identical to what it was in our earlier work in which D was simply (D_x^0, D_y^0). The only change is that the array $\hat{a}$ now holds different numbers than before. Somewhat more work is required, however, in the steps that immediately precede and follow the solution of the discrete Poisson equation. These are the steps in which the operator D is directly applied to data, see Eqs. (50) and (52), and the additional work is a consequence of the larger stencil of D.

Discussion of an alternative approach to improved volume conservation

Since we use a Fourier method to solve the projection equations (Eqs. 49), the following alternative approach to improved volume conservation may occur to the reader: why not

use a finite Fourier series to represent **w**, perform a *continuous* projection of **w** to obtain a *divergence-free* Fourier series for **u**, and then *evaluate* this series at points of the immersed boundary in order to define the velocity with which the boundary moves? The practical difficulty with this approach involves the last step: evaluating the Fourier series at the points of the immersed boundary. Since these points do not lie on a regular grid, the Fast Fourier Transform is not suitable for the purpose. Since the number of boundary points is $O(N)$ and the number of nonzero Fourier coefficients would be $O(N^2)$, the computational work required to evaluate the boundary velocity in this alternative manner would be $O(N^3)$. This alternative is therefore expensive and has not, in fact, been tried.

References

[1] Peskin CS, Printz BF. Improved volume conservation in the computation of flows with immersed elastic boundaries. In Press, J Comput Phys.

[2] Peskin CS. Flow patterns around heart valves: a numerical method. J Comput Phys 10:252-271, 1972.

[3] Peskin CS. Numerical analysis of blood flow in the heart. J Comput Phys 25:220-252, 1977.

[4] McQueen DM, Peskin CS, Yellin EL. Fluid dynamics of the mitral valve: physiological aspects of a mathematical model. Am J Physiol 242 (Heart Circ Physiol 11):H1095-1110, 1982.

[5] Meisner JS, McQueen DM, Ishida Y, Vetter HO, et. al. Effects of timing of atrial systole on LV filling and mitral valve closure: computer and dog studies. Am J Physiol 249 (Heart Circ Physiol 18):H604-619, 1985.

[6] Peskin CS, McQueen DM. Modeling prosthetic heart valves for numerical analysis of blood flow in the heart. J Comput Phys 37:113-132, 1980.

[7] McQueen DM, Peskin CS. Computer-assisted design of pivoting disc prosthetic mital valves. J Thorac Cardiovasc Surg 86:126-135, 1983.

[8] Peskin CS, McQueen DM. A three-dimensional computational method for blood flow in the heart: I. Immersed elastic fibers in a viscous incompressible fluid. J Comput Phys 81:373-405, 1989.

[9] McQueen DM, Peskin CS. A three-dimensional computational method for blood flow in the heart: II. Contractile Fibers. J Comput Phys 82:289-297, 1989.

[10] Tu C, Peskin CS. Stability and instability in the computation of flows with immersed elastic boundaries. J Sci Stat Comput. In Press.

[11] Chorin AJ. Numerical method for solving incompressible viscous flow problems. J Comput Physics 2:12-26, 1967.

[12] Chorin AJ. Numerical solution of the Navier-Stokes equations for an incompressible fluid. Math Comp 23:928-931, 1969.

Table 3.1 Volume Errors Over One Cardiac Cycle

Sources & Sinks	OLD METHOD	NEW METHOD	OLD/NEW
OFF	8.81 cm^3	0.132 cm^3	67
ON	11.58 cm^3	0.0508 cm^3	225

Figure 3.1 The Peskin–McQueen Computer Heart Model

(A). View of the base of the heart, comprised of the valve rings, with a line drawn to indicate the two-dimensional cross section that is represented in the model. This plane bisects the anterior leaflet (AL) and posterior leaflet (PL) of the mitral valve, together with the aortic root, left atrium, and left ventricle.

(B). An illustration of the computational plane as indicated in (A), showing the portions of the atrium, ventricle, and aortic root represented in the model.

(C). The initial configuration of the computational heart model, superimposed on the 64 X 64 computational grid. The initial heart geometry is constructed by the parameters R_{LV}, the left ventricular radium; ZV, the length of the straight segment of the ventricle; ZA, the left of the ventricular outflow tract; ZE, the length of the straight segment of the atrium (which functions to increase the size of the atrium); R_{LA}, the radius of the left atrium; and PHM, the angle of the mitral valve ring with respect to the horizontal axis. The lines across the ventricle represent cross links used simulate the forces generated in the plane perpendicular to the model plane. These links generate force at their end points only, and do not interfere with the flow inside the heart. There is also a source in the middle of the left ventricle which models pulmonary venous return to the heart, a sink equipped with a mathematical pop-off valve which models aortic outflow, and a source/sink around the edges of the domain to accomodate instantaneous changes in volume.

(D). Representation of Hill's three component muscle model, which is incorporated into the links between boundary points used to represent the cardiac muscular characteristics. Each link is comprised of a parallel elastic element (PE), a series elastic element (SE) and a contractile element (CE). The elastic elements are linear springs,

while the contractile element generates force dependent on its velocity of shortening; see [3] for details.

(Figure from [3], reprinted with permission of author and publisher).

Figure 3.1 The Peskin–McQueen Computer Heart Model

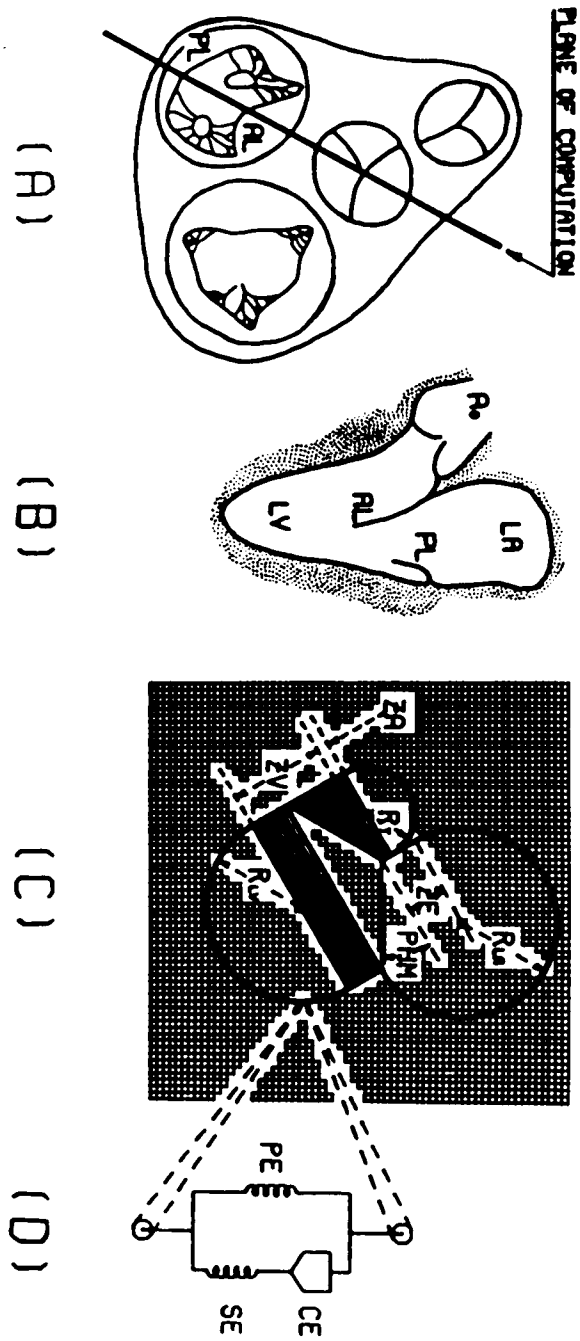

Figure 3.2 Flow, pressure and volume during one cardiac cycle plotted versus time. The sources and sinks have been turned off during this experiment in order to more easily study the volume error. Solid curves represent the results computed using the new divergence method, broken curves represent the computed results using the old divergence method. The upper left panel plots the flow (volume/time) through the mitral valve annulus, the upper right panel plots the volumes of the left atrium (lower curves), the left ventricle (middle curves), and the sum of atrial and ventricular volumes (upper curves). The lower left panel plots the chamber pressures throughout the cardiac cyle: the atrial and ventricular pressure are not greatly different until ventricular systole, when the ventricular pressure rises. The lower right panel contains the same data as shown in the top curves of the upper right panel, but now plotted on an expanded scale to better visualize the volume loss. If there were no volume loss, the upper curve of the upper left panel would be constant since there is no source or sink. However, the broken curve departs substantially from a straight line, especially after ventricular pressure begins to rise with the onset of ventricular systole at about 450 msec. The total volume obtained by using the new form of the divergence is essentially flat. Even on the expanded scale seen in the lower right plot, the volume error is essentially zero.

Figure 3.2 Flow, Pressure and Chamber Volume, No Source/Sink

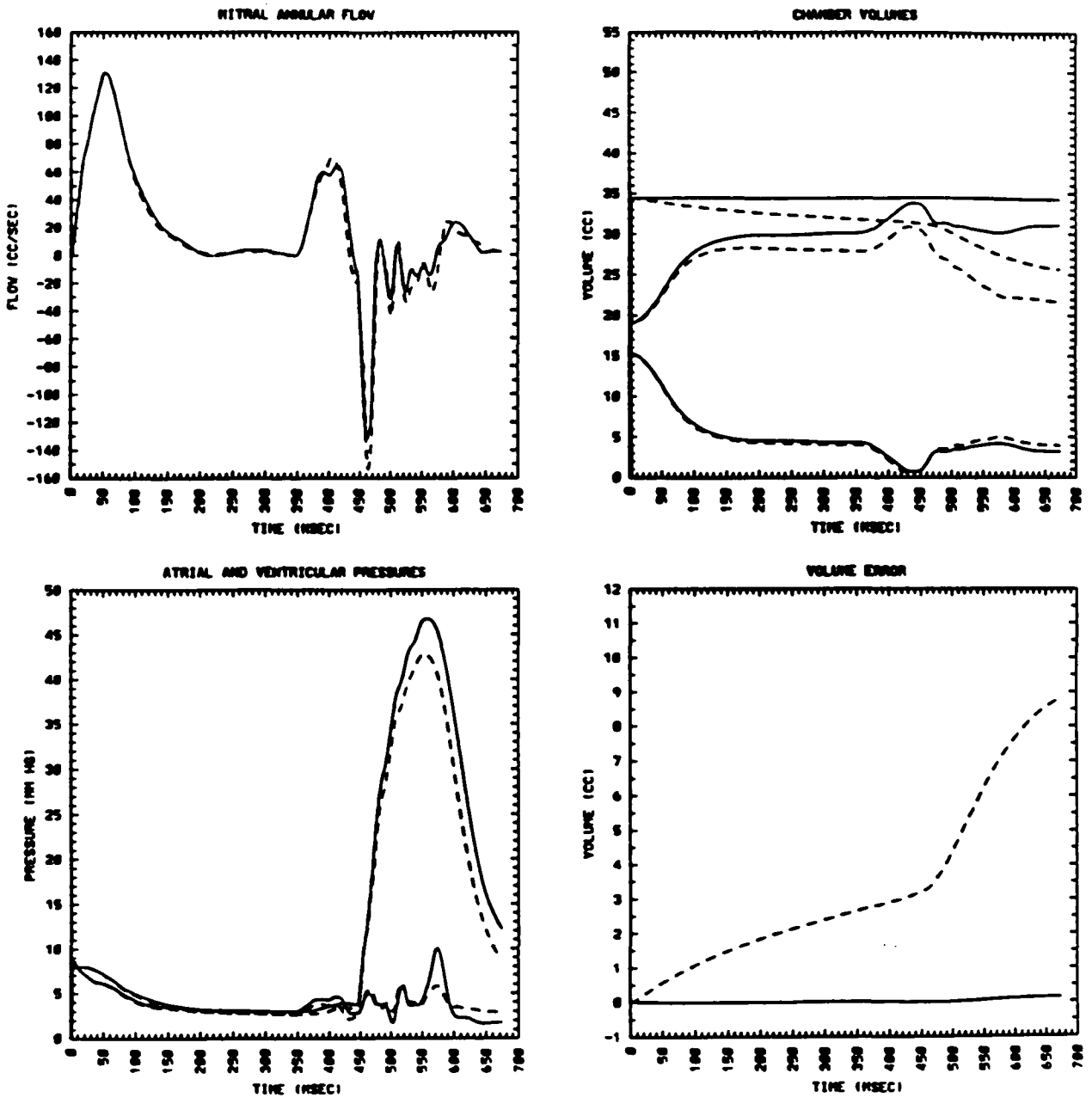

Figure 3.3 Computed heart boundary configuration and streamlines corresponding to the waveforms shown in Figure 3.2.

Again, all sources and sinks have been turned off. The top row are the results of the old method, and the bottom row the results of the new method. Each subsequent frame in a row depicts the heart configuration at a particular timestep, separated by about 113 msec from the following frame (or 160 timesteps). Thus, the first frame in each row corresponds to a time at the beginning of diastole, while the last frame in each row is at the end of ventricular systole. Note that the heart volume is larger in the last frame of the new method (bottom row, far right) compared with the last frame of the old method (top row, far right). The extra streamlines seen in the last two frames of the old method (top row) may be associated with the previous numerical leakiness.

Figure 3.3 Computed Heart Boundaries and Streamlines, No Source/Sink

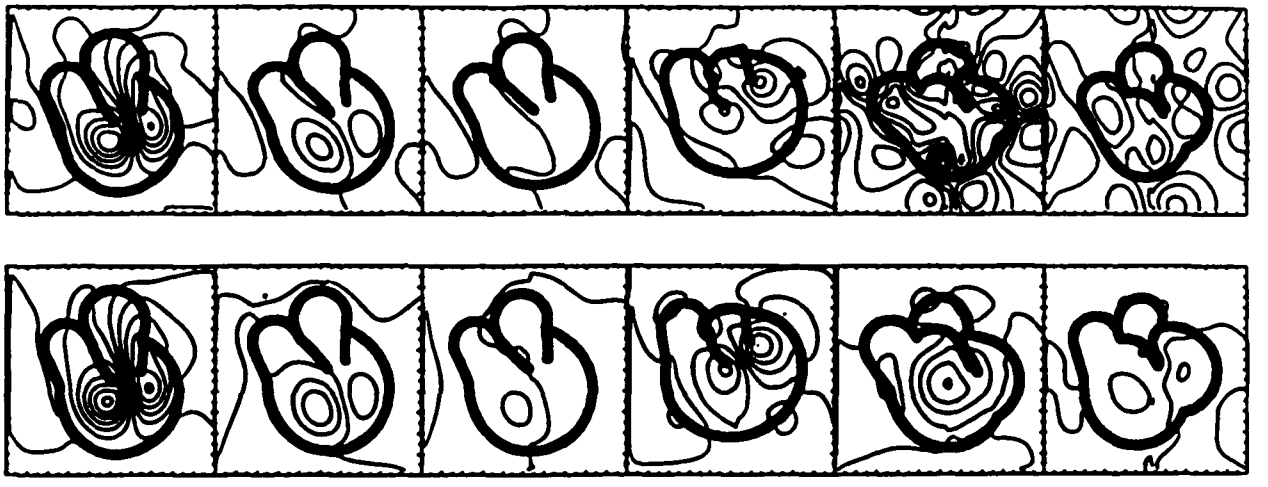

Figure 3.4 Flow, pressure and volume during one cardiac cycle plotted versus time with sources and sinks turned on.

As in Figure 3.2, the solid curves represent data generated with the computer model using the new divergence technique while the broken curves represent data generated with the computer model using the old divergence technique. There is an extra set of curves seen in the lower left panel pressure plots that represents the pressure in the ventricular outflow tract where the aortic sink has been placed. This pressure is approximately clamped by the aortic pressure when the aortic "valve" opens once ventricular pressure exceeds a certain number (here, set at 35 mm Hg). The total volume seen in the upper right panel is no longer constant, since the heart gains volume through the pulmonary venous source into the atrium and loses volume out of the aortic "valve" during systole. As explained in the text, a volume error can still be constructed by comparing the integrated change in volume over the complete heart beat with the amount of fluid known to have entered and left the heart through the atrial source and aortic sink. This difference is seen in the lower left panel.

Figure 3.4 Flow, Pressure and Chamber Volume, Source and Sink ON

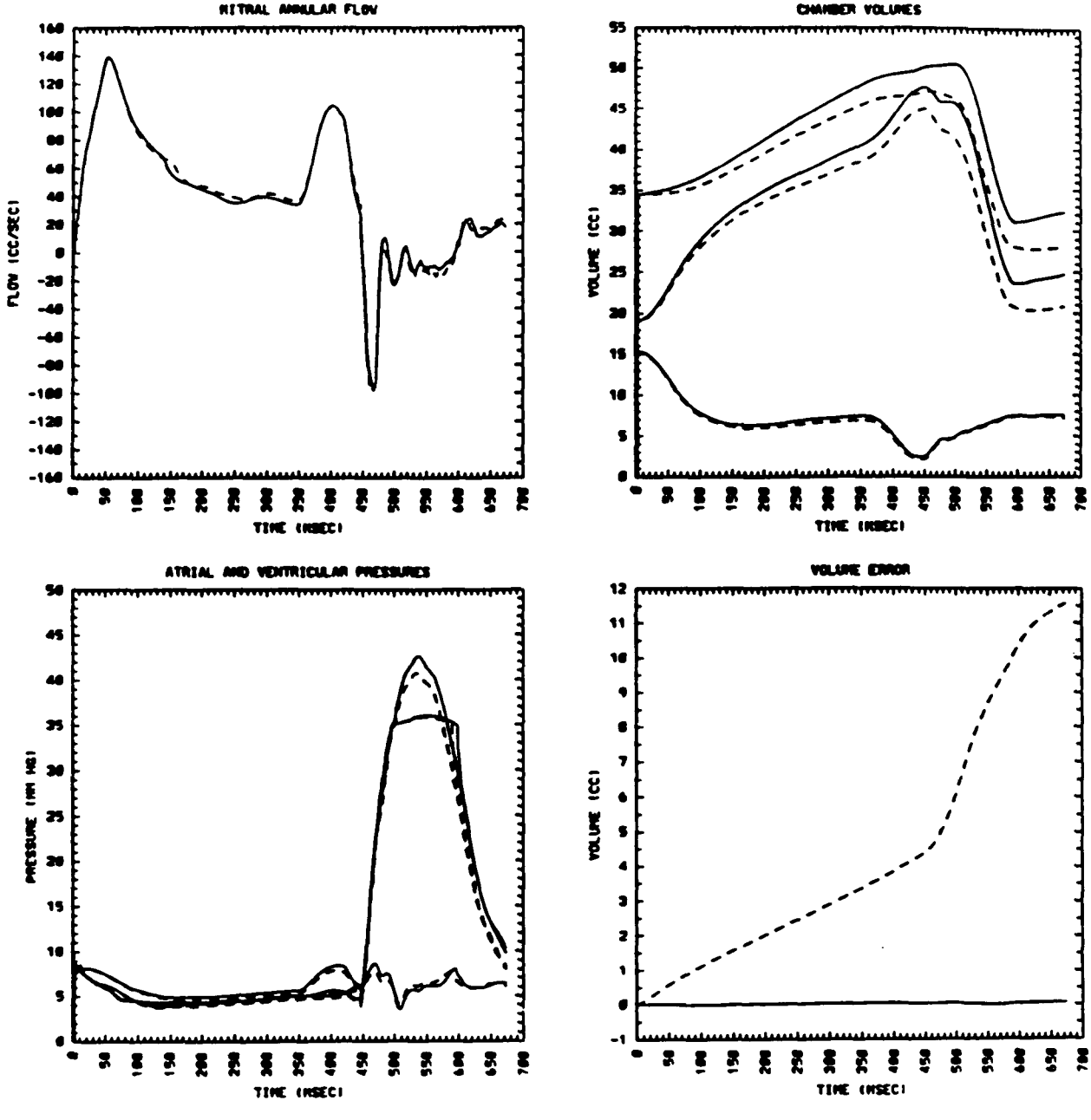

Figure 3.5 Computed heart boundary and streamlines corresponding to the waveforms of Figure 3.4.

Format same as in Figure 3.3: old method seen in the top row, new method in the bottom. The atrial source and aortic sink are visualized as areas without streamlines, as the stream function is not defined in these regions where the divergence of the velocity is not zero. To enable construction of a stream function, two cuts have been introduced to connect the source and sink with the external source/sink. The final volume appears approximately equal in both rows, but as seen in Figure 3.4, about a third of the volume was lost through the numerical leak and not ejected through the aorta. Note also that the heart appears to rotate: see text for explanation.

Figure 3.5 Computed Heart Boundary and Streamlines, Source and Sink ON

Chapter 4.

Effects of Mitral Apparatus Geometry On Mitral Flow and Leaflet Motion: A Computer Study [1]

Beth Feller Printz[2], Charles S. Peskin, Ph.D.[3],

Edward L. Yellin, Ph.D.[4], and Louis Evan Teichholz, M.D. [5]

---

[1]Submitted, Journal of the American College of Cardiology, May 1992

[2]Department of Physiology, Mount Sinai School of Medicine 1 Gustave Levy Place New York, NY 10029

[3]Courant Institute of Mathematical Sciences, New York University 251 Mercer Street New York, NY 10012

[4]Department of Cardiothoracic Surgery, and Department of Physiology and Biophysics, Albert Einstein College of Medicine 1300 Morris Park Avenue Bronx, NY 10461

[5]Department of Medicine, Division of Cardiology, Mount Sinai School of Medicine

Abstract

To study the relationship between mitral valve structure and function, the computational methods of Peskin, McQueen, et. al. are used to explore the effects of mitral valve geometry on transmitral flow dynamics, leaflet coaptation, and mitral valve prolapse. Different mitral valve geometries are modeled by independently varying the lengths of the mitral valve leaflets and/or chordae tendineae and papillary muscle, thereby simulating possible valve pathologies. It is found that: 1) When the mitral leaflets and total mitral apparatus are lengthened, there is an increase in early systolic backflow without true regurgitation; 2) A decrease in leaflet coaptation can lead to mitral prolapse and true mid to late systolic regurgitation; 3) Diastolic transmitral flow patterns can be significantly altered solely by changing mitral apparatus lengths.

These results should lead to an increased awareness of how mitral apparatus geometry can influence diastolic and systolic heart function. In particular, this information may help explain the heterogeneity of the clinical syndrome of mitral valve prolapse, the occurrence of "early systolic regurgitation" through normal and abnormal mitral valves, and the variation in diastolic flow that have been observed without myocardial pathology. Because the effects of changes in mitral apparatus lengths are analyzed, this study may also be useful in surgical reconstruction of the diseased mitral valve.

Introduction

Two-dimensional, pulsed, and color Doppler ultrasound have been used to study the anatomical and physiological conditions that define the prolapsing or redundant mitral valve (1-3), diastolic transmitral flow dynamics (4,5), and systolic regurgitation through the normal (6-10) and prolapsing (11-13) mitral valve. Even with these diagnostic tools, an in-vivo exploration of the relationship between mitral valve geometry and flow dynamics is difficult. A computational model of the heart developed by Peskin and McQueen is used in this study to explore the relationship between mitral geometry and flow.

The Peskin–McQueen computational model has been used to study a few aspects of diastolic and early systolic mitral valve physiology and pathophysiology (14-18). (*Early systole* will refer to the time before aortic outflow begins.) When Peskin and McQueen et. al. examined the computationally-measured flow through the normal mitral annulus, they made an observation that is particularly relevant to the present study: blood was flowing back towards the atrium during early systole (16-18). Two possible mechanisms for this early systolic backflow were described (16): that it represented true regurgitation, or that it was non-regurgitant displaced-volume backflow. If the flow were true regurgitation, blood from the left ventricle would pass between the mitral leaflet tips, through the annulus, and into the left atrium. On the other hand, if the flow represented displaced- volume backflow, blood not yet in the ventricle (nor through the leaflet tips) would be caught between the leaflets and carried into the atrium as the leaflets themselves were displaced toward the atrium upon valve closure. This non-regurgitant backflow mechanism has alternately been described as the "closing volume" of the valve (5,7,19). Therefore, these two mechanisms could be differentiated based on the presence or absence of flow through the leaflet tips.

Previous data from computational studies (15-18) and from invasive dog experiments

(18) indicate that the normal mitral valve closes with a small volume of backflow through the mitral valve annulus while almost no flow can be measured between the leaflet tips, consistent with a non-regurgitant displaced-volume mechanism for the observed early systolic backflow. The magnitude of this backflow was shown to depend on the timing of atrial systole (18). This mechanism may explain, at least in part, the clinical observation of "early systolic regurgitation" through the normal mitral valve using Doppler ultrasound (6,7,19).

When McQueen and Peskin simulated one form of mitral valve prolapse by decreasing papillary muscle tension (16), they found that the mitral valve first closed competently, accompanied by a spurt of early sysolic displace-volume backflow. This was followed in mid systole by prolapse of the posterior leaflet and true regurgitation. Would other variations in mitral apparatus geometry lead to changes in the amount of displaced- volume backflow, the amount of true regurgitation, or both? Would any such changes be accompanied by mitral leaflet prolapse? There seems to be an increased prevalence of early systolic backflow seen clinically with mitral valve prolapse or volume depletion (12,20, and LE Teichholz, Unplublished data): what is the mechanism of this backflow? Finally, would diastolic flow patterns also be changed?

In order to address these questions, a series of computational experiments was performed where different mitral valve parameters (leaflet, chordal and papillary muscle length) were varied, both in absolute terms as well as relative to each other.

Methods

The mathematical formulation of this method has been described previously (14-19) and will be only summarized here. The plane chosen for two- dimensional simulation is a cross-section of the heart bisecting the anterior and posterior leaflets of the mitral valve, intersecting the apex and left ventricular outflow tract (Fig. 4.1A–B). This representation is similar to an apical long axis view of the left heart on two-dimensional echocardiography. The initial computational representation of this plane can be seen in Fig. 4.1C–D. This configuration corresponds to the onset of left ventricular filling: the atrium is fully relaxed, the ventricle is in the isovolumic relaxation phase at the time of mitral valve opening, and falling left ventricular pressure has just crossed the left atrial pressure. Geometric and flow parameters were chosen to correspond to data from invasive dog experiments (16,18); these can be varied to simulate different initial heart or valve configurations, either to agree with experimental data or to investigate the influence of a particular parameter on flow patterns and heart performance.

In the present investigation, the model has been improved to allow the ejection of blood from the ventricle during systole when ventricular pressure exceeds aortic pressure. Though there is no actual aortic valve modeled, there is a resistive sink with aortic properties located in the tip of the ventricular outflow tract where the aortic valve should be. There has also been a change in the mathematical formulation to improve volume conservation (22).

The heart walls and mitral valve are represented as a series of points superimposed on a fluid mesh. These points are connected by links that have the properties of Hill's three-component muscle model, including parallel and series elastic elements plus a contractile element as described by Braunwald et. al. (16,23). The model mitral valve is comprised of two thin, asymmetric flexible leaflets without contractile properties. The initial configura-

tion of these leaflets is mathematically constructed from two circular arcs tangent to each other at their free margins and pointing toward the apex (Refer to Fig. 4.1C–D).

Papillary muscle and chordae, which anatomically lie outside the plane of the model, are represented as a Y-shaped force-generating structure connecting the free margins of the mitral valve to the apex, as shown in Fig. 4.1D. In a three-dimensional heart, chordae and papillary muscles would alter the flow patterns, since blood would have to move around these structures. Here, however, we model the chordae and papillary muscle as force-generating links that do not interfere with flow. The net effect is that the proper restraining forces can be represented while blood flow in this two-dimensional model is not obstructed.

As the computation proceeds over time, the boundary points that represent the heart wall and valve leaflets apply forces to the fluid. These forces depend on the heart configuration, and muscular and elastic properties of the boundary. The Navier-Stokes equations for incompressible flow are used to compute the fluid velocity throughout the heart at each time step. This fluid motion in turn moves the heart wall and valve leaflets.

Data from a computational heartbeat can be displayed as plots of flow, velocity, pressure, and chamber volume versus time, as well as simulated M-mode echocardiograms and phonocardiograms. Flow patterns can be displayed as streamlines at each time step, as a video of fluid markers moving with the blood inside the heart (similar to the clinically-used bubble injection technique or contrast angiography), or even as simulated color-Doppler ultrasound images. One complete heartbeat consists of 960 computational time steps and lasts 675 msec (a rate of 88 beats/minute). The ventricle begins to contract about 450 msec after mitral valve opening, blood ejection begins approximately 50 msec later, and peak ventricular pressure is reached at about 560 msec.

The study reported here consisted of three series of experiments in which the parameters

that define the lengths of the mitral valve leaflets and/or chordae and papillary muscle were changed: (Refer to Fig. 4.1C-D)

Series I. Constant Total Length:

Mitral valve leaflet length was increased (and decreased) while chordae plus papillary muscle length was shortened (lengthened) to maintain constant total ventricular axis length (i.e. distance VA was constant). This was accomplished by increasing (decreasing) the proportion of the ventricular axis that determines the valve arc length (from the mitral annulus to the mitral cusp) while decreasing (increasing) by an equal amount the proportion that determines the chordae plus papillary muscle length (from the mitral cusp to the ventricular apex).

Series II. Variable total length of valve plus chordae/papillary muscle complex, either mitral valve or chordae/papillary muscle length changed:

A. Length of the valve leaflets changed while keeping chordae/papillary muscle length constant.

B. Chordae/papillary muscle length changed while holding valve length constant.

Series III. Variable total length, both valve and chordae/papillary muscle length changed in same direction:

Both mitral valve and chordae/papillary muscle length simultaneously made longer or both made shorter, increasing or decreasing the total apparatus length (i.e. the distance from the mitral annulus to the ventricular apex.)

In all experiments, note that the chordae comprise one third of the distance from the mitral cusp to the ventricular apex, while the papillary muscle comprises the remaining

two thirds (again refer to Fig. 4.1C-D). One should also note that the size of the mitral annulus has not been varied independently in any of the experimental series, although it does change as the dynamic forces on the mitral apparatus change.

Computational data will be presented below as planar images of the heart and valve configuration with flow streamlines, together with plots of volume flow, velocity, and annular and cusp diameter versus time.

Conceptual Definitions:

Mitral valve prolapse is here defined as posterior displacement of part of the valve leaflet(s) beyond the mitral annulus (i.e. toward the atrium); this has been termed "billowing mitral leaflets" elsewhere (19,23). Prolapse does not imply that the valve leaflets are larger than normal: those will be referred to as redundant mitral leaflets. Prolapse also will not imply mitral regurgitation. As explained above, early systolic backflow will be a general term describing blood moving toward the atrium across the plane of the mitral annulus. It may be due to true regurgitation, displaced-volume backflow, or a combination of the two.

Results

Series I: Constant total apparatus length, variable mitral or chordae plus papillary muscle length.

All frames of Figure 4.2 (as well as Figs. 4.4, 4.6 and 4.8) illustrate the heart wall, mitral valve and the fluid streamlines when ventricular volume is at a minimum (i.e. at end ejection), just before isovolumic relaxation begins. This occurs 590 msec after mitral valve opening. Frames 4.2A–E are from different experiments, as described below. In each frame, there are two square regions connected by cuts to the left margin where the streamlines are absent: one region in the atrium, and one in the ventricular outflow tract. These two areas correspond to the locations of the atrial source (which models pulmonary venous return) and ventricular sink (which models aortic outflow), respectively.

As the total chordae plus papillary muscle length length is increased from 30% shorter to 20% longer than the control and mitral valve length decreased by an equal amount, the coaptation of the mitral leaflets decreases (Fig. 4.2A–D). With a normal valve (Fig. 4.2C) or with longer valve and chordae/papillary muscle (Fig. 4.2A–B) there is no prolapse, but when chordae/papillary muscle length is increased 20% and the valve is shortened 20%, the posterior mitral leaflet prolapses across the plane of the mitral annulus, though the leaflets still coapt slightly (Fig. 4.2D).

As chordae/papillary muscle length is increased and valve length decreased by 30%, the leaflets no longer coapt, the posterior leaflet prolapses, and the valve becomes incompetent (Fig. 4.2E). Thus, increased chordae/papillary muscle length with decreased leaflet length causes decreasing coaptation and increasing prolapse of the posterior mitral leaflet, eventually leading to valvular incompetence. In contrast, decreased chordae/papillary muscle length with increased mitral leaflet length increases coaptation and does not lead to mitral

valve prolapse. This incompetent valve does return to a normal configuration as ventricular pressure falls just before the next diastole would begin.

Additional results from this series of experiments can be seen in plots of flow volume, velocity, and annular and cusp diameter versus time (Fig. 4.3). As chordae/papillary muscle length is increased from 30% shorter to 30% longer than the control (and leaflet length changed inversely), there is only a very slight decrease in early systolic backflow through the annulus (Fig. 4.3A, arrow 1) or through the leaflet tips (Fig 4.3B, arrow 1). Thus, if the length of the entire mitral apparatus remains constant, there is little change in the amount of early systolic backflow: a small volume of non-regurgitant flow is present, but almost no true early systolic regurgitation occurs.

In contrast to the lack of significant true early systolic regurgitation, significant true mid to late systolic regurgitation can be seen when the chordae/papillary muscle is longest and valve leaflets are shortest, as flow can be seen through both the annulus and between the leaflet tips (Fig. 4.3A–B curve e, arrow 2). Note that this is the same valve that prolapsed in mid systole, and that there was no accompanying significant true *early* systolic regurgitation.

Early and late diastolic flow peaks are also changed as the valve and chordae/papillary muscle length are varied (indicated by the asterisk in Fig. 4.3A–B): as chordae/papillary muscle length is increased and leaflet length decreased, peak diastolic flow through the valve increases. At the same time as this flow change, there is an increase in cusp area (area between the leaflet tips), though annular area remains virtually constant in all cases (Fig. 4.3C). While the peak diastolic velocity measured at the annulus increases as flow is increased (Fig. 4.3D), peak velocity at the level of the leaflet tips decreases as the chordae and papillary muscle are lengthened and valve leaflets shortened (Fig. 4.3E).

Series IIA: Mitral valve leaflet length varied without changing chordae/papillary muscle length.

As in the first experimental group, the coaptation length increases as the valve leaflets are made progressively longer (Fig. 4.4A–C), but the magnitude of the change is much less here where chordae/papillary muscle length is held constant than in the first experimental group where chordae/papillary muscle length was decreased. As the valve leaflets are shortened the valve does not prolapse, whereas when the leaflets are lengthened there is a slight amount of prolapse (Fig. 4.4C). These changes are opposite to the changes seen in Series I, where the shorter valve with longer chordae/papillary muscle prolapsed while the longer valve did not.

Looking at the plots of flow versus time for this experimental series, one can see that early systolic backflow through the mitral valve annulus increases significantly with only a small change in flow through the leaflet tips as leaflet length is increased without changing chordae/papillary muscle length (Fig. 4.5A–B). This is consistent with a displaced-volume origin for the majority of the backflow, rather than the backflow constituting true regurgitation. Though the regurgitant volume is quite small, there is an increase in the peak velocity of this flow with shorter leaflets (Fig. 4.5D, arrow 1).

Peak early diastolic flow through the mitral annulus and cusp change only slightly (Fig. 4.5A–B, asterisk) while peak cusp area and velocity increase as the mitral leaflets are made longer (Fig 4.5C–D, asterisk). This is in contrast to the significantly decreased peak diastolic flow and cusp area seen in the first experimental group, where chordae/papillary muscle length is decreased and leaflet length increased. Late diastolic flow and velocity peaks do not change substantially.

Series IIB: Chordae/papillary muscle length changed; leaflet length constant.

Fig. 4.6A–C shows that as chordae/papillary muscle length is increased from 30% shorter to 30% longer than the control, the coaptation length decreases with only slight valve prolapse. Note in Fig. 4.7A–B that as chordae/papillary muscle length is increased, peak early systolic backflow through the annulus and leaflet tips increases only slightly (arrow 1), in contrast to the significant increase in early systolic flow seen when mitral leaflet length was increased. Again, no significant early systolic backflow (i.e. true regurgitation) was seen through the mitral cusp. As in the first experimental group, peak early and late diastolic flow and leaflet tip separation (Fig. 4.7C, asterisk) increase as CPM length increases, and the velocity at the leaflet tip level again decreases (Fig. 4.7D, asterisk).

Series III: Both valve leaflet and chordal/papillary muscle length changed in the same direction.

As both mitral leaflet and chordae/papillary muscle length are increased, the valve prolapses slightly (Fig. 4.8). Coaptation length increases as both lengths are increased from 30% shorter to normal; further length increases do not change leaflet coaptation. One can see in Fig. 4.9A–B that there is a very large increase in the early systolic backflow as leaflet, chordal and papillary muscle length are increased by 30%, with almost no backflow through the mitral tips indicative of true regurgitation. Early and late diastolic flow peaks increase as the valve and chordae/papillary muscle lengths are increased. There is also a substantial increase in peak tip separation area during both early and late diastole (Fig. 4.9C, asterisk); the increased flow and leaflet separation is again accompanied by a decrease in peak early and late diastolic blood velocity through the leaflet tips (Fig. 4.9D, asterisk).

Discussion

This study demonstrates the importance of the relative and absolute lengths of the valve, chordae and papillary muscle in determining coaptation length, degree of prolapse upon valve closure, the amount and type of backflow observed through the mitral valve, and diastolic mitral valve motion and flow.

Change in leaflet coaptation

Leaflet coaptation was primarily related to chordae plus papillary muscle length: when the chordae and papillary muscle were made longer coaptation decreased, while coaptation increased when the chordae and papillary muscle were shortened. Coaptation was secondarily related to leaflet length, as longer leaflets led to only a small increase in coaptation. When both valve and chordae/papillary muscle were lengthened, these opposing changes in coaptation partially canceled each other and coaptation length was close to normal. Coaptation decreased, however, when both the valve leaflets and chordae/papillary muscle were shortened 30%. Perhaps the total length of valve plus chordae/papillary muscle was so short compared to the size of the mitral annulus that the leaflets were geometrically prevented from coapting normally.

Degree of mitral valve prolapse

The degree of prolapse was related to the degree of leaflet coaptation and the total length of the valve plus chordae/papillary muscle. Increased leaflet coaptation may prevent prolapse when leaflets are longer and chordae/papillary muscle shorter. Conversely, the valves with longer chordae and papillary muscle and shorter leaflets had decreasing coaptation until the valve prolapsed and became incompetent. The excessively long chordae/papillary

muscle with little or no leaflet coaptation seemed to be incapable of restraining the valve from prolapsing into the atrium. This result agrees with data from Barlow that a decrease in leaflet coaptation can lead to mitral valve prolapse and valvular incompetence (20). It is also in agreement with geometric analyses by Miller and Marcotte (25) and Bryhn and Garding (26), who found that if leaflet and/or chordae and papillary muscle length is varied, coaptation could decrease and result in a prolapsing, incompetent valve. It may also explain the increase in prolapse and regurgitation observed in certain cases of mitral annular dilatation (11,27): as the annulus expands, constant length leaflets will not be able to coapt normally. Prolapse occurred in the second and third experimental protocols when the length of the entire valve plus chordae/papillary muscle complex was increased. Though prolapse was present, coaptation remained normal: the longer mitral valve complex may have nowhere else to go as the ventricle contracts but toward the left atrium. Clinically, this may correspond to cases of mitral valve prolapse where mitral leaflet and/or chordae are thought to be longer than normal. The increase in mitral prolapse which has been reported following volume depletion (28) can also be explained in this manner, as there would exist a relative increase in size of the mitral apparatus components in comparison with atrial and/or ventricular dimensions.

Early systolic backflow:

Early systolic backflow at the level of the mitral annulus was often seen without substantial backflow between the leaflet tips. This is consistent with previous computational (16,18) and experimental (18) results that normal and certain abnormal mitral valves initially close competently without substantial regurgitation. It also supports the closing volume mechanism (5,7,19) for normal early systolic "regurgitation" detected by Doppler ultrasound.

There was a large increase in this amount of early systolic non-regurgitant backflow in all cases where leaflet length was increased without decreasing chordae/papillary muscle length. This is consistent with idea that longer leaflets can engulf more blood, which is then carried through the mitral annulus as the leaflets are displaced toward the atrium during valve closure. The increased non-regurgitant backflow observed in this experimental series may explain why patients with redundant mitral leaflets and/or mitral valve prolapse seem to have a higher occurrence of clinically reported early systolic mitral "regurgitation" than do subjects with normal valves (12,20), while in fact no significant true regurgitation may be present. Konicek et. al. reported that acute blood loss (through blood donation) could result in decreased left atrial dimensions and early mitral regurgitation without the occurrence of mitral valve prolapse (21), which would seem to disagree with the results of Eicher et. al. mentioned previously (28). It would be interesting to measure valve parameters in subjects such as these to look for *relative* redundancy of the mitral apparatus, even without true mitral valve prolapse.

Though no substantial early systolic true regurgitation was seen in any of the experiments performed, there was often an increase in the velocity of the very small volume of early systolic regurgitation through the mitral leaflet tips as leaflet length was increased. Even normal valve closure produced a small velocity jet toward the atrium in early systole. This very low volume high velocity jet may be detected by clinical Doppler ultrasound examination. It should be emphasized that the volume of this true regurgitation is substantially less than the volume of the non-regurgitant backflow discussed above.

Presence of true mid to late systolic regurgitation:

In the current experimental series, true mid to late systolic regurgitation only occurred

when leaflet length was decreased 30% and chordae/papillary muscle length increased 30%. The mitral valve prolapsed substantially and leaflet coaptation became inadequate, resulting in valvular incompetence. The timing of this prolapse and true mitral regurgitation is similar to clinical mitral valve prolapse, where the leaflets (especially the posterior leaflet) prolapse into the atrium and a mid-systolic click is followed by a murmur (if regurgitation occurs), with the valve returning to its correct orientation just before diastole begins.

Impact on diastolic mitral flow:

Increased leaflet length and decreased chordal and papillary muscle length caused a large decrease in peak early and late diastolic flow (Figs. 4.3, 4.5, 4.7 and 4.9). As seen by the decrease in leaflet tip separation, the shorter chordae and papillary muscle may restrain the valve from fully opening, resulting in a functional stenosis due to a decreased flow area. The increase in velocity through the leaflet tips despite the decrease in flow volume is consistent with this explanation. This change in early diastolic flow was not as dramatic when chordae/papillary muscle length was held constant. This result is consistent with experimental data from Keren et. al. (29) that an increase in valvular resistance can cause a decrease in peak diastolic flow, and is one example of how diastolic flow patterns (and subsequent systolic function) can be changed without myocardial dysfunction (5).

Limitations:

Although a model is only a representation of the actual processes being studied and limitations are inevitable, this model has previously given valuable insights into cardiac physiology and pathophysiology [with good agreement when compared to experimental data] (15-18). A dog heart was chosen to model because of the availability of experimental

data; this may lead to different results than if a human heart were modeled. The method is now being modified to include more realistic human parameters. For computational reasons, the Reynold's number has also been reduced. This has the effect of increasing the viscous forces relative to the inertial forces. Evidence has been given in earlier reports of this method that the inertial effects still dominate (5,16). Another limitation is that a two-dimensional model cannot take into account the three-dimensional saddle-shaped mitral valve geometry described by Levine, et. al. (3). A three-dimensional model is now being developed that would remove this limitation (30,31). Finally, although we have explored a wide range of different mitral apparatus geometries in this study, we have not looked at all circumstances that would be of clinical import. For example, we have not independently changed the size of the mitral annulus, atrium or ventricle. Boltwood, et. al. (32) found that the increased mitral regurgitation seen in dilated cardiomyopathy was accompanied by annular dilatation and a decrease in coaptation. They did not observe prolapse or lack of coaptation in any patient, however, as the leaflets were constrained within the ventricle. It would be interesting to simulate this condition by changing the initial shape of the model ventricle.

Summary:

This study provides a conceptual framework of how mitral apparatus geometry can alter transmitral flow and valve motion. In particular, we have found that: 1) When the mitral leaflets and total mitral apparatus are lengthened, there is an increase in early systolic backflow without true regurgitation; 2) A decrease in leaflet coaptation can lead to mitral prolapse and true mid to late systolic regurgitation; and 3) Diastolic transmitral flow can be significantly altered solely by changing mitral apparatus lengths. Although

care must be taken when extrapolating from a model to clinical situations, we believe that our results have clinical relevance. Our finding of significant non-regurgitant early systolic backflow emphasizes the clinical conclusion that care should be taken when "early systolic regurgitation" is reported by Doppler ultrasound, as much of this measured flow may not be true regurgitation. Because we have described results of specific changes in mitral apparatus parameters, this study may also be useful in determining the optimal design for surgical reconstruction of diseased mitral valves (24,33). We now plan to compare Doppler ultrasound measurements of valve apparatus parameters and transmitral flow in patients who have redundant mitral leaflets, mitral valve prolapse, and in normal controls, to our computational data.

Acknowledgment:

The authors are indebted to David M. McQueen for numerous helpful discussions and for supercomputing assistance.

References

[1] Ormiston JA, Shah PM et al. Size and motion of the mitral valve annulus in man. II. Abnormalities in mitral valve prolapse. Circulation 1982;65:713-719.

[2] Krivokadich J, Child JS, Berge J, Dadourian MD, Perloff JK. Reassessment of echocardiographic criteria for the diagnosis of mitral valve prolapse. Am J Cardiol 1988;61:131-135.

[3] Levine RA, Handschumacher MD, Sanfilippo AJ, et al. Three-dimensional echocardiographic reconstruction of the mitral valve with implications for the diagnosis of mitral valve prolapse. Circulation 1980;80:589-598.

[4] Nishimura RA, Abel MD, Hatle LK, Tajik AJ. Assessment of diastolic function of the heart: background and current applications of Doppler echocardiography, Part II. Mayo Clin Proc 1989;64:181-204.

[5] Yellin EL, Nikolic S, Frater WM. Left ventricular filling dynamics and diastolic function. Prog Cardiov Dis 1990;32:247-271.

[6] Kostucki W, Vandenbossche JL, Friart A, Englert M. Pulsed Doppler regurgitant flow patterns of normal valves. Am J Cardiol 1986;58:309-313.

[7] Pollak ST, McMillan SA, Knopff WD, et al. Cardiac evaluation of women distance runners by echocardiographic color Doppler flow mapping. J Am Coll Cardiol 1988;11:89-93.

[8] Yoshida K, Yoshikawa J, Shakudo M, et al. Color Doppler evaluation of valvular regurgitation on normal subjects. Circulation 1988;78:840-847.

[9] Berger M, Hecht SR, Van Tosh A, Lingam U. Pulsed and continuous-wave Doppler echocardiolgraphic assessment of valvular regurgitation in normal subjects. J Am Coll Cardiol 1989;13:1540-1545.

[10] Choong CY, Abascal YM, Weyman J, et al. Prevalence of valvular regurgitation in patients with structurally normal hearts by two-dimensional echocardiography. Am Heart J 1989;117:636-642.

[11] Panidis IP, McAllister M, Ross J, Mintz GS. Prevalence and severity of mitral regurgitation in the mitral valve prolapse syndrome: a Doppler echocardiographic study of 80 patients. J Am Coll Cardiol 1986;7:975-981.

[12] Akasaka T, Yoshiwara J, Yoshida K, Yamaura Y, Hozumi T. Temporal resolution of mitral regurgitation in patients with mitral valve prolapse: a phonocardiographic and Doppler echocardiographic study. J Am Coll Cardiol 1989;13:1053-1061.

[13] Grayburn PA, Berk MR, Spain MG, Harrison MR, Smith MD, DeMaria AN. Relation of echocardiographic morphology of the mitral apparatus to mitral regurgitation in mitral valve prolapse: Assessment by Doppler color flow imaging. Am Heart H J 1990;119:1095-1102.

[14] Peskin CS. Numerical analysis of blood flow in the heart. J Comput Physics 1977;25:220-252.

[15] Yellin EL, Peskin CS, Yoran C, et al. Mechanics of mitral valve motion during diastole. Am J Physiol 1981;241:H389-400.

[16] McQueen DM, Peskin CS, Yellin EL. Fluid dynamics of the mitral valve: physiological aspects of a mathematical model. Am J Physiol 1982;242:H1095-1110.

[17] Peskin CS. The fluid dynamics of heart valves: experimental, theoretical and computational methods. Ann Rev Fluid Mech 14;1982:235-259.

[18] Meisner JS, McQueen DM, Ishida Y, et al. Effects of timing of atrial systole on left ventricular filling and mitral valve closure: computer and dog studies. Am J Physiol 1985;249:H604-619.

[19] Sahn DJ, Maciel BC. Physiological valvular regurgitation. Doppler echocardiography and the potential for iatrogenic heart disease. Circulation 1988;78:1075-1077.

[20] Barlow JB and Pocock WA. Mitral leaflet billowing and prolapse. In: Barlow JB. Perspectives on the Mitral Valve. Philadelphia: FA Davis, 1987: 45-111.

[21] Konicek S, Guntheroth WG, Sylvester CE, Mack LA, Reichler RJ. Does "physiologic" MVP occur with acute blood loss? Clin Cardiol 1987;10:159-162.

[22] Peskin CS, Printz BF. Improved volume conservation in the computation of flows with immersed elastic boundaries. Submitted, J Comput Physics.

[23] Braunwald E, Ross J, Sonnenblick EH. Mechanism of Contraction of the Normal and Failing Heart. Boston: Little Brown, 1976:49-66.

[24] Frater RWM: Mitral Valvuloplasty. In: Roberts AJ, Conti CR, eds. Current Surgery of the Heart. Philadelphia: Lippincott, 1987:64-77.

[25] Miller GE, Marcotte H. Computer simulation of human mitral valve mechanics and motion. Comput Biol Med 1987;17:305-319.

[26] Izumi S, Miyatake K, Beppu S, et al. Mechanism of mitral regurgitation in patients with myocardial infarction: a study using real-time two-dimensional Doppler flow imaging and echocardiolgraphy. Circulation 1987;76:777-785.

[27] Keren G, Katz S, Strom J, Sonnenblick EH, LeJemtel TH. Noninvasive quantification of mitral regurgitation in dilated cardiomyopathy: correlation of two Doppler echocardiographic methods. Am Heart J 1988;116:758-764.

[28] Eicher M, Lax D, Goldberg SJ. Mild dehydration induces mitral valve prolapse in female volunteers with prior normal cardiac findings. J Am Coll Cardiol 1990;15;97A.

[29] Keren G, Meisner JS, Sherez J, et al. Interrelationship of middiastolic mitral valve motion, pulmonary venous flow, and transmitral flow. Circulation 1986;74:36-44.

[30] Peskin CS, McQueen DM. A three-dimensional computational method for blood flow in the heart: I. Immersed elastic fibers in a viscous incompressible fluid. J Comput Physics 1989;81:372-405.

[31] McQueen DM, Peskin CS. A three-dimensional computational method for blood flow in the heart: II. Contractile fibers. J Comput Physics 1989;82:289-297.

[32] Boltwood CM, Tei C, Wong M, Shah PM. Quantitative echocardiography of the mitral complex in dilated cardiomyopathy: the mechanism of functional mitral regurgitation. Circulation 1983;68;498-508.

[33] Gallaway CA, Calvin SB, Baumann FG, Harty S, Spencer FC. Current concepts in mitral valve reconstruction for mitral insufficiency. Circulation 1988;78:1087-1098.

Figure 4.1 Initial anatomy of the computational heart

A. Base of the heart, indicating orientation of computational plane. This plane bisects the anterior leaflet (AL) and posterior leaflet (PL) of the mitral valve and the aortic valve (Ao), and passes between the papillary muscles and chordae.

B. Cross section of the left heart in the plane of computation.

C. Computer model of the left heart with aortic valve closed. This model heart is superimposed on a 64 X 64 computational mesh. The heart wall and valve leaflets are composed of a series of points spaced at intervals of approximately 1/2 meshwidth.

MA - Mitral annulus (ring) level

MC - Mitral cusp (leaflet tip) level

VA - Ventricular axis (parallel to the leaflet tips), bisecting the mitral annulus, and ending at the ventricular apex.

D. Enlargement of the model left ventricle to show initial mitral valve, chordae and papillary muscle configuration.

(A, B, and D Reprinted with permission, Amer J Physiol.)

Figure 4.1A–B Initial anatomy of the computer heart

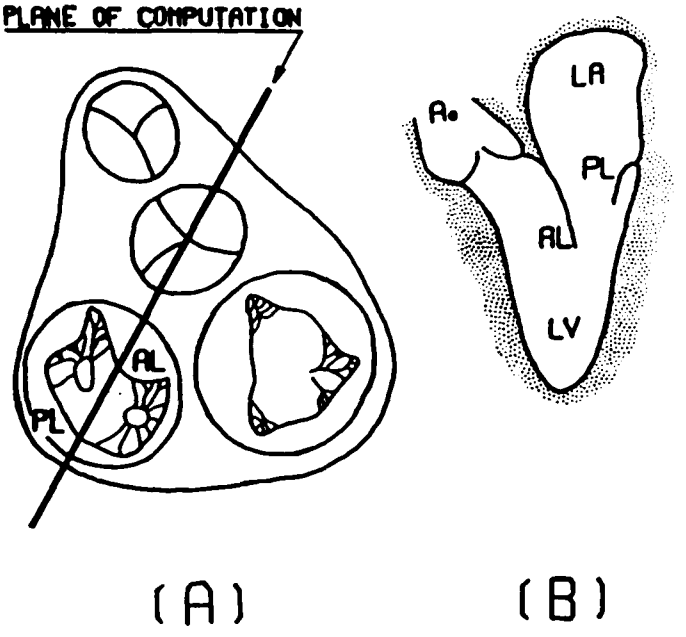

Figure 4.1C Computer model of the heart, aortic valve closed

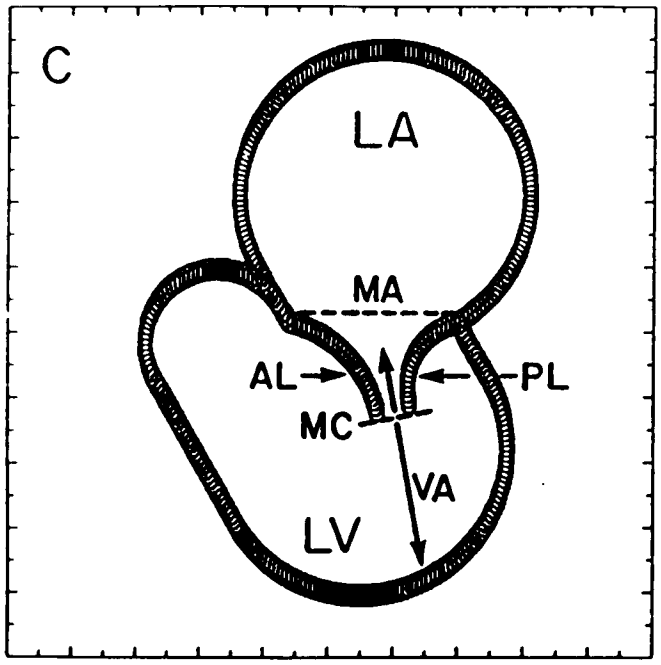

Figure 4.1D Enlargement of Model Left Ventricle

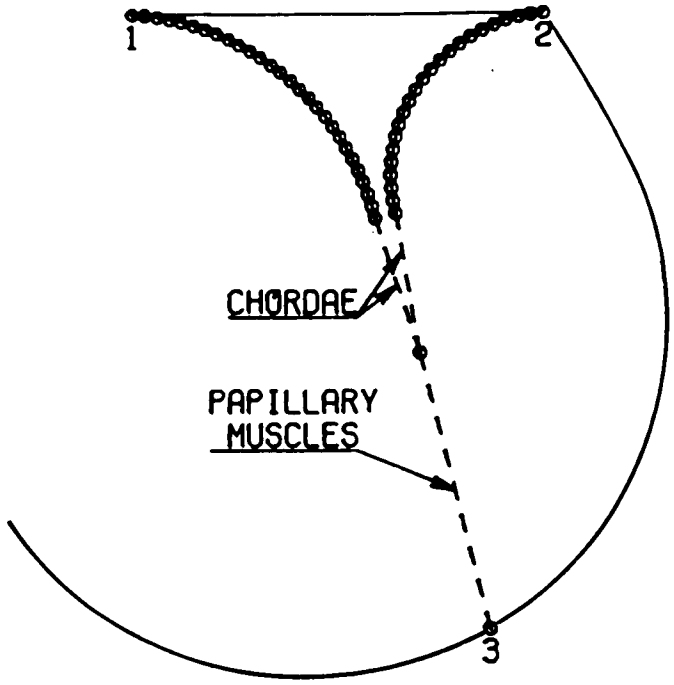

(D)

Figure 4.2 Computed heart and valve configuration with fluid streamlines at minimum of ventricular volume, 590 msec after the mitral valve begins to open. All subsequent streamline figures will also be at this time. Source (atrial inflow) and sink (ventricular outflow) locations are seen as areas without streamlines, as described in text.

A. Chordae plus papillary muscle (CPM) length decreased 30%; mitral leaflet (ML) length increased 30%.

B. CPM length decreased 20%; ML length increased 20%.

C. Normal CPM and ML length (Corresponds to Fig. 1D.)

D. CPM length increased 20%; ML length decreased 20%.

E. CPM length increased 30%; ML length decreased 30%.

Note that coaptation decreases as one goes from Fig 2A to E, and prolapse increases, with the mitral valve becoming incompetent in Figure 4.2E.

Figure 4.2 Computed Heart and Valve Configuration, Series I

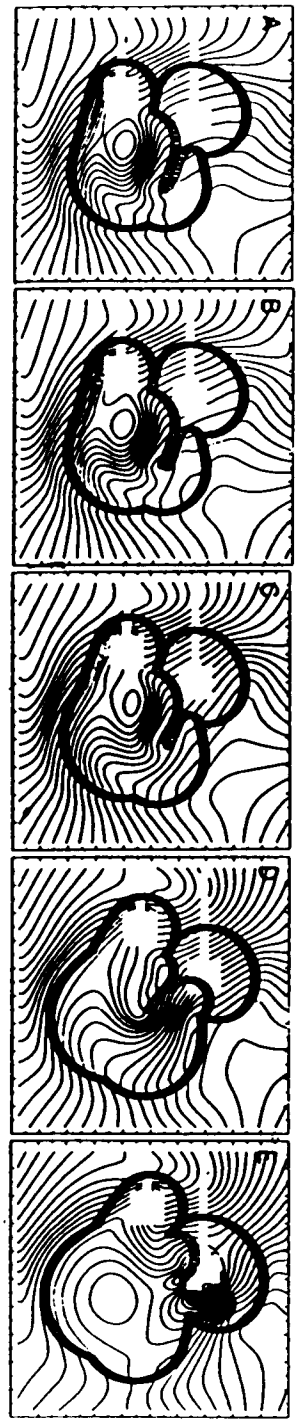

Figure 4.3 Mitral flow, diameter and velocity versus time, Series I, including data from the following three experiments:

(a)— - — - 30% shorter CPM; 30% longer ML

(b)———— Normal CPM and ML

(c)- - - - - 30% longer CPM; 30% shorter ML

Arrow 1 in this and subsequent figures corresponds to the peak early systolic backflow. Arrow 2 corresponds to the location of mid- to late-systolic true regurgitation. The asterisk corresponds to peak diastolic forward flow.

Figure 4.3 Mitral Flow, Diameter and Velocity, Series I

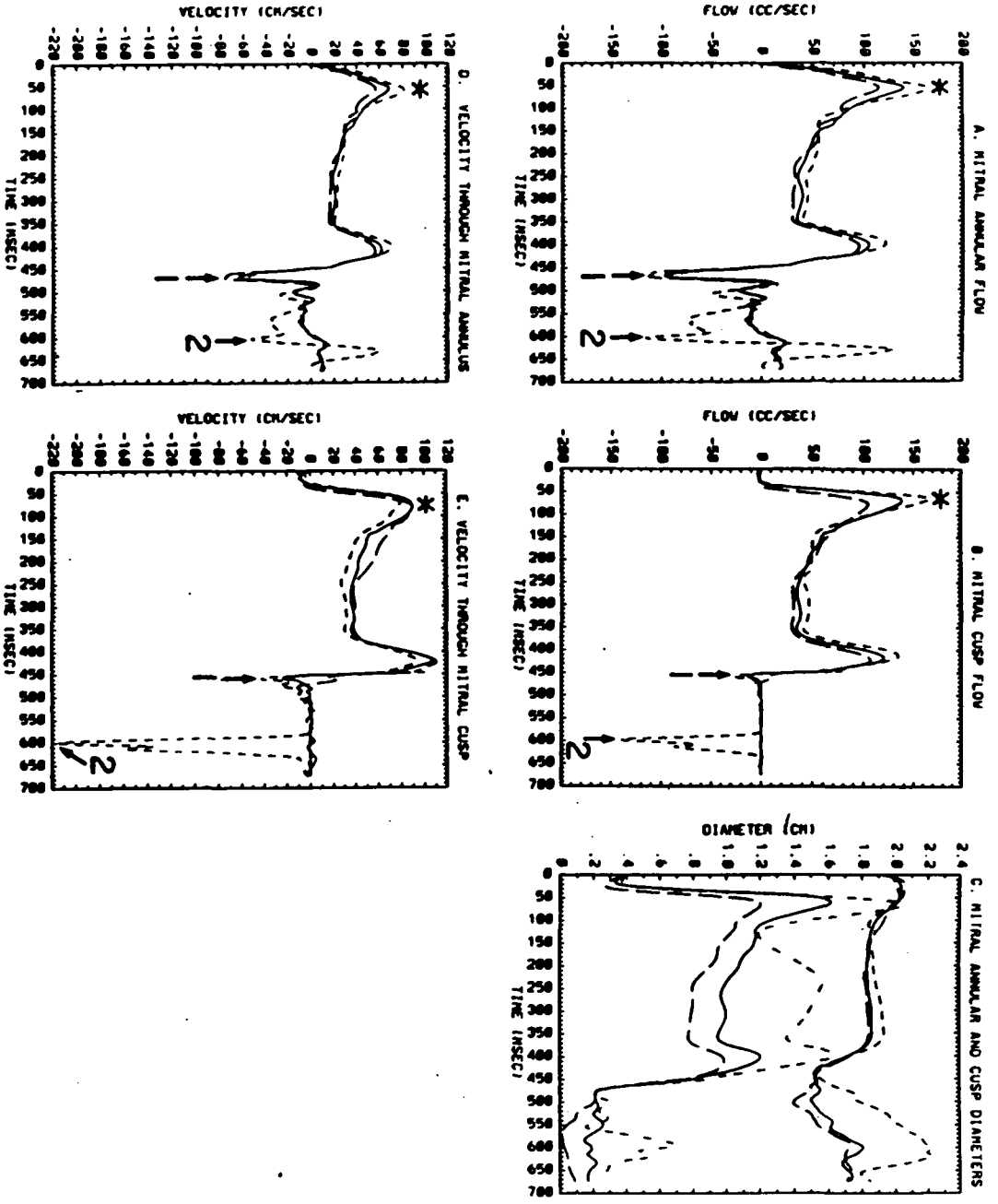

Figure 4.4 Computed heart and valve configurations and fluid streamlines, Series IIA (Mitral leaflet length varied; CPM length constant).

A. 30% shorter ML

B. Normal ML

C. 30% longer ML

Note that coaptation increases from Figure 4.4A–C, accompanied by a slight increase in the amount of prolapse.

Figure 4.4 Computed Heart and Valve Configuration, Series IIA

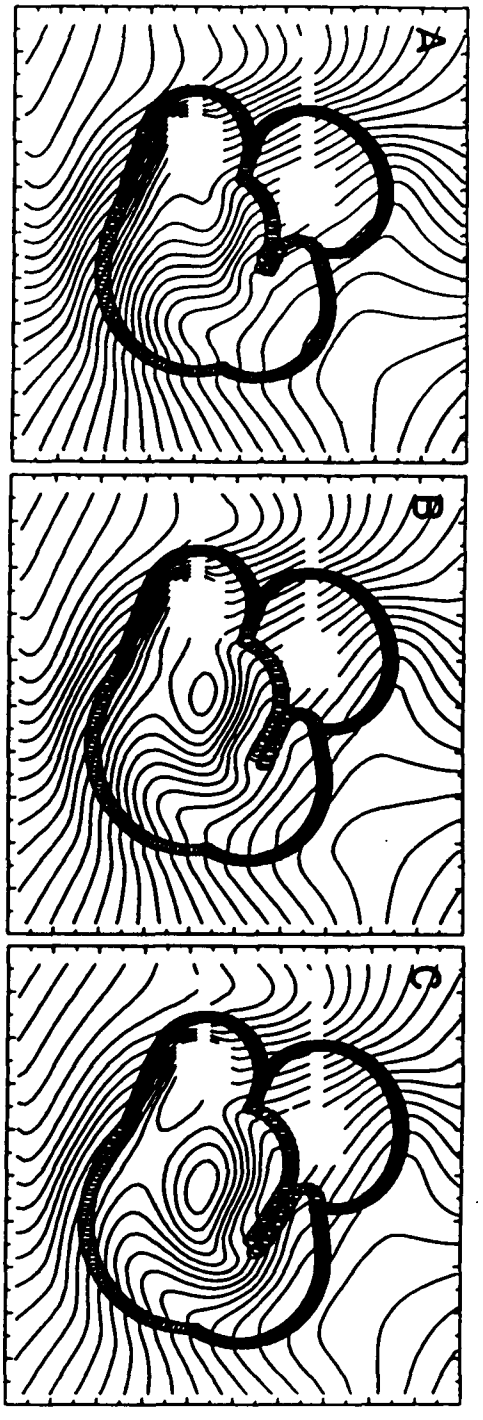

Figure 4.5 Mitral flow, diameter and velocity versus time, Series IIA.

(a)— - — - 30% shorter ML

(b)———— Normal ML

(c)- - - - - 30% longer ML

Peak early-systolic mitral annular backflow increases as one goes from case (a) to (c), without the appearance of any mitral cusp backflow. This is accompanied by an increase in peak early diastolic flow and cusp area, with a decrease in velocity (case (c)).

Figure 4.5 Mitral Flow, Diameter and Velocity, Series IIA

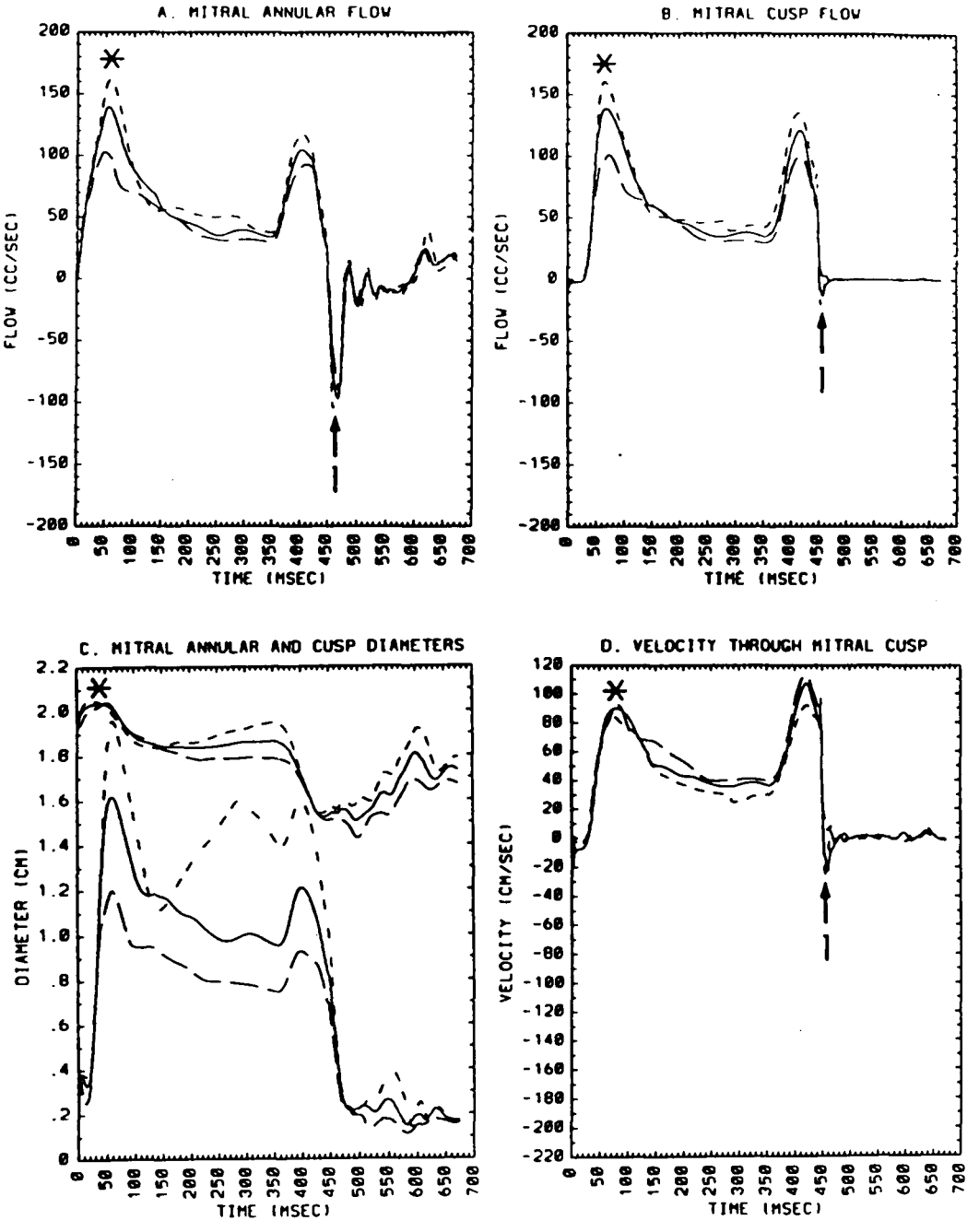

Figure 4.6 Computed heart and valve configuration and fluid streamlines, Series IIB (CPM length varied; Mitral leaflet length constant).

A. 30% shorter CPM

B. Normal CPM

C. 30% longert CPM

Coaptation length decreases slightly from Figure 4.6A–C, again with only a small amount of prolapse.

Figure 4.6 Computed Heart and Valve Configuration, Series IIB

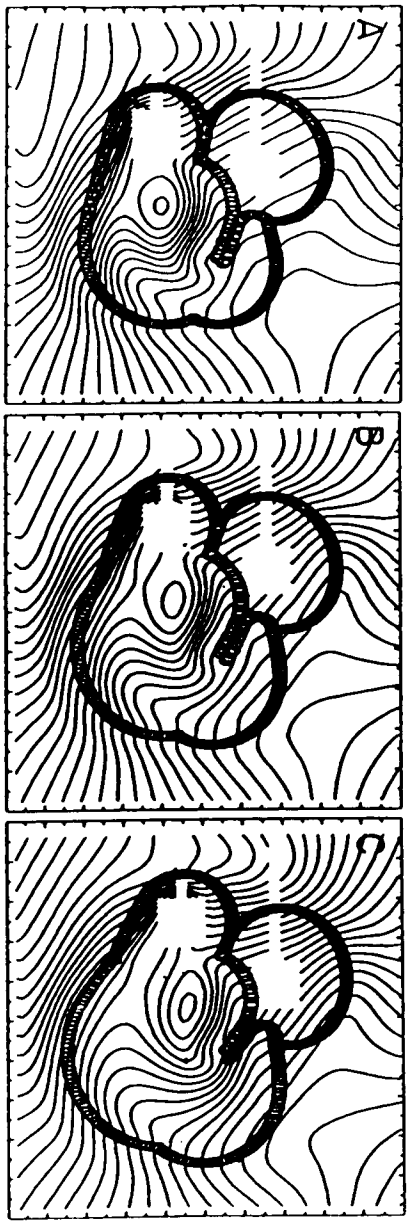

Figure 4.7 Mitral flow, diameter and velocity versus time, Series IIB.

(a)— - — - 30% shorter CPM

(b)———— Normal CPM

(c)- - - - - 30% longer CPM

Peak early-systolic mitral annular backflow increases only slightly (arrow 1), but peak diastolic flow and cusp diameter increase with a decrease in velocity as one goes from case (a) to (c) (asterisk).

Figure 4.7 Mitral Flow, Diameter and Velocity, Series IIB

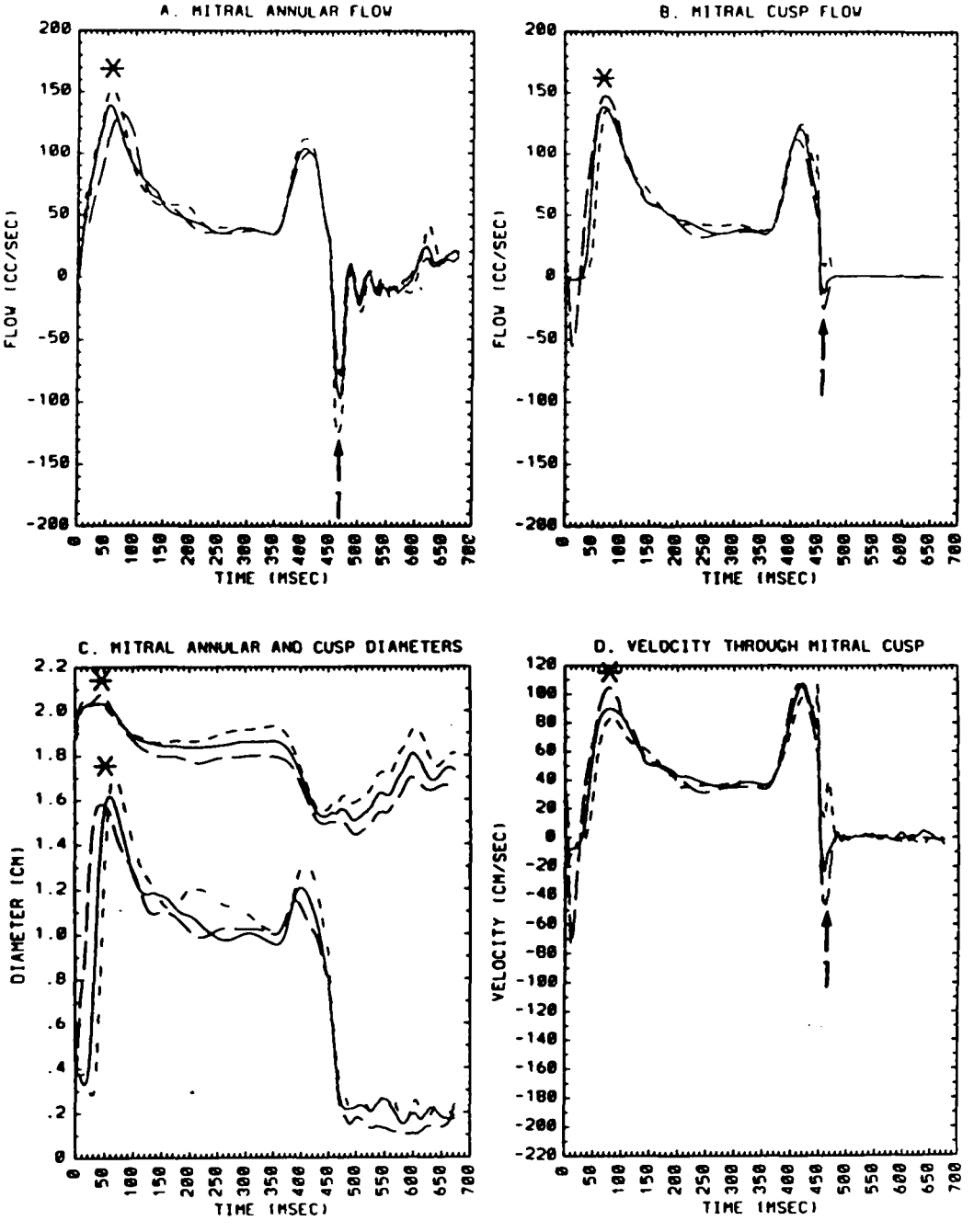

Figure 4.8 Computed heart and valve configuration and fluid streamlines, Series III (Mitral leaflet and CPM length both varied in same direction)

A. 30% shorter ML AND CPM

B. Normal ML AND CPM

C. 30% longer ML AND CPM

Figure 4.8 Computed Heart and Valve Configuration, Series III

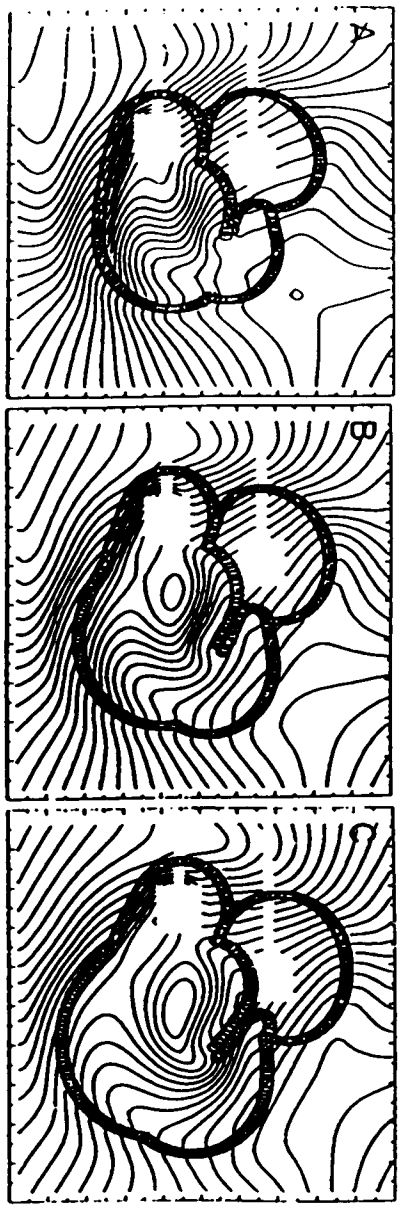

Figure 4.9 Mitral flow,diameter and velocity versus time, Series III

(a)— - — - 30% shorter ML AND CPM

(b)———— Normal ML AND CPM

(c)- - - - - 30% longer ML AND CPM

There is a large increase in early systolic mitral annular backflow as both ML and CPM are lengthened. There is also an increase in diastolic flow and leaflet tip separation, but a decrease in mitral cusp velocity from case (a) to (c).

Figure 4.9 Mitral Flow, Diameter and Velocity, Series III

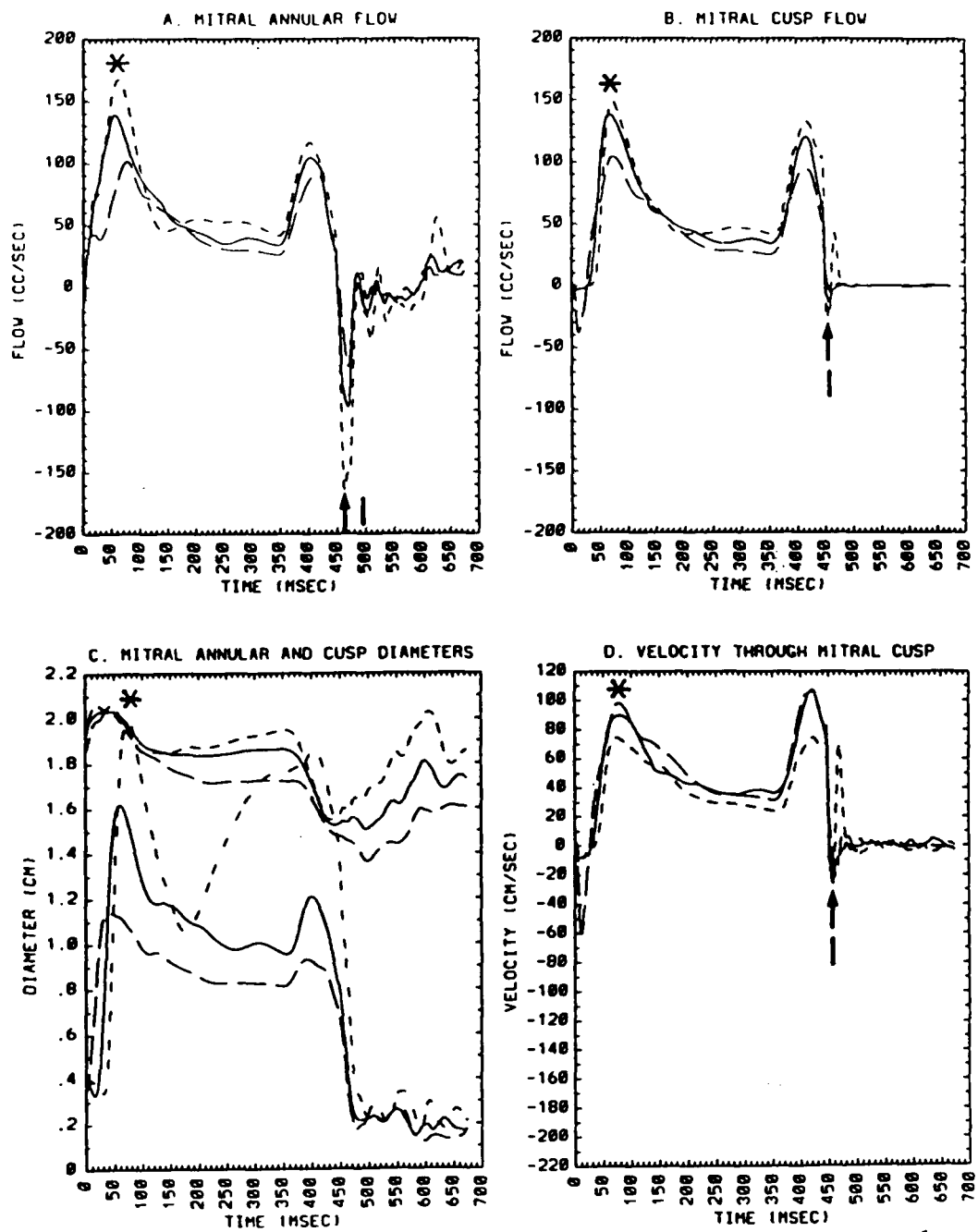

Chapter 5.

Computer Simulation of Color Doppler Ultrasound

Beth Feller Printz [1], Hadil S. Sabbagh [2],

Charles S. Peskin [3], and Louis E. Teichholz [4]

[1] Department of Physiology, Mount Sinai School of Medicine, New York, NY 10029

[2] Department of Computer Science, Courant Institute of Mathematical Sciences, New York University, New York, NY 10012

[3] Department of Mathematics, Courant Institute of Mathematical Sciences

[4] Division of Cardiology, Department of Medicine, Mount Sinai Medical Center

Abstract

A method to generate simulated color Doppler ultrasound images has been developed using the computational two-dimensional Peskin – McQueen model of blood flow through the heart. The motivation for this simulation was twofold: to help clinicians correlate results generated by this computer model with their clinical Doppler data, and to offer fluid dynamical explanations for certain color Doppler observations. Three clinical situations have been simulated to date, images of the normal mitral valve, Starr-Edwards prosthetic valve in the mitral position, and images of a heart characterized by 'ischemic mitral insufficiency', here a result of stiff chordae and papillary muscle. The simulated images are similar to those seen in clinical color Doppler examinations. In addition, certain details are visible using this simulation technique that are often difficult to see in clinical Doppler studies. Advantages of this method include finer spatial and temporal resolution than is typically available using clinical instruments enabling the visualization of flow patterns that are less evident clinically, as well as full control over all imaging parameters. A study is planned to compare clinical and model Doppler images in various mitral valve pathologies using the expanded Peskin – McQueen model in order to extend the simulation beyond diastole and early systole to include the complete cardiac cycle.

Introduction

Peskin, together with McQueen, have developed a computational technique to simulate blood flow and valve motion in the left side of the heart, and have used this model to study various aspects of mitral valve physiology and pathophysiology [1,2,3,4,5,6]. Flow patterns generated with this method have been displayed as plots of stream functions, pressure contours, and fluid marker videos. These displays are sometimes difficult to interpret by clinicians who are not well-versed in fluid dynamics, and cannot be compared directly to clinically-generated data. Because of the widespread clinical use of color Doppler ultrasound to examine blood flow patterns within the heart, a color Doppler ultrasound analogue generated during a cardiac simulation could improve the clinician's understanding of what this computer model can accomplish.

Such a simulation may be beneficial for another reason. Color Doppler ultrasound is a relatively new technique, where some of the data obtained has been difficult to interpret. For example, questions remain concerning how these images can be used to quantify *volumes* of regurgitant jets, since the data displayed are *velocities.* Although many studies have used in-vitro chamber models to investigate some of the factors that influence the appearance of such regurgitant jets [7,8,9,10], a color Doppler simulation generated by the computer model also may help provide a better understanding of principles such as volume quantification.

For these reasons, a computer-simulated color Doppler ultrasound analogue has been developed which models as closedly as possible those instruments currently in clinical used. This simulated Doppler display modality complements the other computer-generated display methods that have been used previously without changing the basic computational procedure.

Methods

The computational method used to solve for the flow patterns and valve motion have been described previously [1,2,3,4]. Only those parts of the method important for understanding how these simulated Doppler images are generated will be described here.

The model is a two-dimensional representation of the left side of the heart; it includes the atrium, ventricle, mitral valve, and left ventricular outflow tract but does not in its present form contain an aortic valve or aorta. As such, this model can only be used to look at diastole and early systole, until the time when the aortic valve would normally open. however, this is the period of interest when examining the fluid mechanics of the mitral valve.

Heart walls and valves are represented as approximately 300 boundary points. The heart wall boundary points are connected by links that have the properties of Hill's three component muscle model, including both active and passive components. The natural mitral valve is modeled as two asymmetric thin flexible leaflets. Chordae tendineae and papillary muscles, though outside the computational plane, are included as structures that generate forces on the leaflets and ventricular walls without obstructing intraventricular flow (although clinically they would have an effect on flow patterns.)

The heart is immersed in a fluid-filled box of constant density, equal to the density of the blood and the heart wall. Because this fluid is viscous, motion of the heart walls and valves determines the patterns of fluid flow, and vice versa. This is the so-called 'no slip condition' of fluid mechanics. Heart muscle and valve characteristics are incorporated as extra forces that act on the fluid. This technique, which has been termed the immersed boundary method, makes it possible to solve the Navier-Stokes equations for incompressible flow to determine the velocity of blood flow everywhere within the heart. The computed

blood velocity then moves the heart walls and valves.

The fluid-filled box in which the heart is immersed is divided into a fluid mesh with 64 meshpoints per side. For computational reasons, all lengths and times have been reduced by a factor of 25, which also reduces the Reynold's number to a subphysiological level. However, evidence has been presented previously that this scaling does not significantly affect the flow patterns generated by the computational method [3]. One computational "heart beat" entails solving these equations for the two components of the velocity (x and y, in two dimensions) at each of the 64 X 64 fluid mesh points for each of the 640 time steps that together comprise the period of diastole through early systole modeled here. It is this 'velocity mesh' that serves as the basis for the simulated color Doppler images. However, the desired Doppler resolution may be different than this 64 X 64 computational mesh resolution. In order to simulate the same pixel size as clinical Doppler machines use, the computed velocity mesh can be spread onto a coarser mesh or interpolated onto a finer mesh using the same weighting (delta) functions as are used to spread and interpolate quantities between fluid and boundary points. The resolution of this Doppler grid is therefore variable, and can simulate different resolutions of those instruments used clinically.

Clinical color Doppler images are comprised of a 2-D echocardiographic outline of the heart walls and valve together with the color representation of the flow velocities inside the heart. Because the model heart is immersed in a large fluid-filled box, some of the fluid grid points where velocity is computed lie outside the heart, some correspond to the heart wall or valves, and some are those desired points inside the heart. One step in this simulation of color Doppler images is therefore to determine which fluid mesh points fall into which of these three categories: only those points that represent heart wall or valve, together with those inside the heart, will be included in the simulated Doppler images.

As in a clinical Doppler examination, one must decide where the ultrasound probe (transducer) is to be placed with respect to the heart. Such positions are typically apical (on the chest wall at a point overlying the cardiac apex), suprasternal (above the sternal notch), parasternal (on the side of the sternum), and subcostal (below the rib margin). Each position transects the heart in a different plane, thereby producing images that include different cardiac structures and flow patterns. Ideally, its beam should be directed parallel to the direction of blood flow since the measured velocity is a function of the cosine of the angle between the transducer plane and the fluid jet. The location of the 'transducer' used to generate the simulated color Doppler images similarly can be varied to model these different orientations. For the present study, the transducer was located in a standard apical position; this transducer is stationary while the heart contracts, as in an actual Doppler examination. Since the model is two-dimensional however, the simulated transducer cannot be moved in the plane perpendicular to the computational grid.

In the simulation, once the two velocity components of the points inside the heart have been determined on the Doppler grid, the velocity component parallel to the line connecting each grid point and the Doppler transducer is computed. This is the 'Doppler velocity' at each point. A positive velocity means blood is moving towards the transducer, while a negative velocity means blood is moving away. Files containing this velocity information for each Doppler grid point, including which grid points correspond to the heart wall or valves, are output at each time step that Doppler information is desired. A typical Doppler device displays images at a rate of 30 images per second, or one image approximately every 33 msec. This rate can be simulated by computing Doppler velocities at every 45 timesteps, or refine this clinical temporal resolution by computing the Doppler velocity information more frequently. These data files then are transferred from the computer where

the actual computer simulation has been performed (a Cray supercomputer) to a local graphics workstation for generation of the color display.

A graphics program is used to generate the desired color Doppler images from the velocity data files. The images can be looked at individually, or linked together to create a videotape that runs at the same speed as a true color Doppler video.

Various parameters can be adjusted in this color Doppler simulation, both to represent different Doppler devices, or to simulate changing the controls available on one particular device. These adjustable parameters include the Doppler probe position (as described above), the color scale, and the instrumental gain.

Doppler devices code the velocity's magnitude and direction by assigning shades of red and blue. By convention, red typically represents blood flow toward the transducer (positive Doppler velocity), while blue represents flow away from the transducer. As the magnitude of the velocity increases, the color grows brighter. Black represents no flow (or flow perpendicular to the transducer, which would be measured as no flow since the cosine of the angle between this flow and the Doppler probe is zero). Eight different shades for each color are typically employed, with maximum and minimum velocities for each level assigned internally. An "enhanced" color scheme is often used: shades of yellow augment the shades of red, while deeper blue represents higher velocity flow away from the transducer. This enhancement is technically produced by adding shades of green to the red and blue [11]. Heart walls and valves (the 2-D echocardiographic data) are shown in white.

These color conventions have been followed for the computer-generated color Doppler images. One advantage of the simulation is that the color scheme can be varied to match that used by a particular instrument, since different instruments typically use different color schemes. An enhanced color scheme has been modeled here.

Another characteristic of clinical color Doppler images is the presence of 'aliasing' if the magnitude of the velocity exceeds a certain positive or negative limit known as the Nyquist limit. This limit is a function of the pulse repetition frequency used by the ultrasonic transducer. When a velocity exceeds the positive limit, the encoded color suddenly flips from very bright red (or yellow, if an enhanced color scheme has been used) to very bright blue (or cyan). The opposite occurs if the velocity is more negative than the lower Nyquist limit, and the color flips from blue to red or yellow. The simulated color Doppler images include aliasing.

Clinical Doppler instruments have a variable gain control that works as a filter to allow optimal output of velocity information with minimal noise (noise being interference caused by low-frequency signals due to such things as heart wall motion). This feature also has been incorporated into the simulation procedure. Another feature that has been duplicated is the ability to displace the zero-velocity baseline if one wishes to examine more accurately either highly positive or negative velocity jets.

Some Doppler devices also add differing amounts of green to their color schemes in order to represent 'turbulent' blood flow, thereby again producing shades of yellow and cyan. This is typically accomplished by comparing the velocities inside a sample volume: if the variance (spectral broadening) of these velocities is above a certain limit, flow inside the sample volume is defined as 'turbulent' and green is added to that pixel. However, as explained by Gardin and Lobodzinski, most machines add green to velocities that are below the velocity thresholds where turbulent flow would typically be seen. Also, there is no standardization between instruments as to how this algorithm is performed, nor to the amount of green added [11]. Although the Peskin – McQueen computational cardiac model does not actually generate turbulent flows (the Navier-Stokes equations used are only valid for non-turbulent

flows and the Reynold's number is sub-physiologic), an artificial turbulence parameter based on velocity variance within a sample volume can also be included in the color Doppler simulation. This has not been included to date, however, since it only makes computational sense if the simulated Doppler sample volume is larger than the grid spacing used in the model.

Results

Color Doppler Simulation of Flow Patterns with a Normal Mitral Valve

The color Doppler simulation of normal diastolic and early systolic flow patterns resembles what is seen during clinical Doppler examination of the normal heart. One can see a red jet of fluid entering the ventricle through the mitral valve during early diastole; this jet is red because the blood is flowing toward the apical transducer. The blood velocity increases (the colors become orange and even yellow) as diastole continues. The jet reaches the heart apex and then blood seems to 'sweep up' the ventricular walls; this is seen as blue flow along the walls. Blood continues to flow into the outflow tract toward the aorta and away from the transducer (and therefore appears blue) as systole begins. The Doppler simulation ends at this point, since there is no aortic valve for the blood to be ejected through. These same color Doppler patterns have been seen clinically [12]. There also seemed to be a small amount of velocity increase on the proximal side of the mitral valve. This proximal flow acceleration has recently been suggested as a method to quantitate flow given velocity information [17,18].

During diastole, one can also see vortices forming behind the mitral valve leaflets. These vortices continue as blood flowing up from the apex sweeps down the ventricular side of the mitral valve leaflets toward the apex and transducer. This explains the shades of red seen on the ventricular side of the mitral valve leaflets. In clinical Doppler examinations vortices are seldom seen, although there have been reports of eddies seen at the apex that subsequently proceed up the ventricular walls. This observation has been reported more commonly in cases of dilated cardiomyopathy, where it has been attributed to an abnormal alignment of the anterior mitral leaflet with the ventricular septum, thereby directing the flow toward the posterior ventricular wall. [13,14,15]

Diastolic Color Doppler Flow Patterns with a Starr-Edwards Mitral Prosthesis:

When a Starr-Edwards (ball-in-cage) prosthetic valve was modeled in the mitral position, the simulated color Doppler images produced were again similar to what has been reported clinically [16]. There were now two separate mitral inflow jets on either side of the prosthetic valve, seen as red diastolic flow patterns. Valve closure is accompanied by a small spurt of mitral regurgitation (blue flow into the atrium) at the conclusion of the simulation. Note that one can also see flow within the ball of the valve itself. This is a consequence of the mathematical method, which models the ball as neutrally buoyant fluid.

Flow Patterns In a Model of Ischemic Mitral Insufficiency

As a third example of the simulation technique, a model of ischemic mitral insufficiency (otherwise known as papillary muscle dysfunction) was created by increasing the stiffness of the links that represent the mitral valve leaflets, chordae tendineae, and papillary muscle. This condition often occurs following a myocardial infarction when a portion of the left ventricle and/or papillary muscle becomes dysfunctional, leading to poor ventricular wall motion and mitral annular dilatation. The annular dilatation and apical wall motion abnormality in turn may lead to mitral regurgitation (insufficiency).

One can see the wall motion abnormality in the simulation of ischemic mitral insufficiency, as well as the early-systolic regurgitation (as blue flow into the atrium upon ventricular contraction) that is characteristic of this condition. These results are qualitatively similar to color Doppler images seen clinically [19].

Discussion

As previous comparisons between the data generated by this computer cardiac model and data from clinical experiments have shown good correlation [3,4], it was hoped that these simulated color Doppler images (which represent the same computer-generated data displayed in a different form) also would correlate well with clinical color Doppler images. It was therefore reassuring that the major characteristics of the simulated Doppler images did agree with those images generated clinically, despite the limitations inherent in this modeling technique. This was true for all three of the simulations described above.

There was, however, one important difference between clinical Doppler images and this Doppler simulation. This was the prominent part played by vortices in the simulated Doppler images, as opposed to usually not being seen clinically: in clinical Doppler images, the area directly behind the mitral valve typically appears black during diastole in most clinical images. The existence of such vortices has been shown experimentally in sheep and dog ventricles by Taylor and Wade [20], as well as in the model ventricles of Bellhouse et. al. [21]. What are some possible reasons why these vortices are therefore not usually seen in clinical color Doppler examinations?

One reason for this difference may be the two-dimensional nature of this computer model. Vortices may not occur clinically within the single plane that is represented in this model. However, if a clinical probe were angulated differently (or moved to a non-standard location), it is possible that one might intersect a plane that does contain vortices. This may be the reason why vortices are more commonly noted in the case of dilated cardiomyopathy [13,14,15]. This dilation may change the relative geometry between mitral valve leaflets and the ventricular walls in such a way that vortices are seen in a particular plane interrogated by the Doppler ultrasound beam. The three-dimensional cardiac model now being developed

by Peskin and McQueen offers a way to explore this possibility in a controlled setting.

There are three other possible explanations for this disparity. First, the sample volume in clinical Doppler images is larger than has been used in these simulations. This may cause vortex velocities on one side of a vortex to be averaged with those on the other side, resulting in a very low velocity signal. This will be tested in the future by increasing the sample volume of the color Doppler simulation to match what has been seen clinically.

A second explanation for the unusual vortex prominence is that there is not enough blood within the vortex itself to generate a visible Doppler pattern, since this pattern is a function of the number of 'reflectors' the ultrasound beam intercepts. This seems less likely, since the concentration of blood through the ventricle is relatively constant.

Lastly, the velocity of the vortex core may be lower than the velocity threshold of Doppler instruments. Although this too is unlikely since the vortex core velocity is *greater* than the velocity of the surrounding fluid, one could easily test this mechanism by decreasing the instrument's gain setting to see if vortices can be produced. Alternately, the simulated gain setting could be increased to see if the vortices disappear.

Despite the differences and the qualitative nature of any comparisons, it is likely that this simulated Dopppler technique can be useful to study the changes in color Doppler images that are produced when one changes different valve or heart wall parameters.

Conclusions

Simulated color Doppler images have been generated using the two-dimension computer model of blood flow through the heart developed by Peskin and McQueen. The images produced during the simulation of the three different mitral valvular conditions presented above are qualitatively similar to the color Doppler images observed clinically, although it has not yet been determined why the prominent vortices seen behind the mitral valve leaflet are often not seen clinically.

This method now can be used to study the color Doppler images that may be expected with many different clinical situations by varying a single parameter and determining the effect this change has on the color Doppler images produced. The recent expansion of the computer model to include systole will enable even better comparisons between experimental and clinical data, as blood flow through the complete cardiac cycle can be examined. Despite the qualitative nature of any comparisons due to the limitations of this (or any) computational method, this computer simulation tool offers a unique opportunity to study the fluid mechanisms and assumptions which underlie the color Doppler images obtained clinically. This technique also will aid those familiar with the Peskin – McQueen computer model in analyzing the data generated by the model from a more clinically relevant perspective.

References

[1] Peskin CS. Flow patterns around heart valves: a numerical method. J Comput Phys 10:252-271, 1972.

[2] Peskin CS. Numerical analysis of blood flow in the heart. J Comput Phys 25:220-252, 1977.

[3] McQueen DM, Peskin CS, Yellin EL. Fluid dynamics of the mitral valve: physiological aspects of a mathematical model. Am J Physiol 242 (Heart Circ Physiol 11):H1095-1110, 1982.

[4] Meisner JS, McQueen DM, Ishida Y, Vetter HO, et. al. Effects of timing of atrial systole on LV filling and mitral valve closure: computer and dog studies. Am J Physiol 249 (Heart Circ Physiol 18):H604-619, 1985.

[5] Peskin CS, McQueen DM. Modeling prosthetic heart valves for numerical analysis of blood flow in the heart. J Comput Phys 37:113-132, 1977.

[6] McQueen DM, Peskin CS. Computer-assisted design of pivoting disc prosthetic mital valves. J Thorac Cardiovasc Surg 86:126-135, 1983.

[7] Bolger AF, Eigler NL, Pfaff JM, Resser KJ, Maurer GM. Computer analysis of Doppler color flow mapping images for quantitative assessment of in vitro fluid jets. J Am Coll Cardiol 12:450-457, 1988.

[8] Bolger AF, Eigler NL, Maurer G. Quantifying valvular regurgitation. Limitations and inherent assumptions of Doppler techniques. Circ 78:1316-1318, 1988.

[9] Sahn DJ. Instrumentation and physical factors related to visualization of stenotic and regurgitant jets by Doppler color flow mapping. J Am Coll Cardiol 12:1354-1365, 1988.

[10] Maciel B, Loises VA, Shandas R, et. al. Effects of pressure and volume of the receiving chamber on the spatial distribution of regurgitant jets as imaged by color Doppler flow mapping. An in vitro study. Circ 83:605-613, 1991.

[11] Gardin JM, Lobodzinski SM. Do Doppler color flow algorithms for mapping disturbed flow make sense? J Am Soc Echo 3:310-315, 1990.

[12] Kisslo J, Adams DB, Belkin RN, Flow patterns in the normal heart. In: Doppler Color Flow Imaging. (1988) Churchill Livingstone, NY, 76.

[13] Abinader EG, Kuo LC, Rokey R, Quinones MA. Mitral angles: a new two–dimensional echocardiographic index of left ventricular performance. Am Heart J 110:381-385, 1985.

[14] Delmarre BJ, Bot H, Visser CA, Dunning AJ. Pulsed Doppler echocardiographic description of a circular flow pattern in spontaneous left ventricular constrast. J Am Soc Echo 1:114-118, 1988.

[15] Jacobs LE, Kotler MN, Parry WR. Flow patterns in dilated cardiomyopathy: a pulsed-wave and color flow Doppler study. J Am Soc Echo 3:294-302, 1990.

[16] Jones M Eidbo EE. Doppler color flow evaluation of prosthetic mitral valves: experimental epicardial studies. J Am Coll Cardiol 13:234-240, 1989.

[17] Bargiggia G, Recusani F, Yoganathan AP, et. al. Color flow Doppler quantitation of regurgitant flow rate using the flow convergence region proximal to the orifice of a regurgitant jet (abstract). Circ 78(suppl II):II-609, 1988.

[18] Baumgartner H, Schima H, Kuhn P. Value and limitations of proximal jet dimensions for the quantitation of valvular regurgitation: an in vitro study using Doppler flow imaging. J Amer Soc Echocard 4:57-66, 1991.

[19] Zachariah ZP, Hsiung MC, Nanda NC, Kan MN, Gatewood RP, Jr. Color Doppler assessment of mitral regurgitation induced by supine exercise in patients with coronary artery disease. Am J Cardiol 59:1266-1270, 1987.

[20] Taylor DEM, Wade JD. Pattern of blood flow within the heart: a stable system. Cardiovasc Rex 7:14-21, 1973.

[21] Bellhouse BJ. Fluid mechanics of heart valves. In: Bergel DH, ed. Cardiovascular Fluid Dynamics, Vol. 1. (1972) Academic Press, NY, 261-286.

Chapter 6. Discussion and Conclusions

The study of blood flow through the heart has been a subject of great interest ever since DaVinci described the formation of vortices in the aortic sinuses almost five hundred years ago [1]. Despite the time that has elapsed since then, there remain many questions regarding cardiac blood flow that have not yet been satisfactorily answered. One reason for this uncertainty is the difficulty inherent in examining blood flow in-vivo: a single intervention may lead to multiple cardiac physiological responses. Any observed change in blood flow may be a result of the responses, not the intervention itself. Thus, cause and effect are difficult, if not impossible, to differentiate.

Another problem with in-vivo studies is their often invasive nature. Experiments are at times conducted on open-chested animals; this method may unpredictably alter the observed results. The introduction of measurement devices (such as electromagnetic flow meters) may in themselves change cardiac dynamics [53]. Additionally, invasive in-vivo studies are very difficult to perform on humans: animal studies are quite helpful, but cannot be extrapolated directly to human cardiac physiology.

There has been much progress made recently in the non-invasive examination of human cardiac blood flow through the use of two-dimensional and pulsed-Doppler echocardiography (and pulsed-Doppler's variant, color Doppler echocardiography). Although there has been an explosion of literature using Doppler techniques to explore cardiac physiology and pathophysiology, there are many limitations of these techniques which are often not considered [29,122,123,124,125].

Computer modeling provides a unique tool to study cardiac physiology and pathophysiology in a more controlled setting by breaking down heart function into its most essential components. One then can examine how a change in a particular parameters affects this

heart function without having to worry about confounding reflex responses. In this way, cause and effect are much easier to elucidate.

One type of computer heart model that has been developed is a lumped-parameter model where the heart is treated as a "black box" with certain characteristics. Parameters are input, processed inside this black box, and resultant cardiac flow patterns emerge. An analog lumped-parameter cardiac model developed by Meisner has been used successfully to study certain aspects of mitral valve function, including the existence of a particular PR interval between atrial and ventricular contraction that optimizes transmitral flow [6], and the effects of decreased ventricular compliance [35] and mitral stenosis [70] on diastolic ventricular filling. Thomas and Weyman have used a similar lumped-parameter computer model to explore the effects of changes in chamber compliance and in crude mitral valve morphology on diastolic cardiac flow [71,73]. These lumped parameter models are useful in their simplicity, but do not allow one to study the actual flow patterns or changes in heart configuration.

Peskin developed a different type of computer model based on a technique known as the immersed boundary method [2,3,5]. By treating the heart as if it were floating within a fluid-filled box and modeling the heart walls and valves as boundary points (connected by links) which move in the fluid and impart forces to the fluid, he was able to use the Navier-Stokes equation for steady flow to actually *look at* the intracardiac blood flow patterns and heart configuration changes. This model had been used previously by Peskin and McQueen to explore a number of different aspects of cardiac function, including normal mitral valve function [5], effects of changes in the PR interval [6], and the optimization of prosthetic mitral valve design [58,59,60]. However, as the model only included a mitral valve, it use was restricted to studying diastolic and early systolic cardiac function. The model also was

not constructed to most accurately represent normal human cardiac geometry.

This dissertation has described the expansion of the two-dimensional Peskin – McQueen cardiac model to enable it to explore cardiac function in health and disease *throughout* the cardiac cycle. We also have corrected some other limitations of the original model. Most of these changes were discussed in Chapter 2. First, an aortic valve and complete aortic structure has been added to allow for blood to be ejected from the heart. The aorta has been tethered in place by linking the aortic boundary points to fixed points in space, thus simulating normal aortic connective tissue and vessel attachments. In order to model aortic outflow, we have generalized the source/sink procedure such that we nw can include any number of sources and sinks. This will make it possible to model multiple pulmonary venous sources into the atrium and arterial branching from the aorta. If the size of the aortic sinuses in comparison to the grid resolution can be increased, it also may be possible to model coronary arterial flow.

The initial geometry of the computational heart chamber has been modified to more accurately reflect human cardiac dimensions, although it is not this exact geometry to which the heart returns at the end of a computed cardiac cycle. This geometric difference between initial and final heart configuration has allowed us to study how changes in chamber volumes might affect the flow of blood through the heart. We now plan to further modify the computer method in order to even more accurately simulate steady-state cardiac geometry, either by implicitly finding the initial geometry *such that* steady-state geometry is correct, or by changing other parameters which control cardiac geometry, such as activation and pressure parameters.

Other methodological changes were necessary to enable the above modifications. The size of the heart and the computational domain has been expanded, with a secondary result

being an increase in the Reynold's number by a factor of four, although this Reynold's number is still subphysiologic due to an artificial length and time scaling factor needed for computational reasons. We now plan to incorporate a recently-introduced second-order accurate technique to solve the Navier-Stokes equations [126] in place of Chorin's projection method that has been used to date. This should enable us to increase the Reynold's number into the physiological range, and even possibly allow us to model the effects of exercise (where the Reynold's number is increased) on cardiac function. This new fluid solver also will allow us to study how the lower Reynold's number of the present model affects the computed results, although it has been shown that even with the lower number inertial effects still dominate [5].

Another modification of the Peskin – McQueen model has been the incorporation of a new divergence method based on the scheme used to interpolate quantities between the fluid grid points and the boundary points which comprise the heart walls, aorta, and valve structures. This contrasts with the simple centered-difference divergence technique used previously. This modification has been described in Chapter 3. The reason for the change was the observation that the heart was numerically "leaky", losing volume at a rate proportional to the pressure difference across the heart walls. With the lower pressures of diastole, this leak was not significant. However, when pressures increased during systole as much as one third of the ventricular volume was lost through this numerical leak. The introduction of the new divergence method, which enters the calculations only during the final stages of Chorin's projection method used to solve the Navier-Stokes equations, virtually eliminates this volume loss. Indeed, we have shown in Chapter 2 that the volume loss of the expanded cardiac model was less than one percent over one complete cardiac cycle.

As we are now able to continue the computation over more than one heartbeat, we can simulate steady-state conditions and eliminate any possibility that computed results were due to initial flow transients. This improvement also allows us to explore acute changes in cardiac parameters in a more controlled manner. One 'normal' beat can be modeled and then a parameter can be changed at the beginning of the next heart beat. It is no longer is it necessary to start from the first timestep where blood flow is artificially zero.

The true test of any cardiac model is its ability to simulate heart function. We have used both the expanded model and an earlier version of the model (where the new cardiac geometry had not been incorporated although the heart was able to eject blood during systole) to explore how this model behaves in a number of different clinical situations.

Results generated by the expanded model have been included in Chapter 2. We have shown that the model produces transvalvular flows which are qualitatively quite similar to measurements obtained clinically. Even the recently-described mid-diastolic transmitral flow peak ('L-wave') can be seen, together with multiple diastolic atrial - ventricular pressure crossovers which have been reported clinically [54]. These details were not seen in the initial Peskin – McQueen model, perhaps because the change in geometry resulted in a different degree of relative mitral stenosis produced by the mitral valve itself, or because the ventricular stiffness has been increased producing a stiffer ventricle. Both of these factors have been shown by others to produce more prominent mid-diastolic flow [35,53]. The transaortic flow is also qualitatively similar to flow through the human aorta, but aortic sinus vortices have not been seen. This may be due to the relatively small size of these sinuses compared to the computational grid, a result of the lower Reynold's number described above, or a consequence of the two-dimensional nature of this model. Despite the lack of vortices the aortic valve closes competently, albeit slightly later and with perhaps

more regurgitation than normally occurs clinically. Since more backflow is seen at the level of the aortic valve ring upon aortic closure than is seen between the leaflet tips, most of this backflow can be attributed to the leaflets displacing fluid as they move toward the left ventricle, and therefore does not represent true regurgitation. This was also true at the mitral valve, as has been previously reported by Peskin et. al. [2,4,5,6].

Peak systolic aortic and ventricular pressures are still lower than they should be, although peak systolic ventricular pressure has been increased by a factor of two versus that obtained using the original Peskin – McQueen model. We now hope to increase these peak pressures by increasing ventricular activation, increasing the 'charging pressure' of the aorta, and substituting a more accurate form for the aortic sink, such as a Windkessel model.

Another example of the advantages of using a computer simulation technique to study cardiac physiology and pathophysiology has been shown in Chapter 4: computer models make it possible to systematically explore the effects of changes in a particular parameter in a way not possible with either clinical or animal studies. In this series of experiments designed to study the effects of changes in mitral apparatus geometry on transmitral flow and leaflet motion, a preliminary form of the expanded model has been used. This form of the model included an aortic sink and the new form for the divergence, but did not include any of the other modification that have been described in this dissertation. Despite these limitation, this study has provided a conceptual framework for how changes in the geometry of the mitral valve leaflets, chordae, and papillary muscle can produce significant changes in transmitral flow characteristics and cardiac function. In particular, we were able to demonstrate that non-regurgitant displaced volume backflow, true mitral regurgitation, and mitral leaflet prolapse are all dependent on the precise geometry of all mitral apparatus structures. We also have shown that diastolic transmitral flow can be significantly altered

solely by changing these geometric parameters. These results offer a unique view of the complex interaction between cardiac structures and function. We now plan to perform this same study using the expanded cardiac model.

Finally, we have produced a new method of displaying our computed results which simulates images obtained via color Doppler ultrasound. This new display modality makes it possible for clinicians not well-versed in other fluid dynamical displays, such as streamlines or pressure contours, to be able to interpret data generated by our model. This simulation tool might also help to explain some of the limitations of color Doppler ultrasound [29,122,123,124,125].

Although limitations still remain, especially those due to the two-dimensional nature of this model, this expanded cardiac model now can be used to explore an almost limitless number of physiological and pathophysiological situations in a manner not possible clinically. These possibilities in studying aortic valve in a similar manner to prior computer experiments concerning the mitral valve, looking at the effect one valve has upon the other, exploring how changes in diastolic heart function can alter systolic heart function, and simulating increases in preload and afterload, among others. Peskin and McQueen are now in the process of developing a full three-dimensional cardiac model that also includes the right heart [112,113]. This three-dimensional model will be much more computationally expensive to use, however, compared to the two-dimensional model. It is therefore our intention to use the expanded two-dimensional model to explore a wide range of different clinical problems. Once we have found a particularly interesting result, we can simulate that condition using the three-dimensional model. In this way, we hope to help answer those questions that still remain about the mechanisms of valve motion and blood flow during the complete cardiac cycle.

Bibliography

[1] O'Malley and Sanders, Leonardo da Vinci on the Human Body, 2nd Ed. Henry Schuman Inc., NY (1982), p. 266.

[2] Peskin CS. Flow patterns around heart valves: a digital computer method for solving the equations of motion. Ph.D. thesis, Albert Einstein College of Medicine, NY, 1972.

[3] Peskin CS. Numerical analysis of blood flow in the heart. J Comput Phys 25:220-52, 1977.

[4] Yellin EL, Peskin CS, et. al. Mechanics of mitral valve motion during diastole. Am J Physiol 241 (Heart Circ Physiol): H389-400, 1981.

[5] McQueen DM, Peskin CS, Yellin EL. Fluid dynamics of the mitral valve: physiological aspects of a mathematical model. Am J Physiol 242 (Heart Circ Physiol):H1095-1110, 1982.

[6] Meisner JS, McQueen DM, et. al. Effects of timing of atrial systole on left ventricular filling and mitral valve closure: computer and dog studies. Am J Physiol 249 (Heart Circ Physiol):H604-619, 1985.

[7] Kostucki W, Vandenbossche JL, Friart A, Englert M. Pulsed Doppler regurgitant flow patterns of normal valves. Am J Cardiol:58:309-313, 1986. 58:309-313.

[8] Yoshida K, Yoshikawa J, Shakudo M, et. al. Color Doppler evaluation of valvular regurgitation in normal subjects. Circ 78:840-847, 1988.

[9] Panidis IP, McAllister M, Ross J, Mintz GS. Prevalence and severity of mitral regurgitation in the mitral valve prolapse syndrome: a Doppler echocardiographic study of 80 patients. J Am Coll Cardiol 7:975-981, 1986.

[10] Akasaka T, Yoshiwara J, Yoshida K, Yamaura Y, Hozumi T. Temporal resolution of mitral regurgitation in patients with mitral valve prolapse: a phonocardiographic and Doppler echocardiographic study. J Am Coll Cardiol 13:1053-1061, 1989.

[11] Grayburn PA, Berk MR, Spain MG, Harrison MR, Smith MD, DeMaria AN. Relation of echocardiographic morphology of the mitral apparatus to mitral regurgitation in mitral valve prolapse: Assessment by Doppler color flow imaging. Am Heart H J 119:1095-1102, 1990.

[12] Laniado S, Yellin EL, et.al. Physiological mechanisms in aortic insufficiency: I. The effect of changing heart rate on flow dynamics. II. Determinants of Austin-Flint murmur. Circ 66: 226-35, 1982.

[13] Fortuin NJ, Craige E. On the mechanism of the Austin Flint murmur. Circ 45: 558-570, 1972.

[14] Louie EK, Mason TJ, et. al. Determinants of anterior mitral leaflet fluttering in pure aortic regurgitation from pulsed Doppler study of the early diastolic interaction between the regurgitant jet and mitral inflow. Am J Cardiol 61:1085-1091, 1988.

[15] Harvey W. Anatomical Studies on the Motion of the Heart and Blood, 5th ed. Translated by Chauncey D. Leake. Charles C. Thomas Inc., Ill (1970), p. 49.

[16] Bergel DH, ed. Cardiovascular Fluid Dynamics, Vol. 1. Academic Press, NY (1972), p. 5.

[17] Henderson Y, Johnson FE. Two modes of closure of the heart valves. Heart 4: 69-82, 1912.

[18] Little RC. The mechanism of closure of the mitral valve: a continuing controversy. Circ 59:615-618, 1979.

[19] Peskin CS. The fluid dynamics of heart valves: experimental, theoretical and computational methods. Ann Rev Fluid Mech 14:235-259, 1982.

[20] Mills CJ. Measurement of pulsatile flow and flow velocities. 2. The electromagnetic flowmeter. In: Bergel DH, ed. Cardiovascular Fluid Dynamics, Vol I. Academic Press, NY (1972), pp. 53-70.

[21] Reneman RS. The use of electomagnetic flow probes in the mitral position - principles, advantages, and limitations. In: Kalmanson D, ed. The Mitral Valve. A Pluridisciplinary Approach (1976), pp. 117-125.

[22] Hatle L, Angelsen B. Doppler Ultrasound in Cardiology. Lea and Febiger, Philadelphia (1981).

[23] Switzer DF, Nanda NC. Limitations of pulsed and continuous-wave Doppler echocardiography. Echocardiography: A Rev of Cardiovasc Ultras 2:207, 1985.

[24] Dang TY, Gardin JM, et. al. Refining the criteria for pulsed-Doppler diagnosis of mitral regurgitation by comparison with left ventricular angiography. Am J Cardiol 60:663-666, 1987.

[25] Kisslo J, Adams DB, Belkin RN. Doppler Color Flow Imaging. Churchill Livingstone, NY (1988).

[26] Yoganathan AP, Reamer HH, et. al. Laser-Dopper anemometer to study velocity fields in the vicinity of prosthetic heart valves. Med Biol Engin and Comput 17:38, 1979.

[27] Yoganathan AP, Chaux A, et. al. Bileaflet, tilting disc and porcine aortic valve substitutes: in vitro hydrodynamic characteristics. J Amer Coll Cardiol 3:313, 1984.

[28] Stewart WJ, Jiang L, et. al. Variable effects of changes in flow rate through the aortic, pulmonary and mitral valves on valve area and flow velocity: impact on quantitative Doppler flow calculations. J Amer Coll Cardiol 6:653-662, 1985.

[29] Bolger AF, Eigler NL, Pfaff JM, Resser KJ, Maurer GM. Computer analysis of Doppler color flow mapping images for quantitative assessment of in vitro fluid jets. J Am Coll Cardiol 12:450-457, 1988.

[30] Feigenbaum H. Echocardiography, 3rd Edition. Lea and Febinger, Philadelphia (1981).

[31] Gorlin R, Gorlin SJ. Hydraulic formula for calculation of the area of the stenotic mitral valve, other cardiac valves, and central circulatory shunts. Am Heart J 41:1-29, 1951.

[32] Thomas JD, Weyman AE. Doppler mitral pressure half-time: a clinical tool in search of theoretical justification. J Amer Coll Cardiol 10:923-929, 1987.

[33] Bellhouse BJ. Fluid Mechanics of heart valves. In: Bergel DH, ed. Cardiovascular Fluid Dynamics, Vol 1. Academic Press, NY (1972), pp. 261-286.

[34] Schnittger I, Appleton CP, et. al. Diastolic mitral and tricuspid regurgitation by Doppler echocardiography in patients with atrioventricular block: new insight into the mechanism of AV valve closure. J Am Coll. Cardiol 11:83-88, 1988.

[35] Yellin EL, Nikolic S, Frater WM. Left ventricular filling dynamics and diastolic function. Prog Cardiov Dis 32:247-271, 1990.

[36] Bellhouse BJ. Fluid mechanics of a model mitral valve and left ventricle. Cardiovasc Res 6:199-210, 1972.

[37] Bellhouse BJ. Fluid Mechanics of a Model Mitral Valve. In: Kalmanson D, ed. The Mitral Valve: A Pluridisciplinary Approach. Publishing Sciences Group, Mass (1976), pp. 99-110.

[38] Lee CS, Talbot L. A fluid-mechanical study of the closure of heart valve. J Fluid Mech 91:41-63, 1979.

[39] Brockman SK. Mechanism of the movement of the atrio-ventricular valves. Am J Cardiol 17:682-690, 1966.

[40] Taylor DEM, Wade JD. Pattern of blood flow within the heart: a stable system. Cardiovasc Res 7:14-21, 1973.

[41] Laniado S, Yellin EL, et. al. Temporal relation of the first heart sound to closure of the mitral valve. Circ 47:1006-1014, 1973.

[42] Laniado S, Yellin EL, et. al. A study of the dynamic relation between the mitral valve echogram and phasic mitral flow. Circ 51: 104-113, 1975.

[43] Tsakiris AG, Gordon DA, et. al. Motion of both mitral valve leaflets: A cineroentgenographic study in intact dogs. J Appl Physiol 39:59-66, 1975.

[44] Tsakiris AG, Gordon DA, et. al. Relation of mitral valve opening and closure to left atrial and ventricular pressures in the intact dog. Am J Physio (Heart Circ Physiol) 234:H146-151, 1978.

[45] Karas S, Elkins RC. Mechanism of function of the mitral valve leaflets, chordae tendineae and left ventricular papillary muscles in dogs. Circ Res 26:689-696, 1970.

[46] Marzilli M, Sabbah HN, et. al. Role of the papillary muscle in opening and closure of the mitral valve. Am J Physiol (Heart Circ Physiol) 238:H348-354, 1980.

[47] Tsakiris AG, von Bernuth G, et. al. Size and motion of the mitral valve annulus in anesthetized intact dogs. J Appl Physiol 30:611-618, 1971.

[48] Perloff JK, Roberts WD. The mitral apparatus. Functional anatomy of mitral regurgitation. Circ 46:227-239, 1972.

[49] Sonnenblick EH, Napolitano LM, et. al. An intrinsic neuromuscular basis for mitral valve motion in the dog. Circ Res 21:9-15, 1967.

[50] Priola DV, Fellows C, et. al. Mechanical activity of canine mitral valve in situ. Am J Physiol (Heart Circ Physiol) 219:1647-1651, 1970.

[51] Peskin CS. Flow patterns around heart valves: a numerical method. J Comput Phys 10:252-271, 1972.

[52] Rushmer RF, Finlayson BL, Nash AA. Movements of the mitral valve. Circ Res 4:337-342, 1956.

[53] Keren G, Meisner JS, et. al. Interrelationship of mid-diastolic mitral valve motion, pulmonary venous flow, and transmitral flow. Circ 74:36-44, 1986.

[54] Courtois M, Kovacs SJ Jr, Ludbrook PA. Transmitral flow - velocity relation. Importance of regional pressure gradients in the left ventricle during diastole. Circ 78:661-71, 1988.

[55] Barlow JB. Perspectives on the Mitral Valve. FA Davis Co, Philadelphia, 1987.

[56] McAlpine WA. Heart and Coronary Arteries. An Anatomical Atlas for Clinical Diagnosis, Radiological Investigation and Surgical Treatment. Springer, NY, 1975.

[57] Rutley MS, Adams PF, et. al. Shape and volume changes during 'isovolumetric relaxation' in normal and asynergic ventricles. Circ 50:306-316, 1974.

[58] Peskin CS, McQueen DM. Modeling prosthetic heart valves for numerical analysis of blood flow in the heart. J Comput Phys 37:113-121, 1980.

[59] McQueen DM, Peskin CS. Computer-assisted design of pivoting disc prosthetic mitral valves. J Thorac Cardiovasc Surg 86:126-135, 1983.

[60] McQueen DM, Peskin CS. Computer-assisted design of butterfly bileaflet valves for the mitral position. Scand J Thorac Cardiovasc Surg 19:139-148, 1985.

[61] Yoganathan AP, Corcoran WH, et. al. The Bjork-Shiley aortic prosthesis: flow characteristics, thrombus formation and tissue overgrowth. Circ 58:70-76, 1978.

[62] Yoganathan AP, Reamer HH, et. al. The Bjork-Shiley aortic prosthesis: flow characteristics of the present model versus the convexo-concave model. Scand J Thorac Cardiovasc Surg 14:1-5, 1980.

[63] Rajagopalan B, Friend JA, et. al. Blood flow in pulmonary veins: I. Studies in dog and man. Cardiovasc Res 13:667-676, 1979.

[64] Rajagopalan B, Friend JA, et. al. Blood flow in pulmonary veins: II. The influence of events transmitted from the right to left sides of the heart. Cardiovasc Res 13:677-683, 1979.

[65] Rajagopalan B, Bertram CD, et. al. Blood flow in pulmonary veins: III. Simultaneous measurements of their dimensions, intravascular pressure, and flow. Cardiovasc Res 13:684-692, 1979.

[66] Halperin JL, Rothlauf EB, et. al. Pulsed-Doppler echocardiographic assessment of hemodynamic function during dual-chamber cardiac pacing. (Abstract). Circ 68 (Suppl III):379, 1983.

[67] Beyar R, Sideman S. A computer study of the left-ventricular performance based on fiber structure, sarcomere dynamics, and transmural electrical propogation velocity. Circ Res 55:358-375, 1984.

[68] Beyar R, Sideman S. Atrioventricular interactions: a theoretical simulation study. Am J Physiol (Heart Circ Physiol) 252:H653-H665, 1987.

[69] Meisner JS. Left atrial role in left ventricular filling: dog and computer studies. Ph.D. thesis, Albert Einstein College of Medicine, NY, 1986.

[70] Meisner JS, Keren G, Pajaro OE, Mani A, Strom JA, Frater RWM, Landiado S, Yellin EL. Atrial contribution to ventricular filling in mitral stenosis. Circ 84:1469-1480, 1991.

[71] Thomas JD, Weyman AE. Fluid dynamics model of mitral valve flow: Description with in vitro validation. J Amer Coll Cardiol 13:221-233, 1989.

[72] Flachskampf FA, Weyman AE, Gillam L, Chun-Ming L, Abascal VM, Thomas JD. Aortic regurgitation shortens Doppler pressure half time in mitral stenosis: Clinical evidence, in vitro simulation and theoretical analysis. J Amer Coll Cardiol 16:396-404, 1990.

[73] Thomas JT, Choong CY, Flachskampf FA, Weyman AE. Analysis of the early transmitral Doppler velocity curve: Effect of primary physiologic changes and compensatory preload adjustment. J Amer Coll Cardiol 16:644-655, 1990.

[74] Hunter JF, Seaton DP, et. al. Modeling mitral valve motion: a tool for clarifying mitral valve prolapse. Tex J Sci 35:5-36, 1983.

[75] Miller GE, Marcotte H. Computer simulation of human mitral valve mechanics and motion. Comput Biol Med 17:305-319, 1987.

[76] Bryhn M, Garding L. The mitral valve mechanism with normal and prolapsed leaflets in the light of a dynamic model. Clin Cardiol 9:483-486, 1986.

[77] Kovacs SJ Jr, Barzilai B, Perez JE. Evaluation of diastolic function with Doppler echocardiography: The PDF formalism. Am J Physiol 252 (Heart Circ Physiol 21):H178-187, 1987.

[78] Taylor SEM, Whamond JS. Velocity profile and impedence of the healthy mitral valve. In: Kalmanson D, ed. The Mitral Valve. A Pluridisciplinary Approach (1976), pp. 127-136.

[79] Arts T, Reneman RS. Dynamics of the left ventricular wall and mitral valve mechanism - A model study. J Biomech 22:261-271, 1989

[80] Ormiston JA, Shah PM, et. al. Size and motion of the mitral valve annulus in man. I. A two-dimensional echocardiographic method and findings in normal subjects. Circ 64:113-120, 1981.

[81] Ormiston JA, Shah PM, et. al. Size and motion of the mitral valve annulus in man. II. Abnormalities in mitral valve prolapse. Circ 65:713-719, 1982.

[82] Smalcelj A, Gibson DG. Relation between mitral valve closure and early systolic function of the left ventricle. Brit Heart J 53:436-42, 1985.

[83] Wexler LF, Pohost GM, et. al. The relationship of the first heart sound to mitral valve closure in dogs. Circ 66:235-243, 1982.

[84] McDonald DA. Blood Flow in Arteries, 2nd Ed. Edward Arnold, London, (1974).

[85] Bellhouse BJ, Bellhouse FH. Mechanism of closure of the aortic valve. Nature 217:86-87, 1968.

[86] Bellhouse BJ, Bellhouse FH, Reid KG. Fluid mechanics of the aortic root with application to coronary flow. Nature 219:1059-1061, 1968.

[87] Bellhouse BJ, Bellhouse FH. Fluid mechanics of model normal and stenosed aortic valves. Circ Res 25:693-704, 1969.

[88] Bellhouse BJ, Talbot L. Fluid mechanics of the aortic valve. J Fluid Mech 35:721-735, 1969.

[89] vanSteenhoven AA, vanDongen MEH. Model studies of the closing behavior of the aortic valve. J Fluid Mech 90:21-32, 1979.

[90] Swanson WM, Clark RE. Aortic valve leaflet motion during systole. Circ Res 32:42-48, 1973.

[91] Gillani NV, Swanson WM. Time-dependent laminar incompressible flow through a spherical cavity. J Fluid Mech 78:99-126, 1976.

[92] Hung TK, Schuessler GB. An analysis of the hemodynamics of the opening of the aortic valves. J Biomech 10:597, 1977.

[93] Peskin CS, Wolfe AW. The aortic sinus vortex. Fed Proc 37:2784-2792, 1978,

[94] vanSteenhoven AA, Veenstra PC. The effect of some hemodynamic factors of the opening of the aortic valves. J Biomech 15:941-950, 1982.

[95] Taylor AL, Eichhorn EJ, Brickner ME, Eberhart RC, Grayburn PA. Aortic valve morphology: an important in vitro determinant of proximal regurgitant jet width by Doppler color flow mapping. J Amer Coll Cardiol 16:405-412, 1990.

[96] Grayburn PA, Eichhown EJ, Eberhart RC, Bedotto JB, Brickner ME, Taylor AL. Aortic valve morphology influences regurgitant volume in aortic regurgitation: in vitro evaluation. Cardiovasc Res 25:73-79, 1991.

[97] Reimold SC, Ganz P, Bittl JA, Thomas JD, Thoreau D, Plappert TJ, Lee RT. Effective aortic regurgitant orifice area: description of a method based on the conservation of mass. J Amer Coll Cardiol 18:761-768, 1991.

[98] Baumgartner H, Schima H, Kuhn P. Value and limitations of proximal jet dimensions for the quantitation of valvular regurgitation: an in vitro study using Doppler flow imaging. J Amer Soc Echocard 4:57-66, 1991.

[99] Yoganathan AP, Woo YR, Sung HW, Jones M. Advances in prosthetic heart valves: fluid mechanics of aortic valve designs. J Biomater Appl 2:579-614, 1988.

[100] Nygaard H, Giersiepen M, Hasenkam JM, Westphal D, Paulsen PK, Reul H. Estimation of turbulent shear stresses in pulsatile flow immediately downstream of two artificial aortic valves in vitro. J Biomech 23:1231-1238, 1990.

[101] Baumgartner H, Khan S. DeRobertis M, Czer L, Mauere G. Effect of prosthetic aortic valve design on the Doppler - catheter gradient correlation: an in vitro study of normal, St. Jude, Medtronic-Hall, Starr-Edwards and Hancock valves. J Amer Coll Cardiol 19:324-332, 1992.

[102] Segadal L, Matre K. Blood velocity distribution in the human ascending aorta. Circ 76:90-100, 1987.

[103] Thrubriker M, Harry R, Nolan SP. Normal aortic valve function in dogs. Am J Cardiol 40:563-8, 1977.

[104] vanSteenhoven AA, Verlaan CWJ, et. al. The closing behavior of the natural aortic valve. In: Baan J, Arntzenius AC, Yellin EL, ed. Cardidac Dynamics. Nijhoff, The Hague (1980), pp. 477-488.

[105] Lucas CL, Keagy BA, et. al. Velocity profile in the canine ascending aorta and its effects on the accuracy of pulsed-Doppler determination of mean blood velocity. Cardiovasc Res 18:282-293, 1984.

[106] vanRenterghem RJ, Arts T, et. al. On-line measurement of arotic valve ring deformation during the cardiac cycle. Am J Physiol (Heart Circ Physiol) 254:H795-H800, 1988.

[107] Fauci LJ, Peskin CS. A computational model of aquatic animal locomotion. J Comput Phys 77:85-108, 1988.

[108] Fauci LJ. Interaction of oscillating filaments: a computational study. J Comput Phys 86:294-313, 1990.

[109] Fogelson AL. A mathematical model and numerical method for studying platelet adhesion and aggregation during blood clotting. J Comput Phys 56:111-134, 1984.

[110] Beyer RP. A computational model of the cochlea using the immersed boundary method. J Comput Phys 98:145-62, 1992.

[111] Fogelson AL, Peskin CS. A fast numerical method for solving the three-dimensional Stokes' equations in the presence of suspended particles. J Comput Phys 96:339-68, 1988.

[112] Peskin CS, McQueen DM. A three-dimensional computational method for blood flow in the heart: I. Immersed elastic fibers in a viscous incompressible fluid. J Comput Phys 81:372-405, 1989.

[113] McQueen DM, Peskin CS. A three-dimensional computational method for blood flow in the heart: II. Contractile fibers. J Comput Phs 82:289-297, 1989.

[114] Chorin AJ. Numerical method for solving incompressible viscous flow problems. J Comput Physics 2:12-26, 1967.

[115] Chorin AJ. On the convergence of discrete approximations to the Navier- Stokes equation. Bull Am Math Soc 73:341-353, 1967.

[116] Chorin AJ. Numerical solution of the Navier-Stokes equations for an incompressible fluid. Math Comput 23:928-931, 1969.

[117] Hunter WC, Baan J. The role of wall thickness in the relation between sarcomere dynamics and ventricular dymanics, as noted in McQueen et. al., Amer J Physiol 242:H1095-1110, 1982 (4).

[118] Braunwald E, Ross J, Sonnenblick EH. Mechanism of Contraction of the Normal and Failing Heart. Little Brown Co, Boston, 1976.

[119] Parmley WW, Chuck L, Sonnenblick EH. Relation of Vmax to different models of muscle contraction. Circ Res 30:34-43, 1972.

[120] Tsakiris AG, Padiyar R, et. al. Left atrial size and geomtery in the intact dog. Am J Physiol (Heart Circ Physiol) 242:H167-172, 1977.

[121] Alexander J, Nikolic S, et. al. The role of the pulmonary venous impedence and the atrium in determining characteristics of left ventricular filling. Presented at the Cardiac Systems Dynamics Society Meeting, Halifax, Nova Scotia, 1988.

[122] Bolger AF, Eigler NL, Maurer G. Quantifying valvular regurgitation. Limitations and inherent assumptions of Doppler techniques. Circ 78:1316-1318, 1988.

[123] Sahn DJ. Instrumentation and physical factors related to visualization of stenotic and regurgitant jets by Doppler color flow mapping. J Am Coll Cardiol 12:1354-1365, 1988.

[124] Maciel B, Loises VA, Shandas R, et. al. Effects of pressure and volume of the receiving chamber on the spatial distribution of regurgitant jets as imaged by color Doppler flow mapping. An in vitro study. Circ 83:605-613, 1991.

[125] Gardin JM, Lobodzinski SM. Do Doppler color flow algorithms for mapping disturbed flow make sense? J Am Soc Echo 3:310-315, 1990.

[126] Bell JB, Collela P, Glaz HM. A second-order projection method for the incompressible Navier Stokes equations. J Comput Phys 85:257-83, 1989.